

## **Partner Project 1779p**

# **“Optimization of MW Plasma Influence on Aerodynamic Characteristics of Body in Airflow “**

## **Final Report**

**To European Office of Aerospace Research  
and Development**

**Period 01.04 2000 – 31.03.2001**

**Project Manager  
Dr. Yuri Kolesnichenko**

**Moscow**

**2001**

## Form SF298 Citation Data

<b>Report Date</b> <i>("DD MON YYYY")</i> 30032001	<b>Report Type</b> N/A	<b>Dates Covered (from... to)</b> <i>("DD MON YYYY")</i>
<b>Title and Subtitle</b> Optimization of MW Plasma Influence on Aerodynamic Characteristics of Body in Airflow		<b>Contract or Grant Number</b>
		<b>Program Element Number</b>
<b>Authors</b> Kolesnichenko, Yury F.		<b>Project Number</b>
		<b>Task Number</b>
		<b>Work Unit Number</b>
<b>Performing Organization Name(s) and Address(es)</b> Moscow Technical Club (MTC-IVTAN) Izhorskaya str., 13/19 Mosow 127412 Russia		<b>Performing Organization Number(s)</b>
<b>Sponsoring/Monitoring Agency Name(s) and Address(es)</b> EOARD PSC 802 BOX 14 FPO 09499-0200		<b>Monitoring Agency Acronym</b>
		<b>Monitoring Agency Report Number(s)</b>
<b>Distribution/Availability Statement</b> Approved for public release, distribution unlimited		
<b>Supplementary Notes</b>		
<b>Abstract</b>		
<b>Subject Terms</b>		
<b>Document Classification</b> unclassified		<b>Classification of SF298</b> unclassified
<b>Classification of Abstract</b> unclassified		<b>Limitation of Abstract</b> unlimited
<b>Number of Pages</b> 107		

REPORT DOCUMENTATION PAGE			Form Approved OMB No. 0704-0188	
Public reporting burden for this collection of information is estimated to average 1 hour per response, including the time for reviewing instructions, searching existing data sources, gathering and maintaining the data needed, and completing and reviewing the collection of information. Send comments regarding this burden estimate or any other aspect of this collection of information, including suggestions for reducing this burden to Washington Headquarters Services, Directorate for Information Operations and Reports, 1215 Jefferson Davis Highway, Suite 1204, Arlington, VA 22202-4302, and to the Office of Management and Budget, Paperwork Reduction Project (0704-0188), Washington, DC 20503.				
1. AGENCY USE ONLY (Leave blank)		2. REPORT DATE  30-March-2001		3. REPORT TYPE AND DATES COVERED  Final Report
4. TITLE AND SUBTITLE  Optimization of MW Plasma Influence on Aerodynamic Characteristics of Body in Airflow			5. FUNDING NUMBERS  ISTC Registration No: 1779	
6. AUTHOR(S)  Dr. Yury F. Kolesnichenko				
7. PERFORMING ORGANIZATION NAME(S) AND ADDRESS(ES)  Moscow Technical Club (MTC-IVTAN) Izhorskaya str., 13/19 Mosow 127412 Russia			8. PERFORMING ORGANIZATION REPORT NUMBER  N/A	
9. SPONSORING/MONITORING AGENCY NAME(S) AND ADDRESS(ES)  EOARD PSC 802 BOX 14 FPO 09499-0200			10. SPONSORING/MONITORING AGENCY REPORT NUMBER  ISTC 00-7003	
11. SUPPLEMENTARY NOTES				
12a. DISTRIBUTION/AVAILABILITY STATEMENT  Approved for public release; distribution is unlimited.			12b. DISTRIBUTION CODE  A	
13. ABSTRACT (Maximum 200 words)  This report results from a contract tasking Moscow Technical Club (MTC-IVTAN) as follows: The contractor will demonstrate the ability to change the aerodynamic drag of a body using microwave-generated plasma in front of the body. He will perform the following: a) study the dynamic characteristics of MW discharge in supersonic airflow; b) study the dynamic characteristics of plasma-body-airflow interaction; c) measure the temperature in different components of plasma; d) study the relaxation characteristics of MW plasma in a supersonic airflow, such as lifetime, electron density and others; e) study the plasma effect in dependence on structure of MW field, plasma volume, polarization, operation mode, optimization, etc. In summary, he will obtain and provide a data set for mathematical simulations.				
14. SUBJECT TERMS  EOARD, Aviation Technology, Aerodynamics			15. NUMBER OF PAGES  Unknown	
			16. PRICE CODE  N/A	
17. SECURITY CLASSIFICATION OF REPORT  UNCLASSIFIED	18. SECURITY CLASSIFICATION OF THIS PAGE  UNCLASSIFIED	19. SECURITY CLASSIFICATION OF ABSTRACT  UNCLASSIFIED	20. LIMITATION OF ABSTRACT  UL	

## Project Team

**V.G. Brovkin**

Dr. in Technical Sciences,  
IHT, MW experiment

**A.A. Gorynya**

Engineer, ARSRIRE,  
MW generator

**Yu.F. Kolesnichenko**

Dr. in Physics and Mathematics,  
IHT, Project Manager

**A.A. Krylov**

Dr. in Physics and Mathematics,  
SRIMM, Sub-manager

**V.A. Lashkov**

Dr. in Physics and Mathematics,  
SRIMM, gas dynamic experiment

**I.Ch. Mashek**

Dr. in Physics and Mathematics,  
SRIMM, optic measurements

**E.N. Osetrov**

Engineer, ARSRIRE, MW  
installation, technical support

**M.I. Rivkin**

Dr. in Technical Sciences,  
ARSRIRE, MW radiation system

At different stages of investigation a credit was made by:

Dr. D.V. Khmara (MRTI)

Dr. V. Krivtsov (MPhTI)

Dr. V.N. Sukhov (IHT)

K.V. Savelkin (IHT)

A.I. Gruzdev (ARSRIRE)



## Contents

<b>Introduction</b>	<b>5</b>
<b>I. Description of facility</b>	<b>6</b>
1.1. Gas-dynamic installation	6
1.2. MW installation	7
<b>II. Diagnostics</b>	<b>7</b>
2.1. Pressure sensors	7
2.2. Schlieren images	8
2.3. Integral optic and spectral measurements	9
2.4. Method of gas temperature measurements	10
2.5. Method of vibrational temperature measurement	11
<b>III. Experimental results</b>	<b>13</b>
3.1. Free flow parameters	13
3.2. Microwave discharge structure	14
3.3. Local kinetics in discharge and afterglow	16
3.4. Gas dynamics with MW discharge	18
<b>IV. Numeric modeling</b>	<b>21</b>
4.1. Evolution of chemical composition of the discharge	21
4.2. Electron excitation rate constants modification	23
4.3. Discharge parameters evolution during active phase	25
4.4. Gas dynamics effect evaluation	26
<b>V. Discussion</b>	<b>26</b>
5.1. Synchronizing of Schlieren, Kulite and optics	27
5.2. Spatial-temporal picture of interaction	27

5.3. Energy input and local parameters of discharge	28
5.4. Shock-shock and shock-density well interaction	30
5.5. Experimental modeling of action at high repetition rate	31
5.6. Optimization of the effect	33
5.7. Nature of the effect	34
<b>Summary</b>	36
<b>Conclusion</b>	39
<b>Acknowledgments</b>	39
<b>References</b>	40
<b>Figures</b>	41
<b>Supplement</b>	78

## Introduction

The project 1779p “Optimization of MW Plasma Influence on Aerodynamic Characteristics of Body in Airflow “ took start at April, 2000. The main goal of the activity was to understand the physical basis of the phenomena of drag reduction of AD-body in supersonic airflow caused by creation of MW discharge in front of such a body. The problem been taken in general, had its history, as an anomalous features of plasma interactions with high speed bodies and air flows have been revealed far ago [1,2]. Two main reasons for effect explanation were proposed – gas heating (thermal mechanism) and/or plasma action (non-thermal mechanism). For a long time the activity of investigation teams was aimed at finding out the conditions for non-thermal mechanism realization and sometimes the results were encouraging, i.e. gas heating seemed to be not enough for the effect explanation. Nevertheless, up to now the physical basis of the effect (and even its existence) is far from consensus among investigators. The idea of key experiments in this area, the conditions of which would have been purified to the extent of undoubted treatment, has led to the first experiments on drag reduction by means of MW discharge action [3]. Preliminary results gave some reasons for the non-thermal mechanism realization expecting [3,4], and careful investigation of the phenomenon became far-going challenge for background of plasma aerodynamics. That is why, *the objective of the project is to clarify the process of MW plasma interaction with gas-dynamic structure of a flow near the AD bodies and to find conditions for maximum drag reduction.*

The Project was implemented by the three Institutions: Institute of High Temperatures RAS (Moscow) – leading Institute, St.-Petersburg State University and All-Russian Scientific-Research Institute of Radio-Equipment (St.-Petersburg). IHT, according to its background in MW and plasma aerodynamics, provides methodic for MW discharge parameters investigation (including investigations at its own MW facility), experimental data processing and coordinated the works. SRIMM of St.-PSU provided wind tunnel, diagnostic equipment and their service. ARSRIRE provided MW generator, radiating system and its technical service. The project activity was estimated at 12 months.

The great importance of diagnostics for solving the problem itself and for providing modern experiment in such a complicated area as plasma aerodynamics was evident. Most of experiments in this area can not be analyzed properly for the lack of essential information about the main discharge-flow parameters. Therefore, we’ve strengthened our efforts firstly

on working out an appropriate diagnostic tools. Then we focused our attention in investigations on eliminating of the spatial-temporal details of MW discharge regions interaction with SS flow. These measures allowed us to obtain new important and valid information about the object under investigation.

This report presents the results of investigation of MW discharge in supersonic flows and its application for plasma creation and energy release in front of AD bodies.

## I. Description of the facility

For providing of the experiments with MW discharge in supersonic flows the unique experimental installation was made at the base of wind tunnel of the SRIMM St.-Petersburg State University. It includes wind tunnel, powerful microwave generator and diagnostic equipment.

**1.1. Gas-dynamic installation.** The layout of the facility is shown in Fig.1.1. The air flow is generated by means of the central supersonic conic nozzle with exit Mach number of 1.5. The outer supersonic nozzle, gas ejector, was set up to obtain the rarefaction in the working chamber. Geometry and parameters of the working jet are determined in such a way that the jet boundary be enclosed by the inlet part of the diffuser. The geometry of the nozzle has been chosen to obtain the maximal rarefaction in the working chamber, namely the pressure level of 0.16-0.20ata. It is known that in the under-expanded jet there is a monotonous increase of gas velocity and decrease of pressure and temperature while gas passes from the nozzle to the Mach disk. In this the gas pressure may become lower than the environmental one. By moving the central nozzle relative to the outer one, one can change the static pressure of the outer media where the working flow is exhausted. The gas flow rate through the central nozzle and thus, stagnation pressure can be regulated by the iris diaphragm. With these measures, the following parameters of the working flow have been obtained: static pressure about 60Torr, flow Mach number 1.5-1.8 and static temperature 170 - 210K. The flow field is controlled by virtue of shadow device. Two geometrically identical conic nozzles were used – one made of metal, the other – from dielectric (Teflon). Different gases can be tested, while the central pipe is fed by these gases and mixtures from the tanks.

**2.2. Microwave installation.** The microwave unit is the klystron type generator of high power pulses with the X-range carrying frequency. The microwave pulses come through the wave-guide to the radiator of parabolic mirror mounted in the working chamber. The wave-

guide is hermetically sealed, the radiator is closed up by the radio-transparent unit, the air pressure in the wave-guide is maintained at the level 1.8atm. The radiator is fixed just over the diffuser of the wind tunnel. The mirror is maintained on the main nozzle and focuses the microwave radiation on to the flow axis, in the region remote at 210-240mm from the nozzle exit. Both position of the central nozzle and the studied models influence the distribution of microwave field in the focal region. The highest pulse power value attained 210kW. The pulse duration is in between 1.2-2.2 microseconds. The pulse frequency can be as high as 1.0kHz, thus, the maximum mean power of the microwave facility is about 400W. The radiated MW flux can be linear and circular polarized. In the case of linear polarized MW radiation three orientations of electric field vector of the wave are available – two of them perpendicular to the flow velocity vector (vertical and horizontal directions, or perpendicular and parallel to the Schlieren main optic axis, correspondingly), and the last one – parallel to the flow velocity vector. For this variant realization additional focusing mirror has been manufactured and installed, as well as feeding and radiation systems.

Photos of gas dynamic chamber inside view and MW generator are presented at Fig1.2.

## II. Diagnostics

**2.1. Pressure sensors.** To investigate the influence of plasmoids on the drag the pressure probes based on the piezoelectric effect are used. Two types of such a probe are produced. One, as a total pressure probe and another - as a static pressure probe. Piezoelectric sensors are mounted on the total pressure probe and on the cylindrical surface of static pressure probe. The sensors are dislocated within the metallic bandage of the probes and are galvanically isolated from them. The signal from sensor comes to the fore-amplifier, further - to standard U2-9 amplifier and, finally, to the F4226 ADC-device of CAMAC system. To avoid the appearance of discharge on the probe surface the special fluoroplast shirts are mounted on the probe, which are the combinations of hemisphere –cylinder, or are blunt-nosed cylinders. This measure also allows to control the position of plasmoid relative to the probe. Special microwave/no-flow tests have been made to evaluate the influence of electrical hindrances on the probe operation.

For calibration of the probes the shock tube has been worked out and built. Calibration was made at the pressures, which are close to that in the working flow of the wind tunnel (of the order 50-80 Torr). The method of probes calibration was also worked out.

The results of the pressure probe investigation in a shock tube are presented at Fig.2.1. The electric signal from the probe changes in time while a shock is acting on it. It is seen that at approximately 1000 $\mu$ s the SW comes to the probe, the last reacts by the spike of voltage, then it attains some level of voltage which monotonously decreases. About 2000 $\mu$ s the contact surface which separates the high- and low-pressure gas comes to the probe. This calibration has shown that the time resolution of the probe is about 0.5-1 $\mu$ s, sensitivity – 3.27Torr/mV.

Testing and calibration of the full-pressure probes based on the using of another types of piezoelectric elements are also done.

The results of investigation of the probe based on Kulite sensor are shown in Fig.2.2. Kulite sensor has resolution time of order 10 $\mu$ s and sensitivity 7.8Torr/mV. It has better transient characteristics than the previously tested sensors. But at approaching the wind tunnel operation condition the pressure up to 5 atm can act on full-pressure receiver. This circumstance troubles Kulite sensor using, as it is designed for pressure measurements not exceeded 0.6atm. Therefore, for protection of the sensor from damage while the wind tunnel begins to run it is positioned near the central nozzle before the run starts and only after attaining the working regime of a flow is displaced in the desired point by means of coordinate gear.

**2.2. Schlieren images.** General scheme of optic measurements is shown at Fig.2.3. To carry out optical studies of influence of pulsed microwave discharge on the supersonic flow around the models experimental facility based on modification of IAB-450 measuring device was used. The facility includes TV camera based on CCD-matrix, fore-amplification complex and TV signal processing, video recorder, pulse light feeder, control video monitors and the system for synchronizing, control and processing of experimental data by means of CAMAC system, which is controlled by IBM PC. Standard CD-matrix can only register the integral in time pattern of flow passed through the measuring system during 20ms and cannot provide the required temporal resolution of order 1-2 $\mu$ s. For an attaining of the mentioned resolution time the scheme of impulse lighting of the flow process is adopted, being synchronized with discharge ignition moment and delayed for a defined time interval. At a rather high frequency of event repetitions (0.5 - 1kHz in our case), and under the mentioned above integration time,

every TV-frame contains from 10 to 20 realizations of the process. Such a scheme allows the flow pattern corresponding to a selected phase of a process to be recorded on the integrating image receiver (CCD-matrix). The change in delay time during experiment allows to make a TV record of unsteady-state flow, the time resolution being determined only by the duration of pulse lighting and the rate of change in delay time. Further data processing is to select the representative pictures from the recorded set, digitize them and numerically process them with computer.

The most important modifications have been made to IAB-450 device included replacement of the standard lighter by a powerful impulse infrared led AL119A and installing of a matching optics, which allows to form a TV camera image field and to remote it in the region with an acceptable level of spurious MW irradiation.

After MW discharge ignition, an impulse current of order 25-30A and duration 1-2 $\mu$ s is passed through the IR-led. The lighting delay time relative the MW pulse can be changed by a program in time range 1-500 $\mu$ s and is fixed at TV frame.

**2.3. Integral optic and spectral measurements.** Investigation of the spatial-temporal and spectral characteristics of light emission of MW discharge in supersonic flow is carried out by two measuring channels. The first is aimed at registering of spectral characteristics of discharge itself and the subsequent process of chemiluminescence in the defined spatial region and at a fixed time moment after MW pulse. The second is integral over spectrum and is aimed at investigation spatial-temporal characteristics of MW discharge and afterglow process in SS flow. This channel is also used for detecting evolution of light emission in a narrow (of order 20 Angstrom) spectral interval. Both of the measuring channels have the identical optical schemes of the investigated radiation collection and transportation, consisting of aperture ratio lens and high-aperture optical fibre. Both of the receiving systems observe practically the same spatial region and are placed on the common coordinate shaft, which allow to move the domain under investigation over the flow axis. For the spectral channel the observed domain is bounded by ellipsoid of revolution of 3mm in diameter and 25-30mm in length, which is positioned perpendicular the flow axis and intersects it. The domain of observation of the integral channel is more extended and is about 4.5-5mm diameter at practically the same length. The optical axis of the integral channel intersects the flow axis at the angle 9.5 degree. The distance between the receiving lens and the flow axis is 230mm. The range of the flow region which can be observed is up to 195mm, spatial step of displacement – 0.2mm, time of passing over the total region length 3s.

As the main spectral device for analyzing emission spectra of microwave discharge in a supersonic air jet the spectrometer based on the monochromator MDR-2 has been adopted. A scanned grating monochromator (1200 line/mm) with a working range 200-625nm. The spread function of the spectrometer has been measured by single-frequency laser and turned out to be 0.2nm at monochromator dispersion 2nm/mm and slot width 100 $\mu$ m.

The scanning over the wavelength of the monochromator is made by means of the step-by-step drive. The minimum spectral step is 0.029nm/step. Spectral device has been gauged in the range of wave lengths 300-600nm with a Hg-He spectral lamp of type of DRGS-12, worked in standard operation mode. Spectral sensitivity of the device has been gauged in the working wave length range by means of light-measuring lamp SIRSH8,5-200-1 with the color temperature about 3000K.

The output radiation of the monochromator is transformed to an electrical signal by the photoelectric multiplier of the type of the FEU-79. The output signal of the preamplifier of the FEU is analyzed by the sample-storage circuit made on a particular chip. Time of sample is 0.1  $\mu$ s, sample delay time is 1-3  $\mu$ s. The signal of the sample-storage circuit is recorded by the computer and the spectrometer is tuned in step on the wavelength.

#### **2.4. Method of gas temperature measurements.**

Spectroscopy of the second positive system of molecular nitrogen was chosen as a method of gas temperature measurements. The optical spectrums were registered by means of a spectrograph MDR-23. The device spread function is 0.15nm. So, a partially resolved molecular spectrum is obtained in experiment.

For the determination of gas temperature in a discharge the method of optical emission spectrum shape fitting has been adopted. The exact full spectrum of 0-0 transition of the second positive nitrogen system, including R-, P- and Q-branches (the last is very weak) is generating under the defined temperature and it is then convoluted with the spread function of the spectral device. The synthetic spectrum obtained in such a manner is then compared with the real one. It is made in a procedure of best fitting of the spectrum contour by variation of the defined temperature. In this case the special attention is paid for the best coincidence of the spectral shape at the lower rotational numbers, where the distribution over the rotational levels is known to establish at a temperature practically equal to that of the gas. The example for such fitting is shown at Fig.2.4. The accuracy of the temperature determination by this procedure can be estimated in 50K at high temperatures and 10-20K at low temperatures. It



should be noted that due to the measurement technique the maximum temperature during the discharge evolution is determined.

## 2.5. Method of vibrational temperature measurement

Determination of vibrational temperature of the ground state of nitrogen molecule in discharge plasma can be done by analyzing the relative intensities of edgings of a given sequence ( $\Delta v = \text{const}$ ) in the spectrum of the second positive nitrogen system. It should be noted that this procedure is referred to the class of inverse problems (generally speaking, incorrect).

Firstly, the vibrational temperature  $T_{\text{vib}}$  of the radiating electronic state is determined as an inclination of a straight line which serves as a graph of dependence

$$\ln ( I_{v_1 v_2} / q_{v_1 v_2} \nu^4 ) = E_{\text{vib}} / k T_{\text{vib}} ,$$

where  $I_{v_1 v_2}$  is the intensity of vibrational transition  $v_1-v_2$ ,  $v_1$  and  $v_2$  - the quantum numbers of the upper and lower levels accordingly,  $q_{v_1 v_2}$  - Frank - Condon factors,  $\nu$  - the frequency of light emission,  $E_{\text{vib}} = \omega_e \cdot (v_1 + 1/2)$  - the energy of the upper vibrational level,  $\omega_e$  - vibrational constant (quantum) for a given molecular electronic state.

Then equations for an upper electronic state vibrational levels excitation by direct electron impact from ones of the ground state (in the case of the second positive nitrogen system the transitions from  $X^1\Sigma_g^+(v = 0, 1, \dots)$  to  $?^3\Pi_u(v = 0 - 4)$  are taken into account) are to be written with understanding that appropriate excitation constants are proportional to Franc-Condon factors. Under some assumptions about upper state deactivation, a system of linear equations for several vibrational levels of the ground state population is obtained. The problem is that due to the uncertainties in experimental data and the assumptions made the probability of obtaining some roots with negative sign is rather high. Nevertheless, this method can be applied for several discharge regimes – impulse and steady-state.

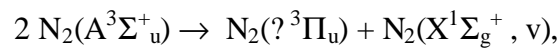
For steady-state situation the graph can be obtained which couples the value of vibrational temperature of the excited state with such of the ground state. The idea is to calculate under the fixed vibrational temperature of the ground state the distribution over vibrational levels of the excited state, which turns out to be non-Boltzmann. But it can be fitted to Boltzmann one with appropriate temperature. Under some conditions this relation is unique.

For the situation of a short-impulse discharge it should be taken into account that characteristic time of distribution function relaxation over vibrational levels is sufficiently larger than that for translational and rotational ones. This situation is illustrated by Fig.2.5,

where distribution function over vibrational levels of nitrogen molecules is shown for different points of time. The characteristic relaxation time is of order of several times of VV exchange at the lower levels, it is about 30μs at 100Torr air pressure. It is seen that for the first 20 - 30μs after the short (about 2μs) electric discharge the distribution function (evaluated via vibrational temperatures of the first and second levels) is highly non-equilibrium, and only after 30μs it converges to an equilibrium value. As the spectrum can be obtained only by the end of electric pulse, when distribution function is the most non-equilibrium due to electron excitation of vibrational levels, the above mentioned method for vibrational temperature determination is not valid in general and corrections are to be made to have more adequate result. This situation is characteristic to relatively low levels of vibrational excitation, so only the first vibrational level population can be determined with eligible reliability.

For determination of vibrational temperature in both situations of stationary and impulse discharges the program is developed. It allows by processing of the sequence  $\Delta v = -3$  (transitions 0-3, 1-4 and 2-5) and  $\Delta v = -2$  (transitions 0-2, 1-3 and 2-4) of the second positive nitrogen system spectrum to define vibrational temperature of the ground state in steady-state situation and the relative population of the level  $v=1$  of the nitrogen ground state  $X^1\Sigma_g^+$  in situation of short-impulse discharge.

The correct determination of vibrational temperature  $T_v$  of the ground state demands as a necessary condition an occupying the upper electronic state ( $?^3\Pi_u$ ) by the direct electron impact from the main state ( $X^1\Sigma_g^+$ ). Alternative to the direct electron impact channel of an occupying a  $?^3\Pi_u$  state is the process



with the velocity constant  $k^* \approx 7.7 \cdot 10^{-11} \text{ cm}^3/\text{s}$ . Comparison of the population fluxes of a  $?^3\Pi_u$  level via the both channels under average concentration of electrons in the discharge and reduced electric field in the plasma should be done. This give a basis to consider the population of  $?^3\Pi_u$  level by the direct electron impact to be the main mechanism.

Nevertheless, determination of gas and vibrational temperatures remains one of the most delicate and debatable procedures in gas discharge physics and demands additional investigation in every case under consideration.

### III. Experimental Results

Almost all experiments were done under the linearly polarized peak MW power of about 200-210kW, MW pulse duration 1.5-1.8 $\mu$ s and pulse repetition rate 500kHz.

#### 3.1. Free flow parameters

##### *a. Measurements with AD-probes*

The working flow is formed by a cone nozzle, thus inside it the flow is also cone-like (“diffluent”). At the exit section the working flow interacts with an external flow, which acts towards the nozzle axis. Therefore, the inclined shock-waves appear, which form a convergent cone structure with an apex at a distance of about 22-23mm from the exit section. This distance is regulated by the iris diaphragm and is chosen as a compromise between obtaining the flow without blunt shock and the level of the flow parameters inhomogeneity.

Gas dynamic parameters of a free flow without MW discharge were measured along the flow axis and over flow radius by means of AD probes of total and static pressure. The distributions of the M-number, total and static pressures, static temperature and gas density over x- and r- axes were obtained. They show that there is a region between 40 and 70mm where the flow parameters are nearly constant with M-number about 1.7. This region was chosen as working one and almost all measurements were fulfilled here. Distribution of M-number, total pressure, gas density and static temperature of the flow (obtained by the optic method which will be presented below) is shown at Fig.3.1,2.

##### *b. Schlieren images of a flow structure and AD-body streamlining*

The flow structure is also well seen at the Schlieren image. It shows the near-nozzle region with characteristic gas-dynamic structure in the form of cone, which, as was noted above is a consequence of the way of the working flow obtaining. The outer flow being turbulent also prevents obtaining high-quality Schlieren images and using sensitive optic methods.

Another method of the M-number determination was used via measurement of the BSW stand-off while the AD body was displaced over the flow axis. The body was of 8mm diameter blunt-nosed cylinder. The calculated M-number over x-coordinate is shown at Fig.3.1 and is in a reasonable agreement with the other measurements.

##### *c. Fluctuations of free flow (Kulite measurements)*

Signals from Kulite were recorded in a free airflow to obtain information of the flow noise and to determine the number of realizations for averaging which are needed for correct measurements of pressure at stagnation point. Three series of measurements were fulfilled –

with single realization, averaging over 10 and 100 realizations. Then the standard deviation of a signal was determined. The dependence of such a deviation over number of realizations turned out to have a slope  $-0.514$ , which is very close to  $-0.5$ . Thus, the flow fluctuations are stochastic and can be eliminated by averaging over 100 realizations – this number was used in all Kulite measurements. Samples of Kulite signals are shown at Fig.3.3.

### 3.2. MW discharge structure

#### a. *MW-field structure, absolute values*

Spatial distribution of linear polarized (y-directed) MW field in the working region was measured by special small-size symmetric dipole. As a MW signal source, the nominal MW generator was used in a modified scheme, the radiated power been attenuated to the acceptable safe level. The absorbed signal then was detected and measured by the oscilloscope. The probe was displaced inside of the tested region by the coordinate gear. To calibrate the measuring scheme and obtain the absolute values of the fields, additional operations were fulfilled. The near-field of radiator was measured at a distance  $40\text{mm}$  ( $1.2\lambda$ ) and the boundaries where the field intensity can be neglected were determined. Thus, the integral of the measured distribution over this surface is equal to all radiated MW power and normalization coefficient can be obtained. With using of these data and for radiated power  $210\text{kW}$  the distribution of the amplitude value MW field over 3- coordinates is shown at Fig.3.4-3.5. It is readily seen that there are 3 maximums in electric field in the working region – placed respectively, at  $16\text{mm}$ ,  $36\text{mm}$  and  $55\text{mm}$  from the exit section of the central (working) nozzle, the main being at  $36\text{mm}$ . Measurements were made for both metal and dielectric nozzles and y-, z-directed polarization.

#### b. *Absorption of MW power in discharge*

MW signals with and without discharge were detected by a special probe and recorded in experiments with air and carbon dioxide. The samples of such records are presented at Fig.3.6. It can be seen that as usual the absorption coefficient is of order  $0.50 \pm 0.15$ , but under the special conditions (i.e. model position) it can attain values which are close to unity.

#### c. *E/N distribution, Light emission structure*

The distribution of the reduced electric field  $E/N$  can be obtained with using information from AD- and MW-probes. Such a distribution for the case of air and dielectric nozzle is shown at Fig.3.5. But placing of AD-body influences the field distribution, at least, when a body is positioned nearer than  $75\text{mm}$ .

Light emission structure of MW discharge in a free airflow confirms the validity of the measurements presented above. Three domains of the increased luminosity are well seen just at the above positions. Two types of light emission distribution measurements were carried out – averaged (over 10 realizations) and instant (single realization). They are shown at Fig.3.7 and give information of the real discharge structure. Also averaged emission distributions are shown at Fig.3.8 for different positions of the AD-body. These distributions confirm the change in MW-field structure. The nearest to the AD-model plasmoid appears at a fixed distance (approximately 7-8mm, or  $\lambda/4$ ) in the range of positions 40 – 70mm. Thus, displacing a model over x-axis, the action of 1, 2 and 3 plasmoids can be realized, the last 2 situations are presented at Fig.3.9.

*d. Photos – single pulse and integral*

Another portion of important information of the discharge and gas dynamic structure can be obtained from the direct photos of discharge in a single pulse and as superposition of number of pulses (Fig.3.10). The main difference between such a photos is that the last show the boundaries of realizations, as the first – the real structure realization, which can differ slightly from pulse to pulse in the boundaries determined above. Also, the contribution of UV-hallo from discharge channels in the total emission is more pronounced in the last case.

Two types of MW discharge plasma objects are realized in the case of linear polarized radiation: highly non-uniform plasma structure in the form of a channel (half-wave dipole), elongated in y- or z- direction and cylindrically symmetric relatively uniform creation in the form of a cone (what are additional foundations to treat this plasmoid as cylindrically symmetric will be presented below). If there is more than one plasmoid in a flow, the nearest one to the model is a channel.

*e. Peculiarities in different gases*

Three gases except air were tested – carbon dioxide, nitrogen and argon. In general, the picture of discharge in molecular gases is close to that in air, especially for nitrogen. The last demonstrates more distinct channel structure and number of channels is more. The light emission spectrum of discharge is also close to that in air. The discharge in carbon dioxide is not so bright as a whole and has violet color, but sometimes very bright green channels appear inside the glow (as well as the discharge at front surface of the AD-model emitted such radiation in a certain positions). The breakdown characteristics seem to be close to that obtained for a static gas [7]. The structure of the first plasmoid is practically the same in all the tested molecular gases. The channels (dipoles) also have their fine structure which can be

### 3.3. Local kinetics in discharge and afterglow

Spectroscopy of the second positive system of molecular nitrogen was chosen as a method of gas temperature measurements in air. The optical spectrums were registered by means of a spectrograph MDR-23. The device spread function is 0.15nm. So, a partially resolved molecular spectrum can be obtained in experiment.

Also review spectra in the wavelength range 3500-4100Å were obtained, providing information of vibrational excitation of nitrogen molecules.

For the determination of gas temperature in a discharge the method of optical emission spectrum shape fitting has been adopted. The exact full spectrum of 0-0, 0-2, 0-3 and 1-4 transitions of the second positive nitrogen system, including R-, P- and Q-branches (the last is very weak) is generating under the defined temperature and it is then convoluted with the spread function of the spectral device. The synthetic spectrum obtained in such a manner is then compared with the real one. It is made in a procedure of best fitting of the spectrum contour by variation of the defined temperature. In this case the special attention is paid for the best coincidence of the spectral shape at the lower rotational numbers, where the distribution over the rotational levels is known to establish at a temperature practically equal to that of the gas.

*1st plasmoid (cone):*    0-0 transition,  $T = 200\text{K}$  ( $t = 1.7\text{ns}$ ),  
                                  0-3 transition,  $T = 240\text{-}250\text{K}$  ( $t = 1.7\text{ns}$ ),  
                                  0-3 transition,  $T = 250\text{-}270\text{K}$  ( $t = 2.5\text{ns}$ )  
*2nd plasmoid (channel):*    0-0 transition,  $T = 270\text{K}$  ( $t = 2.5\text{ns}$ ),

*0-3 transition,  $T = 320K$  ( $t = 2.5\text{ms}$ ),*

*0-3 transition,  $T = 320K$  ( $t = 2.5\text{ms}$ ),*

*1-4 transition,  $T = 300K$  ( $t = 2.5\text{ms}$ ).*

The accuracy of the temperature determination by this procedure can be estimated in 20K. It should be noted that 0-0 transition has given lower temperature in comparison with 0-3 transition, but the difference between temperatures in the first and the second plasmoids is approximately the same – about 70K.

Temperature measurements were also made for all plasmoids in the case of z-polarization of MW flux. Transitions 0-2 and 1-4 were used. The following values were obtained (model was at 75mm position):

*Cone plasmoid:  $T = 200K$  (0 – 2), 220K (1 – 4)*

*First channel:  $T = 230K$  (0 - 2), 270K (1 – 4)*

*Second channel:  $T = 240K$  (0 – 2), 270K (1 – 4).*

Thus, in general the temperatures are lower in comparison with y-polarization, but the temperature in the cone plasmoid once again turned out to be less than in a channels.

Typical review and band spectra are presented at Fig.3.11.

#### *c. Evolution of optical emission in plasmoids during active phase*

For determination of local discharge parameters, evolution of integral optical emission and emission in molecular bands from different plasmoids were registered in air during discharge active phase. The typical “oscillograms” of 0-2 band emission from all three plasmoids are presented at Fig.3.12. Time-dependent curves of radiation for 0-2 and 1-4 transitions of the second positive nitrogen system obtained from two filamentary plasmoids (z-polarization) are shown at Fig.3.13.

#### *d. Weak luminescence*

Just in the first experiments with MW discharge in SS airflow the weak yellow-green luminescence has been observed as afterglow. Due to it, in the appropriate conditions the BSW can be seen even with the naked eye. We consider this emission as chemiluminescence which takes place at recombination of  $O(^3P)$  atoms with  $NO(X^2P)$  molecule [8], both arising in the domains of intensive energy deposition. The kinetics of this process for the conditions under consideration was investigated in [5]. This phenomenon can be used for tracing of the discharge regions drifting downstream, determination of the local gas velocities and time of these regions arrival to the BSW. The importance of such kind of information can not be overestimated. To make sure that it is chemiluminescence indeed, the spectrum of this

emission was recorded. It turned out to be continuous with threshold around 400nm, having maximum at about 600nm and then decreasing in intensity with increasing of the wavelength, just as for the mentioned above case. Thus, it can be stated that the observed emission in the afterglow is chemiluminescence of recombination of oxygen atom and nitric oxide molecule (Fig.3.14). Such kind of luminescence also takes place in carbon dioxide (recombination of oxygen atom with carbon oxide molecule), but the rate constant of this process, and, therefore, the emission intensity is approximately 3 orders of magnitude less and can not be observed without rather delicate special measures.

### 3.4. Gas dynamics with MW discharge

#### *a. Flow tracing by weak luminescence*

So, the method of tracing of the discharge regions in air has been worked out. The emission at a given spatial point was recorded as a function of time. Then, this procedure was repeated with definite spatial shift along x-axis. As a result, the set of curves of emission over time was obtained and processed. The sample of such a record is shown at Fig.3.15. It is seen that the most weak is luminescence from the plasmoid which comes first, and the most intensive – the last, which originates from the cone discharge region (the first from the nozzle). At the next picture (Fig.3.16) the x-position of each plasmoid is presented as function of time, and, hence, the local velocity of drift can be determined. This information is shown at the next Fig.3.17. The mean velocity, determined from x-t diagrams for each plasmoid leads to the next values: the first plasmoid –  $0.496\text{mm/ms}$ , the second –  $0.535\text{mm/ms}$ , and the third –  $0.534\text{mm/ms}$ . The velocity dependence over x-axis is in a good agreement with the measurements made by the AD-probes.

#### *b. Determination of MW discharge regions fronts coming to the BSW*

The next important step to be done was determination of MW discharge regions coming to the BSW in order to further synchronize the data from pressure sensors and Schlieren imaging. The moment of discharge region coming is easily determined by rising of emission signal, the last being up to an order magnitude more intensive than in the case of free flow at a fixed spatial point. This information will be presented with the pressure sensors data. Unfortunately, in the most AD model positions the time of arrival of the nearest to the body plasmoid can not be detected now due to the intensive over-lighting from the discharge emission and this is one of the tasks for future diagnostic enhancement.

#### *c. Piezoelectric sensor measurements of total pressure evolution at stagnation point*



Experiments were made for determination of the total pressure evolution at stagnation point during interaction with the MW discharge regions which are drifted downstream the flow after termination of MW pulse. The sensor was installed in such a manner that its central axis coincided with the central axis of the working flow and was faced towards the flow. The sensor position versus the exit section of the nozzle could be changed.

Pressure evolution tracing was made in time interval up to 300 $\mu$ s after the beginning of a MW pulse. The time step was 1.9 $\mu$ s and every point obtained was a result of 5000 averaging. Besides, monitoring of the flow parameters without discharge was made, as well as MW pickup registration. After approximately 15-20 $\mu$ s from the beginning of MW pulse the influence of MW-pickup can be neglected that can be seen while examining the typical examples of pressure evolution, “zero-flow” and MW-pickup. As could be supposed, evolution of pressure shows subsequent passing of the discharge regions according to the visible light emission of the discharge and time shift of these regions coming to the sensor in accordance with changing of sensor position. Experiments were fulfilled at different positions of the pressure sensor – 15mm, 23mm, 29mm, 35mm, 48mm, 63mm, 75mm (nominal position) and 92mm for the case of dielectric-made nozzle. Three positions of the sensor were tested also for the metal-made nozzle – 64mm, 75mm and 89mm.

The summarized data of experimental investigation by the pressure sensor in the case of the dielectric nozzle are shown at 3D graph of Fig.3.18a. The straight “valleys” formed by the discharge regions drift downstream the flow are very well seen at this picture, indicating of the nearly constant velocity of the downstream displacement. This is confirmed by the curves processing shown at Fig.3.18b. It can be seen that the obtained results concerning the velocities are in a good agreement with measurements by the optic method.

Then the experiments with the piezoelectric sensor were repeated and investigations were made in a more wide range of time window – up to 3ms. In this case two MW pulses were inside time window. It can be seen (Fig.3.19) that oscillations of the pressure take place during approximately half of millisecond.

#### *d. Kulite-sensor measurements of total pressure evolution at stagnation point*

Measurements of pressure evolution at stagnation point of the model were also made by the Kulite sensor. The advantages of this device were discussed above, but this sensor demands very careful transient regimes of the flow. In the most experiments the 8mm dia Teflon cover-shirt was used. Pressure evolution was tested by this sensor at the next positions: from 35mm with step 5mm up to 60mm with adding the last point at 63mm; on account of more

recent investigations 4 positions were also investigated – 35mm, 48mm, 63mm and 75mm. Due to the excellent characteristics of Kulite, signals from the single realizations were recorded. Usually, averaging over 100 realizations was adopted (compare with 5,000 in the case of piezoelectric sensor!). The results are shown at Fig.3.20 and several next ones.

It can be seen that the signals from the Kulite are very similar to those from the piezoelectric sensor. Along with relatively low-frequency oscillations one can observe oscillations with higher frequency, sometimes such oscillations are also seen at the graphs obtained by the piezoelectric sensor (at the first tens of microseconds of registration).

Experiments were made also with cover-shirt 12mm in air (Fig.3.20) and with the regular 8mm cover-shirt in carbon dioxide (Fig.3.21). High frequency oscillations are also present here, their period being practically the same.

Pressure evolution was also tested in the case of z-polarization of MW flux.

*e. Schlieren images of MW discharge regions interaction with BSW (air and CO<sub>2</sub>)*

For obtaining the time-dependent images, the Schlieren device operated in regime of time gating. The lighting impulse duration was less than 2  $\mu$ s. Two, five and ten microsecond steps were adopted in these investigations, the overall time window being up to 250 $\mu$ s. For better visualization experiments were conducted not only in air, but in carbon dioxide as well. The possibility of testing of different gases is one of the advantages of the gas dynamic scheme used. It was cleared up that the behavior of carbon dioxide is absolutely the same as air, but the processes run more slowly and the picture quality is better. The last fact is due not only for better optic characteristics, but also for not so bright discharge. Couple of experiments was made in argon, but no visible effect in BSW position or in other demonstration was find out.

*f. Schlieren images of SW from MW discharge channel and its interaction with BSW (CO<sub>2</sub>)*

For better visualization of gas dynamic processes, polarization of MW flux was turned at 90 degrees and electric field vector has become parallel to the main optic axis of the Schlieren device (z-polarization). Thus, the optic length of the signal was increased and more delicate events became visible. Origination and evolution of a SW from a separate MW discharge channel, as well as its interaction with the BSW was registered in carbon dioxide. The optimal spatial position was determined, where the effect had its maximum value due to effective MW energy absorption (the last was confirmed not only by Schlieren images, but by sufficient decrease of the scattered MW signal). The velocity of the SW at the initial phase of propagation is presented at Fig.3.22.

## IV. Kinetic modeling

The main objectives of the presented kinetic modeling is to form a comparative basis with experimental results, which will be useful both for experimental results processing and for better understanding of the background processes under investigation.

### 4.1. Evolution of chemical composition of the discharge

The kinetic and chemical processes in MW discharge and in afterglow, when the discharge region is drifted downstream to the bow shock wave of AD body are to be analyzed numerically to quantify the evolution of MW discharge region parameters. Not less important is to determine plasma parameters and gas composition in zone of discharge region – BSW interaction and to investigate the detailed vibrational kinetic of nitrogen and oxygen, as well as vibrational-translational relaxation of air molecules on oxygen atom at discharge and afterglow stages.

#### 4.1.1. Kinetic scheme

The kinetic scheme for the dry air includes 106 charged and neutral components and about 20000 reactions. Among 106 components 25 are:  $N_2$ ,  $O_2$ ,  $e$ ,  $O$ ,  $O_2^-$ ,  $N_2^+$ ,  $O_2^+$ ,  $N_4^+$ ,  $O_4^+$ ,  $NO^+$ ,  $N_2(A^3S^+_u)$ ,  $N_2(B^3P_g)$ ,  $N_2(a'^1S^-_u)$ ,  $N_2(C^3P_u)$ ,  $O_2(a^1D_g)$ ,  $O_2(b^1S^+_g)$ ,  $N$ ,  $O$ ,  $O(^1D)$ ,  $O(^1S)$ ,  $O_3$ ,  $NO$ ,  $NO_2$ ,  $NO_3$ ,  $N_2O$ . The rest are nitrogen and oxygen molecules which can be excited in all vibrational levels – 48 for nitrogen and 33 for oxygen. Electron-neutral particle processes rate constants are calculated on the base of energy distribution function of electrons which is determined by solving the Boltzmann equation. The detailed vibrational kinetics, including VV, VV' (vibrational quantum exchange between nitrogen and oxygen molecules) and VT processes are under consideration. Chemical reactions - both conventional and with participation of vibrationally excited molecules are in the list.

#### 4.1.2. Results of simulation

Calculations were made for  $p=60 - 100Torr$ , ranges of MW pulse duration  $t = 1.6 - 1.9\mu s$  and reduced electric field  $E/N=107-110Td$ , and relaxation tracing  $100\mu s$  and more. Initial gas temperature was taken 300K. According to the experiment, the MW discharge region was placed at a distance of about 10mm from the BSW, that is approximately  $30\mu s$  of a downstream drift after the MW pulse termination.

In a few microseconds after the MW pulse all the excited electronic states of nitrogen are quenched by molecular oxygen with producing of the O-atoms and vibrationally excited  $N_2$  molecules in a ground state. We do not consider the so-called fast heating here, as it is a

special question of realistic kinetic chain for it and such a scheme is absent now-time. So, only the vibrational kinetics, as well as the kinetics of the main chemical components was of importance at the mentioned above time scale.

**4.1.3. Vibrational kinetics of nitrogen.** The results of calculation of the distribution function over vibrational levels of nitrogen at time points corresponding to the MW pulse termination and the beginning of plasma region interaction with the BSW of AD body are shown at Fig.4.1. It is seen that at the end of MW pulse the VDF is highly non-equilibrium due to excitation of the first 8 vibrational levels of  $N_2$  by direct electron impact. Then, VV-relaxation process leads to establishing of the Boltzmann distribution at the several first levels (including zero level). This evolution is demonstrated at Fig.4.2, where the relative populations (1-0 and 2-1) are presented. VDF at the lower vibrational levels establishes at the time point about 30  $\mu s$  at a level of 1700-1800K. The total energy input in a gas is about 0.4J/cm<sup>3</sup>·atm.

The effect of VDF non-equilibrium at the end of a short MW pulses and moderate energy inputs should be taken into account while discharge spectra processing. For this purpose the dependence of the first vibrational “temperature” (levels 0-1) at the moment of short-impulse discharge termination over energy input is calculated (Fig.4.3). It helps to reconstruct the actual specific energy input at the base of the measured population of the first vibrational nitrogen level.

At a time scale of order 10-100  $\mu s$  the VT-relaxation of vibrationally excited  $N_2$  on the O-atoms is not important – the gas heating due to this process is of order several degrees Kelvin, but at a longer times or at higher energy input this process may be of principal importance. Thus, consideration of a large AD body interaction with discharge plasma regions may demand this process to be taken into account.

**4.1.4. Vibrational kinetics of oxygen.** Vibrational kinetics of oxygen partially resembles that of nitrogen, but is determined by sufficiently less effective excitation of vibrational levels by direct electron impact (of the first 4 levels) and is strongly influenced by effective VT-relaxation on the O-atom. VV' exchange with molecular nitrogen vibrational reservoir is too slow at such gas temperature and energy storage in  $N_2$  vibrations to affect  $O_2$  vibrational kinetics. As a result, the energy storage in  $O_2$  vibrations is rather small, the VDF establishes practically over all the levels up to 32  $\mu s$  at a temperature only 560K. The evolution of the VDF of oxygen molecule is shown at Fig.4.4.

**4.1.5. Kinetics of the main components.** The kinetics of the main components in a discharge and afterglow is presented at Fig.4.5. Such a components are: oxygen and nitrogen atoms, ozone, nitric oxide and electrons. Oxygen atom concentration, as well as nitrogen one are practically constant in a time range from several microseconds to several hundred microseconds. It is seen that oxygen atom concentration attains 2% of molecular oxygen concentration. It is sufficient for  $O_2 - O$  VT-relaxation, but not enough for  $N_2 - O$  VT-relaxation at the time scale under consideration. The process of NO formation takes place via interaction of vibrationally excited nitrogen molecule (with vibrational numbers higher than 15) with O-atom. That is why, the oxidation process goes in spite of low gas temperature, taking place hand by hand with VDF of nitrogen establishing. The rapid conversion of O-atom in the ozone molecule is observed at a time scale more than 100~~ns~~ms.

Electron kinetics is often proposed as very important for different aspects of the problem, but in our case to the moment of interaction with the BSW electron concentration in the discharge region falls to the value about  $3 \cdot 10^{10} \text{ cm}^{-3}$  and seems to be too low for any direct effect on the BSW.

#### **4.2. Electron excitation rate constants modification (Influence of vibrational population on electron states excitation rate constants in nitrogen gas discharges)**

The methods of calculation of electron states excitation rate constants by electron impact in vibrationally excited mediums are based on assumption about the character of vibration distribution function (VDF). Traditionally, the hypothesis about Boltzmann [11] or Treanor VDF are taken into account. In real, in short pulse discharges (when pulse duration is less than the time of VV-exchange) with intensive pumping of low-lying vibrational levels, VDF is neither Boltzmann nor Treanor.

CARS-experiments [12-14] and calculations (see Fig.4.1-4.2, pumping pulse duration is 1.9 $\mu$ s) show that VDF in this case may be described in two-temperature approach. First vibration temperature  $T_{v1}$  is "traditional" one and is determined by vibrational population of zero and first levels. Second vibrational temperature  $T_{v2}$  is determined by population of the levels, which are excited by electron impact (levels 1-8).

The main goal of this work is calculation of the mentioned above rate constants for  $N_2$  with VDF, which is formed in collisional electron-molecule reactions.

The calculations are based on numerical solving of the Boltzmann equation for energy of electrons. This equation is solved in conventional "two-term approach" with taking into account elastic and non-elastic collisions. As a result, the electron energy distribution

functions (EEDF) and related rate constants and drift characteristics of electrons were obtained.

In advance, the review and the tests of the existed and recommended electron impact cross sections sets were carried out. The aim of these tests is to reach the best agreement between the experimental drift characteristics and rate constants of electrons collisions with the calculated ones with vibrational and gas temperatures  $T_v = T_g = 300$  K. Experimental data were taken mainly from [15, 16]. The results of these tests are shown in Fig.4.6 and 4.7.

The rate constants of electron states excitation during the beginning stage of a discharge (when  $T_v = T_g$ ) were approximated as

$$K_0 = A \cdot (E/N)^{-n} \cdot \exp\left(-\frac{(E/N)_0}{E/N}\right), \quad (1)$$

here and below  $E/N$  is in [Td],  $K_0$  - in [cm<sup>3</sup>/s] with error of approximation less than 1%. Coefficients  $A$ ,  $n$  and  $(E/N)_0$  are shown in Table 1.

At the second step the population of vibrational levels as a function of  $E/N$  was determined. Vibrational pumping of  $N_2$  was calculated based on the solving of evolutionary equations for population of 47 levels, taking into account e-V, V-V and V-T processes. Rate constants for forward and reverse e-V processes were taken from previous EEDF calculation. The pumping pulse was interrupted when V-V processes begin to influence on the form of VDF of the low-lying levels. In another words, pumping pulse was limited by the time of V-V-exchange. Calculations show that in short pulses the temperature  $T_{v1}$  is a function of energy deposition into discharge, and  $T_{v2}$  depends on  $E/N$ :

$$T_{v2} = 1.11 \cdot 10^4 \cdot \exp\left(-\frac{47}{E/N}\right). \quad (2)$$

Finally, the dependencies of rate constants for vibrationally excited  $N_2$  by electron impact were calculated. Here EEDF was calculated taking into account super-elastic collisions of electrons with vibrationally excited molecules, which have VDF according two temperatures:  $T_{v1}$  for  $v=0, 1$  and  $T_{v2}$  for  $v=1-8$ . In addition, the influence of vibrational population on the relative intensity of electron-vibrational transitions between ground and excited electron states was considered. In this case for each pair  $T_{v1}$  and  $T_{v2}$  energy dependence of total cross section for mentioned transitions was recalculated according to Frank-Condon principle. Frank-Condon factors were taken from [16]. The calculations result is the correction item for expression (1):

$$K_v = K_0 + B \cdot T_{v1}^{-a + \frac{b}{T_{v2}}} \cdot \exp \left[ - \left( \frac{\hbar \omega_e}{T_{v1}} \right) - \left( \frac{U}{T_{v2}} \right)^2 \right], \quad (3)$$

$T_{v1}$ ,  $T_{v2}$ , vibrational quantum  $\hbar\omega_e$  are in [K]. Coefficients B, a, b, U and approximation errors are shown in Table 2,  $K_0$  is expression (1),  $T_{v2}$  is dependent value and can be determined from expression (2) as a function of E/N.

The rate constants which are calculated in two-temperature approach (3), when  $T_{v2} > T_{v1}$ , are greater than the corresponding values which are calculated in «traditional» approach- for single-temperature VDF. The differences are:  $\approx 30\%$  at  $E/N = 80$  Td and  $\approx 10\%$  at 150 Td.

The expression (3) for rate constants of electron states excitation is applicable for the ranges: energy deposition in discharge 0.005-0.5 J/cm<sup>3</sup> atm, reduced electric fields 80-150 Td.

#### 4.3. Discharge parameters evolution during active phase

Determination of an actual discharge parameters during its active phase demands taking into account electrodynamic interaction of the discharge structure with an external electric field. For this purpose calculations of the local parameters of discharge in its active phase in air were made at the base of electrodynamics of discharge channel and simplified kinetics in it.

The discharge channel was treated as an ellipsoid of revolution, depolarization factor being of order 0.1 – the value, which was determined both from discharge channel's shape and electric field distribution analysis. The form of the MW signal was taken as it was recorded in experiment without discharge. Thus, it had a short (with duration of order of 0.1μs) initial peak, which exceeded the following part of impulse by 15-20%, and a slow (about 10%) decrease of an amplitude to its end. By variation of an external E/p parameter, the fitting of a calculated optical signals from  $N_2(C^3P_u)$  state with the recorded ones was being attained. The results of such procedure are shown at Fig.4.8.

Three parameters define the shape of an optical signal – delay, raising tempo and inclination of descending part. The influence of the first burst of MW signal on the delay time is decisive. The raising tempo is defined by the mean value of E/p parameter. The inclination part is determined by cooperative influence of depolarization factor value and the descending part of MW impulse. It can be stated definitely, that the most probable value of E/p parameter in the first plasmoid lies in the range 38-39V/cmTorr, that is in a good agreement with electric field measurements. This gives foundation to determine the interval of specific

energy input in the nearest to the model channel as being  $50\text{-}120\text{mJ/cm}^3$ , whereas the ultimate electron concentration to the end of MW impulse as  $(2\text{-}3)\cdot 10^{13}\text{cm}^{-3}$  at 60Torr of normalized air pressure.

The dynamics of the second plasmoid is greatly influenced by the others, therefore, it begins to burn sufficiently later than the first one. For this reason energy input in this channel is less, attaining only  $30\text{-}50\text{mJ/cm}^3$ . The influence of the model position, as well as fluctuations in MW flux distributions (maximums positions) leads to re-distribution of the absorbed energy in these two plasmoids. Another set of light emission evolution from plasmoids is shown at Fig.4.9.

#### 4.4. Gas dynamics effect evaluation (numeric calculations)

Several numeric tests were made to obtain the reference data scale for the main measured values – first of all the pressure and translational temperature at stagnation point of the model. Calculations were provided in the frames of Euler equation which in our case is adequate for determination of the mentioned above parameters. The problem was considered as cylindrically-symmetric, i.e. 2D, it corresponds rather to MW discharge region formed by a circular polarized radiation than that of linear one.

Interaction of AD model in  $M=1.4$  airflow with one and two “plasmoids” was modeled. The last were treated as elliptic spatial regions with decreased density and higher temperature, the last being in exceed of 50K in comparison with surrounding media temperature. The dimensions and position of the discharge areas and AD model ( $R=1\text{cm}$ ) are shown at Fig.4.10. Results of calculations are presented at Fig.4.11. The effect from each plasmoid can be linearly added to obtain the summary action, in the case of calculation each region delivers minus ~~750Torr~~ms. It should be noted that calculations show insignificant change of the BSW front position while the heated regions are passing, just of the order of that are registered in experiment at the latest phases of interaction, when the region is blown down and acoustic tail comes.

## V. Discussion

The results obtained give us opportunity to reconstruct the sequence of events in the physical system under consideration with high degree of probability.



### 5.1. Synchronizing of Schlieren, Kulite and optics

As it was mentioned earlier, there is an interval of AD model (Kulite) positions where the nearest to it plasmoid – channel-type - occupies the same place versus the model – plasmoid's y-axis of symmetry is about  $10mm$  from the model surface. This interval is  $40 - 65mm$ , after it all plasmoids occupy their regular places, as in the case of free flow (without AD model). Just in this spatial interval the most investigations have been made. Thus, due to this fact the first reaction of the Kulite-sensor begins at the same time –  $25 - 27ms$ . It means that the first gas dynamic disturbance has arrived to the sensor surface about this moment. The first changing in the Schlieren picture starts at about  $7ms$  time point and it indicates of very important fact - this disturbance is the nearest boundary of plasmoid defined via its integral luminescence. As the total width (along x-axis) of plasmoid defined in such a way, is about  $4.4mm$ ,  $7ms$  is just the time interval for  $10-2.2-4=3.8mm$  distance overcoming in a free drifting. Additional  $10ms$  are needed for reaching the surface of the model and about  $10ms$  more – for the sensor surface (it is shifted up the model for protection reasons) and delay in its reaction. Thus, about  $20ms$  in total is the standard shift between Schlieren (at BSW standard position change) and Kulite reaction. At  $17-19ms$  the back front of the disturbance comes together with the maximum of this plasmoid chemiluminescence (the last is obtained by reverse one-step extrapolation). At  $63mm$  position, where there are 3 plasmoids, the second comes to the BSW region at about  $39-40ms$ , the back front of it being passed at  $49-51ms$  (Schlieren) together with the second peak of weak luminescence. All this period of time Kulite signal linearly goes down, attaining its minimum at  $80ms$ , i.e.  $60ms$  in Schlieren scale. Then the signal begins to grow up. The front disturbance from the cone comes at  $85-87ms$  and its back front – at  $103-105ms$  together with the third peak of weak luminescence ( $110ms$ ). Meanwhile, the Kulite signal reaches local maximum at  $110ms$  (i.e.  $90ms$  in Shlieren scale) and then begins to fall down, coming to local minimum at  $136ms$  ( $116ms$ ). Thus, practically absolute synchronization in three different diagnostics is demonstrated (Fig.5.1, 5.2).

### 5.2. Spatial-temporal picture of interaction

The catalog of phases in the near AD model gas dynamic behavior was obtained and it seems to be universal, at least it is true for air and carbon dioxide. The sequence of phases is shown at Fig.5.3. The process of interaction begins with coming of the front of disturbance to the BSW. The visual gradient begins to shift towards the model front surface, passing through 2 characteristic phases of pressing on – with single and double discontinuity. Then a short period of absolute instability (bifurcation phase) comes when no discontinuities are

seen. After this a sudden “jump off” of a SW takes place, its position being as far as up to twice in comparison with standard position. Also the pressed SW is seen which is moving from the surface to the moved away. At the moment when these waves unify, the back front of the disturbance comes to this wave position. This stage of the disturbance passing through the BSW takes *10-12ms* for the channel-type disturbance and *25-27ms* for the cone-type disturbance in air. In CO<sub>2</sub>, these values are about *15-17ms* and *35-40ms*, correspondingly. Then the phases of gradual returning back to the standard position, passing it and continuation of moving towards AD model take place. At the moment the back front of the disturbance is well seen. It can be added that this moment coincides with coming of the maximum of light emission of chemiluminescence. After this element is blown down through the front domain of the AD model, the movement of discontinuity changes direction and the reverse movement to the standard position begins. Once again the second discontinuity can be seen closer to the model front surface. At last the BSW takes its standard position, but for some time very small fluctuations of the BSW position can be detected. Then any visible changes in the picture terminate. This part of cycle takes *35-40ms* in air and *60μs* in CO<sub>2</sub>, time scales are given for the cone disturbance interaction with 8mm AD model diameter. The identical picture is also seen from interaction of the channels with the BSW region, the only exception is that the phases after coming of the back front of disturbance are not distinguished due to coming of the next disturbance. As the conic disturbance is the last, all phases can be retraced.

The forming of a cone disturbance and its path to the AD model region can be retraced in CO<sub>2</sub>. Images are obtained from the both (y- and z-) projections, showing some disturbance of symmetry in this domain due to the presence of channel-like region inside it. After several microseconds after the MW pulse, the cone surface which was covered by the discharge, begins to spread in normal (to the surface) direction and a normal shock appears instead of the cone apex. The back front divides the disturbed and non-disturbed (up the flow) regions, where all stationary inhomogeneities are well seen. Then this disturbance drifts downstream, its shape highly resembles a “bug”. The phases of interaction of a “bug” with the BSW are just the same as for the channels, but more extended in time due to the domain dimension. The picture of a flow in the standard cone position relaxes slowly through different stages until recover its initial geometry. This moment coincides with the BSW final returning back to its standard position. These pictures can be seen at Fig.5.3. The figure in the right upper corner of each frame is time interval (in microseconds) after MW pulse. Better

quality frames, as well as movie of the process, obtained by image processing procedure are presented in Supplement and Gif-file.

### 5.3. Energy input and local parameters of discharge

As it was shown above, analysis of the shapes of optic emission evolution along with such of the MW signal allowed to determine energetic characteristics in air discharge regions. Simultaneously, treatment of review spectra allowed to determine vibrational temperature of the first level of the ground state, which turned out to be about 1400-1500K at the end of MW pulse. According to the results of kinetic modeling this value corresponds to specific energy input of order  $100\text{mJ/cm}^3$ . This value is in the interval obtained above. Thus, the typical specific energy input in discharge channels in air is about  $1.0 - 1.2\text{J/cm}^3\text{atm}$ , of taking the value of channel volume of order  $0.3\text{cm}^3$ , 30-40mJ per channel, or 25-30mJ/cm. Of course, only about 10% of these values is deposited instantly in translational degrees of freedom.

For carbon dioxide estimation of energy input can be made on the basis of SW formation from a discharge channel. Examination of a graph presenting SW velocity dependence over time (Fig.3.22) leads to the conclusion that process can be modeled both by a piston action (initial stage) and the cylindrical explosion (stage of SW propagation). Thus, the heated region of a channel with initial radius of 1.2mm spreads with sound velocity of surrounding gas, leading to the SW formation. Estimation according to this imagination gives the value of energy release (in a form of heat) per unit length of order 5-7mJ/cm.

*Gas heating in plasmoids.* Fast gas heating was observed both in air and in  $\text{CO}_2$ . This phenomenon has been discussed in papers [5, 9, 10]. It should be noted here that in our present experiments the level of MW power was somewhat higher in comparison with the previous ones. Therefore, the final temperature in plasmoid turned out also to be higher. For the first time we began temperature monitoring of different plasmoids in air, and it turned out (for both y- and z-polarization) that the cone plasmoid is colder than channels – it is not surprising taking into account more bulk character of the first structure. But the temperature difference in domains is more than  $70\text{K}$ , as the initial temperature near the nozzle is higher. Thus, the ultimate difference is about  $80-90\text{K}$ , the scale of temperature rise in the channel being of order  $100-120\text{K}$ , or heating rate about  $100\text{K}/\mu\text{s}$ . The level of heating in the case of z-polarization is several tens degrees of Kelvin less than in the case of y-polarization. The question is what part of a channel-type structure has such a temperature – very thin filament (dipole itself), or the surrounding “fur”. From one hand, the temperature inside a filament

should be higher, as well as the brightness of the emission intensity. From the other hand, the volume of the filament is sufficiently less than that of the environment and the contribution of the filament in the over-all luminescence can be small. In such case the delicate examination of the upper rotational levels population is needed. This problem demands more careful investigations. The same can be stated for the cone region. As the cone plasmoid is an extended formation (of about  $12\text{mm}$  along x-axis), measurements of temperature distribution will be assumed.

Another interesting phenomenon is observed, which can be explained by cooperative action of discharge and gas dynamics. The image of discharge structures, especially this is refer to the channels, are not fuzzy. Indeed, even at efficient time of intensive luminescence of about  $3\text{ms}$  the shift of image details should have been at least  $1\text{-}1.5\text{mm}$  that is quite detectable. May be the reason for it is that the MW discharge regions are locally decelerated in the process of energy input. In favour of this supposition also indicates the fact of shifting of the maximum of weak luminosity to the back front of the disturbance not only in the case of the cone structure, but in channel-type as well. All this together with the existence of bifurcation (see above) and “jump-off” phases puts a problem of internal plasmoid conditions and inter-plasmoid gas dynamics.

Thus, the energy density release in MW discharge channels is high enough to form the SW from the channel. The characteristic dynamic length is of order  $4\text{-}5\text{mm}$ , that leads to SW-BSW interaction at the initial stages of gas dynamic phenomena.

#### **5.4. Shock-shock and shock-density (thermal) well interaction**

Two types of gas dynamic disturbances from MW discharge were obtained and their interaction with the BSW was investigated – shock-shock and shock-density (thermal) well. As it was mentioned above, in the interval of  $40\text{-}75\text{mm}$  AD model position the nearest plasmoid is the channel. It originates at a distance  $8\text{-}10\text{mm}$  from the AD body front surface and  $4\text{-}6\text{mm}$  from the BSW at its standard position. Thus, interaction of gas dynamic disturbance from a channel can be realized as SW-BSW. The process of shock-shock collision leads to amplification of the weaker wave, appearing of the density jump, extra-compression of the gas behind the stronger wave and its deceleration in laboratory frame due to this process. These events after some time are influenced by interaction with the model surface. Thus, the picture of interaction in this case is rather complex. Also, two waves from the channels are interfering at spatial domain between them. All this, including interaction with density “holes” in a gas where the “explosions” took place, leads to the stagnation

pressure behavior which is registered by the Kulite sensor. Further analysis is needed to make more definite conclusions.

Also energy release in the domain of oblique shocks intersection was observed. The appearance of a disturbance in this region after MW energy input can be seen at a Schlieren images. After some time it takes form of a “bug”, traveling downstream the flow at practically constant velocity. Its interaction with the BSW of a model was described above.

### **5.5. Experimental modeling of action at high repetition rate**

While the AD model is displaced along x-axis, 3 types of interaction regimes of AD body with MW discharge regions are realized (all as a consequence of one MW pulse):

1. Interaction with one plasmoid, i.e. conic (model positions up to  $x = 35\text{mm}$ ).
2. Interaction with two plasmoids, one of them is MW channel, the other – conic ( $x = 40 - 50\text{mm}$ ), the time interval between them in air being changed from 30 to  $60\mu\text{s}$ .
3. Interaction with three plasmoids, two of them are MW channels, the last – conic ( $x = 55 - 70\text{mm}$  and more), the time interval between first two in air being changed from order of 10 to  $34\mu\text{s}$ , after 70mm the intervals between plasmoids coming become nearly constant,  $34\mu\text{s}$  and  $60\mu\text{s}$ , correspondingly.

Thus, the effect of high repetition rate (30 – 100kHz) was modeled to some extent. This situation is also being reflected in the character of Kulite signals while changing its position (Fig.5.4) and is discussed below. It is seen that the amplitude of pressure diminishing is of order 20 Torr (regular for 8mm AD model diameter) – 30 Torr (the ultimate value that has been registered for 12mm AD model diameter). In this case, the regular value seems to be invariant to the type of effecting MW discharge region – it can be seen both from Kulite signal at 35mm position and while analyzing the signals behavior at 63 – 75mm positions together with the weak luminosity evolution at the same positions. In air the characteristic duration of negative phase for the first two discharge plasmoids is of order  $70\mu\text{s}$  and for the cone one – 35-40 $\mu\text{s}$ , but these conclusions are not final, further analysis is required. Carbon dioxide is less “reactive” than air, it is seen from the appropriate Kulite curves, but the general structure of the signals is close to that in air. The time scales ratio in carbon dioxide and air seems to be guide by the ratio of their densities, the necessity of further analysis completely refers to this item as well.

The optimal action of discharge domains can be find as an integral of pressure signal over time. The results are shown at Fig.5.4, 5.5. It is seen that the effect rises with increasing the distance from the nozzle, being even of an opposite sign (drag rise) at initial positions

(35mm) and having maximum (or saturation?) as high as  $1200\text{--}1400\text{Torr}\cdot\text{ms}$ . at a distance of 55mm. It can be supposed that every disturbance gives about  $450\text{Torr}\cdot\text{ms}$  of final effect, but regarding that before this point there are only two plasmoids, the effect from each may reach  $650\text{Torr}\cdot\text{ms}$ . Despite the peak values of pressure diminishing depends on the model size (in about linear proportion), the integral effect is not so sensitive to the model size. At the first sight it is also surprising that the maximum effect in carbon dioxide is almost the same as in the case of 12mm model in air. Compensation comes from the “oscillatory tail” of the disturbance, which influences sufficiently the final integral effect value.

Thus, the influence of temporal sequence of the coming disturbances is evident and will be also discussed below, due to a number of circumstantial interconnected aspects the analysis given should be considered as preliminary one.

*Oscillations and oscillatory model.* Two characteristic frequencies are present in pressure sensors data in air – relatively low frequency ( $18\text{kHz}$ ) and high frequency ( $128\text{kHz}$ ). The HF oscillations, which, without doubt, are launching by/coming with the front of disturbance are present in all tests and their frequency is independent neither the AD model diameter, nor the gas nature (air, carbon dioxide). But damping coefficient depends upon the model position. It should be noted that these HF oscillations are excited by the MW channel structure, and not by the cone one. One of the supposition is that these oscillations are the HF sound which is excited in the hollow of AD front surface (“whistle”). Amazing is the fact that the amplitude of these oscillations decreases sufficiently with change of the electric field polarization (from y- to z-).

The intensity of the low frequency disturbances (at least their tail) is a straight function of the intensity of discharge in a cone. This can be seen by comparison of Kulite signals in the case of metal and dielectric nozzles as it was done above. Thus, the conclusion can be made that the low-frequency oscillations are launching by/coming with the back front of the cone disturbance. They can be treated as an acoustic tail, at least this is quite reasonable supposition.

Careful examination of the obtained set of pressure sensors data suggests as if the process under consideration obeys somewhat oscillatory process, the main parameters of which – frequency and damping – can be determined from signals treatment at latest time moments. Such a model was investigated, the Kulite signal being as a solution of equation, and the right –hand side was obtained, i.e. the effecting “force”. The results of such treatment (for  $T = 70\text{ms}$  and  $damp=1/33\text{ms}$ ) are quite rational.

### 5.6. Optimization of the effect - Effectiveness parameters of action

*What structure is better?* We have examined two principle types of discharge plasma structures – cylindrically symmetric, rather homogeneous and extended in the direction of a flow, and highly non-uniform, filamentary, elongated in the direction perpendicular to the flow axis structure. It is surprising that the first one (or two) filamentary creations which are approximately parallel to the BSW exert even more strong (at least the same) action as the cone plasmoid. This conclusion can be confirmed by inspecting of Kulite (Fig.5.4) and piezoelectric sensors data. By present understanding it can be associated with a shock-type energy release in a channel plasmoids.

Another data can be obtained by comparison of action in the case of linear and circular polarization (Fig.5.7). In the case of circular polarization all plasmoids have cylindrical symmetry (the exact action of the cone plasmoid in both cases is additional evidence in favour of its symmetric structure). Thus, concentration of energy gives better effect regardless of mutual spatial orientation of plasmoid and the BSW. The scale of this discharge region action also can be found from comparison of pressure sensors data at the same position, but for the cases of metal and dielectric nozzles (Fig.5.6) – in the last case the plasmoid is greater, as the MW field is not screened by the metal and the discharge is not burning at the edge of the nozzle. From the curve of integral action also the conclusion can be made that energy concentration is better – model position at 55mm is the case when the plasmoids are concentrated the most closely.

Thus, the preliminary conclusion can be made that the effectiveness of filaments is higher, as at practically the same absorbed energy the effect in pressure reduction is more. It should be noted that the mean temperature in the cone plasmoid is less than in the channels. Model position was one of the parameters for effect optimization – it attained 15% in the position 55mm.

*Model dimension (possible scaling).* The next parameter was AD model dimension. Variation of this parameter was limited by the working flow diameter, therefore, could be changed up to 12mm. Experiments showed increase of the peak pressure reduction (also at 55mm of model position) up to 29Torr in comparison to 19Torr for 8mm model under the same other external conditions. It means that the peak value of stagnation pressure reduction increases linearly with the model diameter. But the integral effect over time at stagnation point differs not so strong, mainly due to the action of “acoustic tail”.

*Discharge organization.* Effectiveness of MW energy use is also important parameter. It evidently increases with increase of absorption coefficient and decrease of time delay in discharge origination. This can be achieved by the proper choice of MW impulse shape. Partially such shape was realized in experiments. MW impulse should consist of two parts – initial powerful very short burst and subsequent pumping part with lower intensity and larger duration, the last is the control parameter for energy input in a flow. Above records of the scattered MW signal from the discharge were presented, which showed that the absorption coefficient could be very high. The influence of radiation polarization – linear, or circular – was already discussed. The last important parameter is mutual orientation of electric field vector in linearly polarized wave and the vector of flow velocity. All the results presented refer to the case when they are perpendicular to each other. Pilot experiments when these vectors were parallel were also conducted, the results are given in Supplement.

*Model position in respect to MW discharge.* Investigation of stagnation pressure behavior while moving the model away from the domains of MW energy release has shown strong decrease of the effect (Fig.5.8). For example, model displacement from 75mm to 100mm position, i.e. changing the distance from the first plasmoid to the model surface from 15mm to 40mm leads to the pressure amplitude of the effect diminishing more than 2-3 times. As the time of gas element drift downstream the flow at 25mm is about 50~~ms~~ $\mu$ s, the process of thermal conductivity and appropriate gas cooling is ineffective. Therefore, it can be supposed that gas in plasmoids is turbulent and this is in agreement with a shock-type of energy release in a channels. The fact of gas cooling under these conditions was confirmed by the measurements made by thermocouple. Where as the mean temperature rise at 80mm position was 2.5K, this indicator for the 120mm position turned out to be only 1K. Thus, the optimal distance between AD-model and MW discharge exists and should be determined in every specific case.

### **5.7. Nature of the effect**

Let us summarize the results obtained.

1. The effect of stagnation pressure reduction is directly proportional to energy concentration in plasmoids.
2. It is also proportional to the measured gas temperature rise in air – the higher temperature, the more pronounced effect is observed. For the metal nozzle: under y-polarization the mean temperature increase is about 120-140K and stagnation pressure difference about



22Torr; under z-polarization the mean temperature increase is about 90-100K and stagnation pressure difference about 17Torr.

3. The temperature of the cone plasmoid is less than in the channels and the credit of it in effect at model positions where all discharge structure elements are realized is less despite of more extended dimensions.
4. The effect scale, calculated numerically under the gas heating which was determined from the experiments is in the range of that obtained experimentally.
5. No visible influence on the BSW in argon where heating is small for the conditions realized.
6. Decreasing of the pressure reduction value with model displacement downstream the flow along with the mean temperature.

These facts evidence in favour of the thermal basis of the drag reduction effect. The unusual behavior of the BSW – splitting in 2 or 3 waves, large values of stand-off, SW disappearance or instability – can be explained by taking into account the amplitude and structure of gas dynamic disturbances which interact with the BSW, as well as relaxation processes which are rather actual due to high energy density in (channel) plasmoids and are intensified after the shock. Thus, the phenomenon has a complex character and includes delicate aspects of standard gas dynamics and non-equilibrium kinetics. But the final conclusions can be made after full-scale modeling.

## Questions

Several questions are of principle importance:

- What are the conditions inside the cone region and filaments?
- Why we do not see the BSW for some time interval and easily see it in other periods of disturbance passing through?
- Why the BSW position evolves in such a wide range?
- What is the nature of oscillatory processes – they are launched by, or come with the disturbance, but is their nature physical or system?
- What is the reason for fast decreasing of the pressure amplitude with moving of AD model away from the domain of MW energy release?

## Summary

We understood well the great importance of diagnostics for solving the problem itself and for providing modern experiment in such a complicated area as plasma aerodynamics. Most of experiments in this field can not be analyzed properly for the lack of essential information about the main discharge-flow parameters. Therefore, we've strengthened our efforts firstly on working out an appropriate diagnostic tools. We have sufficiently moved ahead in this direction and now in our experiment we obtain synchronized information about:

- The discharge regions drift downstream the flow (velocity and position) from their creation to interaction with the BSW with spatial resolution about 1mm and temporal 1 $\mu$ s
- Schlieren images of gas dynamic inhomogeneities evolution (discharge regions, BSW, their interaction, etc.) with time step 1 $\mu$ s
- Stagnation pressure evolution with time resolution less than 1 $\mu$ s (at models with different shape)
- The integral and spectral light emission evolution from different discharge regions during MW discharge burning and afterglow
- Spectra for gas and vibrational temperatures determination in different discharge regions
- Reflected MW signal evolution during discharge burning
- Integral and speed photo-registration of discharge structure at active phase and in afterglow
- Integral drag, lift and their variation while discharge operation (by tenzo-balance)
- Integral thermal effect and its variation while discharge operation (by thermocouple)
- Schlieren images computer processing and processing methods for emission spectra of a discharge are worked out, as well as kinetic models.

Experiments are available in different gases and mixtures, most of diagnostics are valid not only for air, but for other gases as well. Investigations were made in air, nitrogen, carbon dioxide and argon. Additional important feature is possibility to organize different mutual orientation of MW energy flux and gas flow (parallel-perpendicular) and MW polarization (linear-circular). This is important for finding out of efficient schemes for energy deposition.

**All this allowed to obtain spatial-temporal picture of evolution of MW discharge regions from their creation in SS flow to their interaction with the BSW of the AD body and quantify the main discharge-flow parameters.**

Based on these achievements in diagnostics the comparative investigation of the nature of the phenomenon has begun, as well as optimization of MW discharge organization. Thus, the following investigations were fulfilled in a frame of the Project:

- Detailed spatial-temporal investigation of MW discharge in supersonic flows ( $M = 1.7 - 1.8$ ) and its action on AD-bodies is carried out
- MW discharges in SS flows of  $N_2$ , Ar and  $CO_2$  are obtained
- Different regimes of MW discharge domains action on AD-model are realized and investigated
- Method of MW discharge domains downstream drift tracing is worked out and adopted
- Evolution of the total pressure at stagnation point of AD-models of different dimension in SS flows of the mentioned above gases is registered
- Schlieren images with high temporal resolution of MW discharge regions interaction with the BSW are obtained
- Comparative investigation of action of MW discharge regions formed by linear and circular polarization in airflow is fulfilled
- More detailed investigation of discharge structure in the tested gases is done
- Gas temperatures in different discharge regions in air are measured
- Vibrational temperature is determined, as well as energy input in plasmoids
- Electric field distributions over three coordinates are measured in the focal region and absolute values of electric field strength are obtained
- Detailed modeling of kinetic processes at all stages of discharge evolution, including deep afterglow is fulfilled
- Pilot numeric modeling of gas dynamic processes has begun
- Oscillatory processes in stagnation pressure evolution are revealed
- Phases of the SW-BSW, BSW-density well and energy release in domain of oblique shocks interaction are registered
- Zones of the BSW instability are determined
- Data obtained by the different diagnostic channels are synchronized and the detailed picture of the phenomenon under investigation is lightened

- Preliminary analysis of the results obtained is carried out and presented, the most important questions to be answered are formulated.

The investigation stage is now in progress, but several main (preliminary) conclusions can be announced:

- The basis of drag reduction effect seems to be provided rather by thermal mechanism than non-thermal one.
- The effect value increases with concentration of energy deposition.
- The BSW position evolution can not be explained in terms of simple heating model.

The general conclusion to be done is that the physical nature of the phenomenon is very rich and future investigations will afford us new revelations.

More detailed information of the results obtained and additional conclusions will be presented in the Supplement to the Final Report, as well as the steps for creation of high-efficient MW-energy deposition system.

**Thermal mechanism – not the end, but the beginning of the way.** Discussion about thermal or non-thermal mechanism of drag reduction which took place during the last years put out of focus thermal method realization and investigation as more “trivial”. Meanwhile, this mechanism is not less interesting and promising, as non-thermal one, but is not surrounded by some kind of mystic. Investigations by numeric modeling made both in Russia and the USA [19] has shown very important consequences for this method application:

- Gas heating in front of AD-body can be very effective in terms of energy utilization for drag reduction, for example, using of 1.5% of airflow energy for this purpose can reduce drag twice at Mach 6.5 (compare with [18]).
- The effect value rises with increasing of Mach and Reynolds numbers.
- Not only drag, but also lift and pitch can be influenced effectively.

Thus, thermal mechanism seems to be promising for hypersonics. But there are several fundamental problems which are to be solved on the way to this method realization, and may be the main – to heat effectively gas (air) by means of discharge in hypersonic flow. The next one is to organize the energy deposition region structure properly, as it should be rather thin and placed at a special position in front of the body. These are a challenging problems for electrodynamics, gas dynamics, plasma physics and kinetics. To present understanding, this problem by its physical basis is as rich, as thermonuclear one. That is why thermal mechanism application designates not the end, but the beginning of the way to creation of real technology with using of all plasma physics potential.

## Conclusion

The principle step in investigation of MW discharge in SS flows has been made. Probably, for the first time in the area of plasma aerodynamics, the detailed spatial-temporal data of discharge domains evolution and interaction with the BSW were obtained. They include synchronized information from optical emission diagnostics via using of hemiluminescence for discharge regions tracing, from the pressure sensors, which provide information about temporal evolution of the total pressure at stagnation point and Schlieren pictures available with time step of order of microsecond. All this, together with additional information about real discharge structure and gas temperatures in different plasmoids allowed us to reconstruct the sequence of events in the process of discharge regions – AD model interaction, to formulate the regularities of such interaction and to eliminate those questions which are to be answered in further investigations. Preliminary conclusions about the thermal nature of the phenomenon are presented.

## Acknowledgments

Our deep gratitude is addressed to the European Office of Aerospace Research and Development (EOARD) and personally to Dr. Charbel Raffoul for the support of this work. We are also grateful to Dr. Steven Walker, Dr. Julian Tishkoff and Dr. David Van Wie for their encouraging interest.

## References

1. Workshop on Weakly Ionized Gases, USAF Academy, Colorado, 9-12 June 1997. Proceedings.
2. 2<sup>nd</sup> Workshop on Weakly Ionized Gases, AIAA, Norfolk, 24-25 April 1998. Proceedings. "Microwave Plasma Influence on Aerodynamic Characteristics of Body in Airflow", P.193.
3. V.G. Brovkin, Yu. F. Kolesnichenko, S. B. Leonov et. al. "Study of Microwave Plasma-Body Interaction in Supersonic Airflow", 30<sup>th</sup> AIAA Plasmadynamics and Lasers Conference, June 28-July 1, 1999 / Norfolk, Virginia, AIAA 99-3740.
4. V.G. Brovkin, Yu. F. Kolesnichenko, A. A. Gorynya et. al. "Microwave Plasma-Body Interaction in Supersonic Airflow", Proceedings of Workshop "Perspectives of MHD and Plasma Technologies in Aerospace Applications", Moscow, IVTAN, 1999, pp. 78-81.
5. Yu.F.Kolesnichenko, D.V.Khmara. "Plasma-Chemical Composition of Airflow in MW Discharge, Relaxation Zone, and Under Interaction with Bow Shock Wave of AD Body". Second Workshop "Magneto and Plasma Aerodynamics in Aerospace Applications", Moscow, IVTAN, 5-7 April, 2000.
6. Yu. F. Kolesnichenko, V.G. Brovkin, A. A. Gorynya et. al. "Investigation of AD-Body Interaction with Microwave Discharge Region in Supersonic Flows", 39<sup>th</sup> AIAA Aerospace Sciences Meeting & Exhibit, 8-11 January 2001 / Reno, Nevada, AIAA 2001-0345.
7. V.G.Brovkin, Yu.F.Kolesnichenko. "Structure and dynamics of stimulated microwave gas discharge in wave beams". J. Moscow Phys. Soc. **5** (1995) 23 - 38.
8. A.M.Pravilov. Photoprocesses in Molecular Gases. Moscow: Energoatomizdat, 1992 (in Russian).
9. J.D.Kelley, G.V.Candler. "Flowing Air Plasmas: Kinetics, Relaxation Rates, and Flow Dynamics". Second Workshop "Magneto and Plasma Aerodynamics in Aerospace Applications", Moscow, IVTAN, 5-7 April, 2000.
10. G.V.Candler and J.D.Kelley. AIAA Paper No.99-0418, Jan. 1999; No.99-4964, Nov. 1999
11. N.L.Alexandrov, A.M.Konchakov, E.E.Son, Rus: "Fizika plasmy" (Physics of plasma), 4, 5, 1978, p.1182
12. S.I.Valyansky, K.A.Vereshagin, V.Vernike et al., Rus: "Kvantovaya elektronika" (Quantum electronics), 11, 9, 1984, p.1833
13. A.A.Devyatov, S.A.Dolenko, A.T.Rakhimov et al., Rus: "Zh.ETF" (Journal of experimental and theoretical physics), 90, 2, 1986, p.429
14. B.Massabieaux, G.Gousset, G.Lefebvre et al., J.Physique, 48, 1987, p.1939
15. J.Dutton, J. Phys. Chem. Ref. Data, 4, 3, 1975, p.577
16. W.Roznerski, K.Leja, J. Phys.D: Appl.Phys. 17, 297, 1984
17. A.Lofthus, P.H.Krupenie, J. Phys. Chem. Ref. Data, 6, 1, 1977, p.113
18. R.G.Adelgren, G.S.Elliott. D.D.Knight et al. "Energy Deposition in Supersonic Flows", 39<sup>th</sup> AIAA Aerospace Sciences Meeting & Exhibit, 8-11 January 2001 / Reno, Nevada, AIAA 2001-0885.
19. D.W.Riggins and H.F.Nelson. "Hypersonic Flow Control Using Upstream Focused Energy Deposition", AIAA Journal, v.38, No.4, pp.723-725.

## Scheme of Experimental Installation

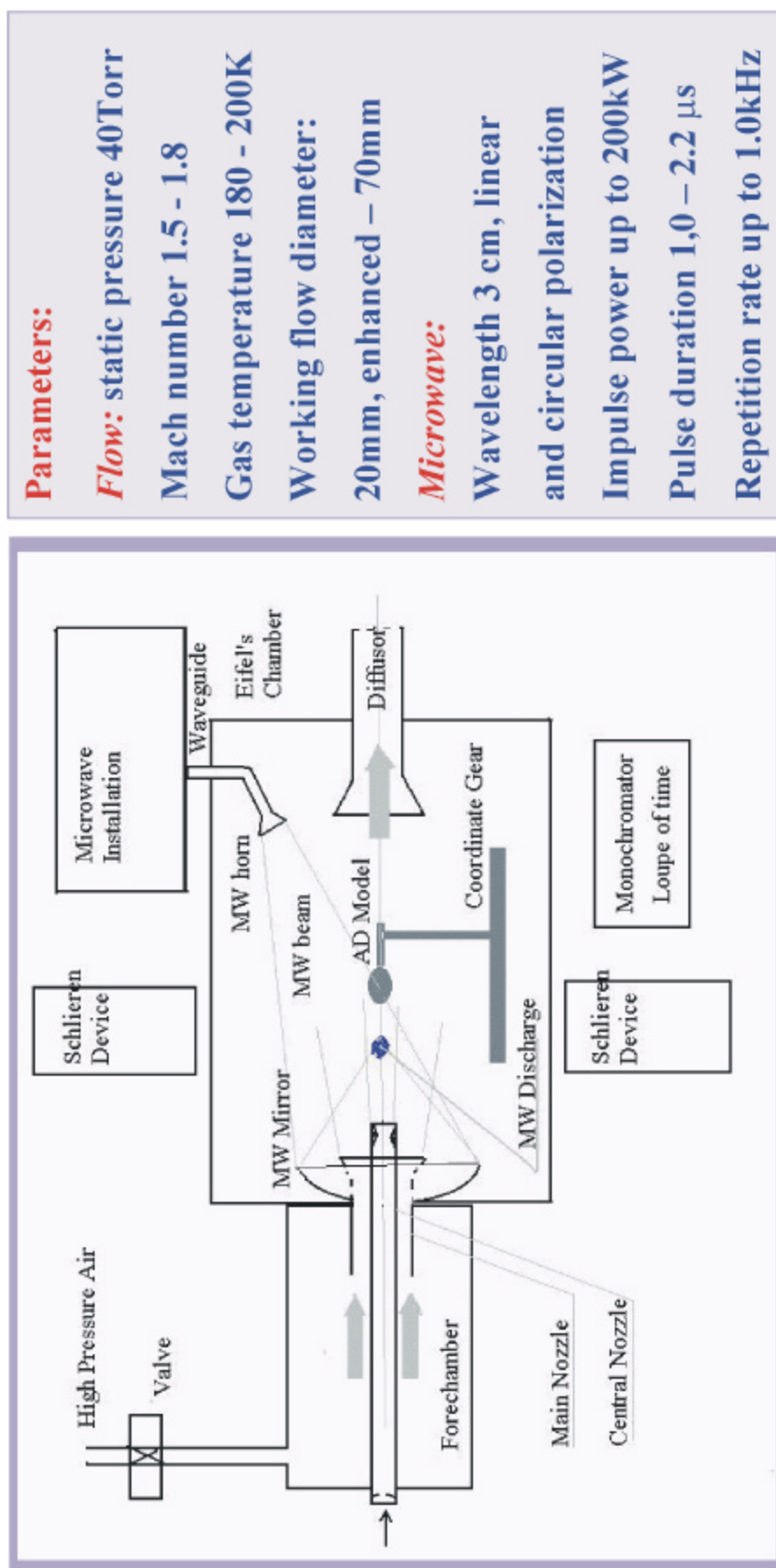


Fig.1.1. General scheme of installation.

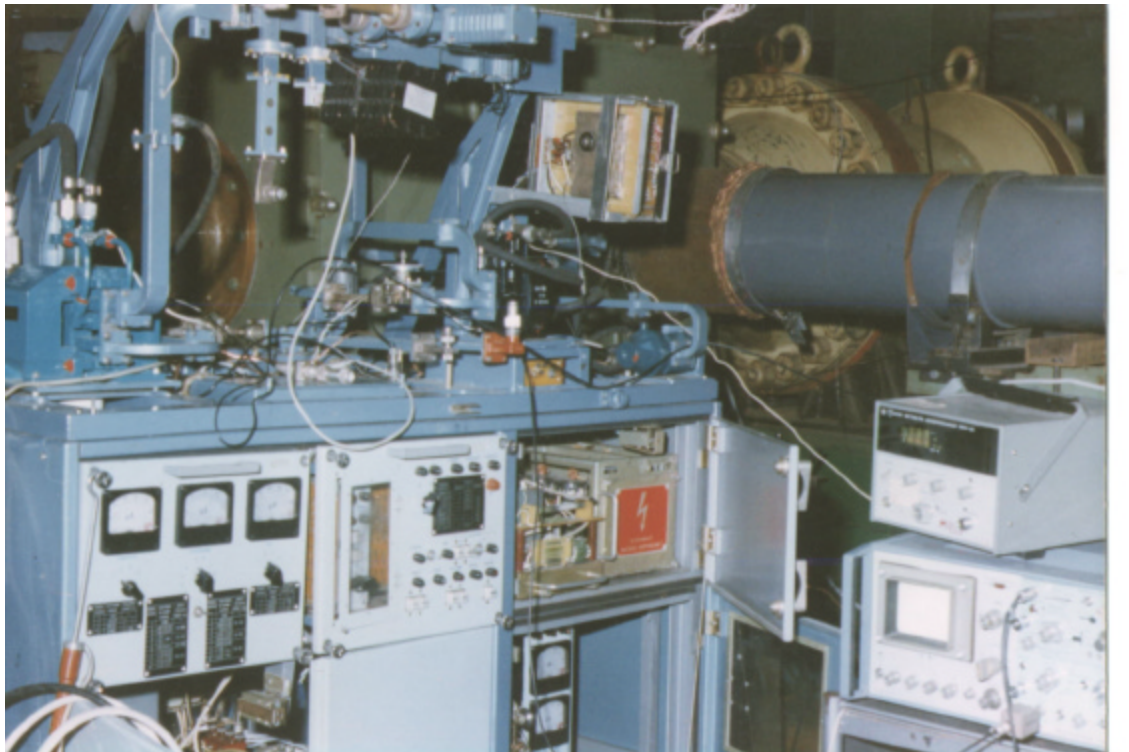
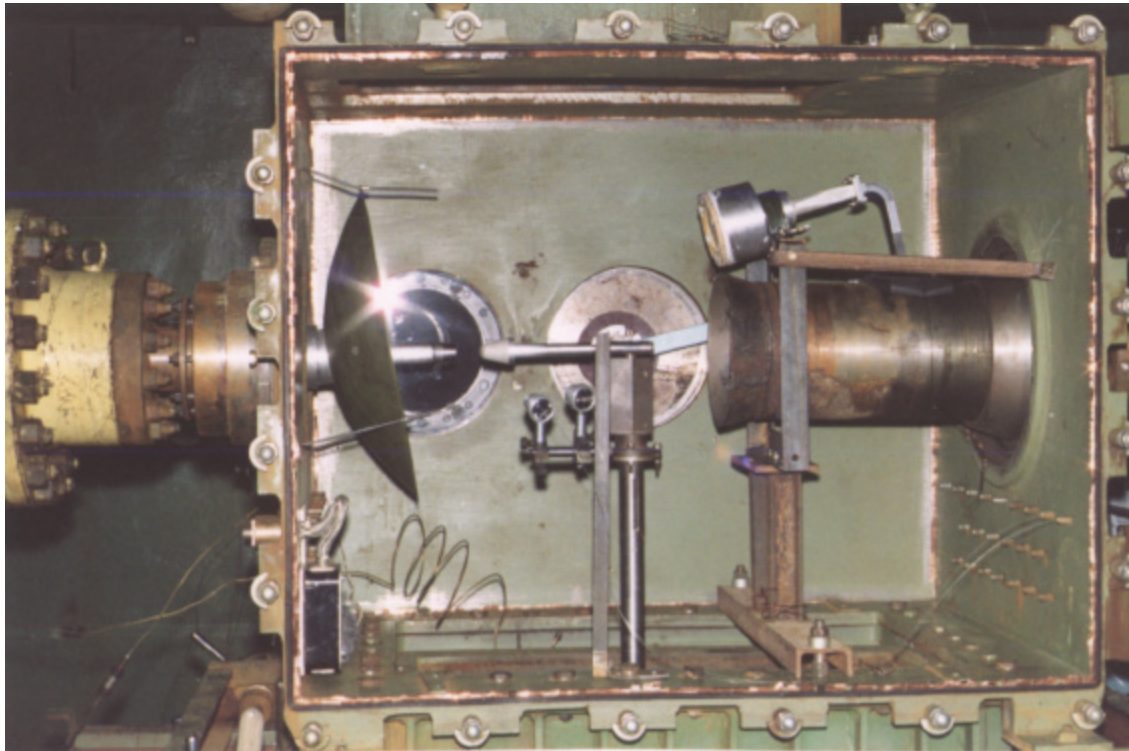


Fig.1.2. Photos of gas-dynamic chamber inside view and MW generator



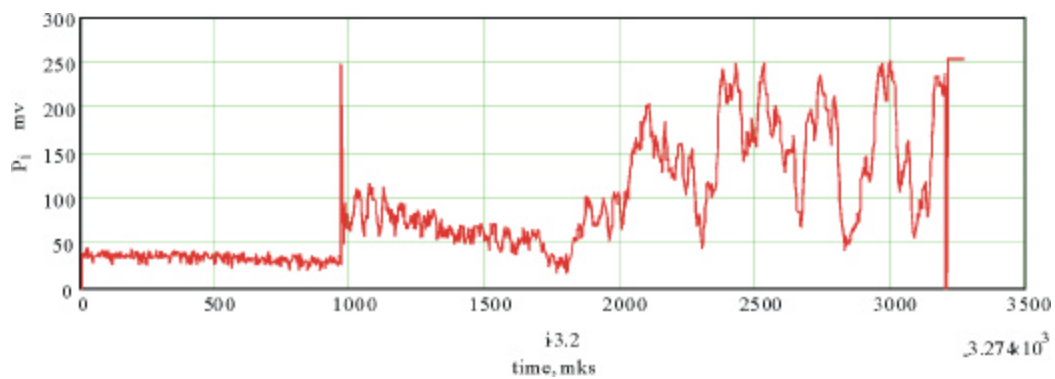


Fig. 2.1. Transient characteristic of the piezoelectric sensor and Kulite

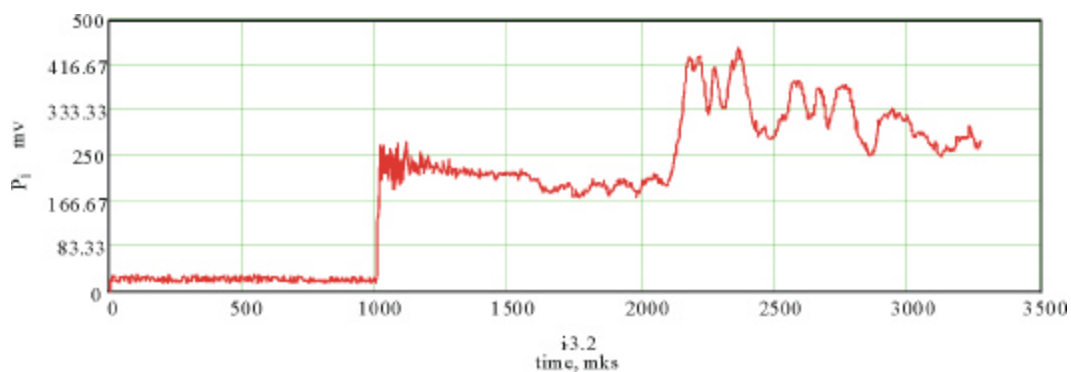
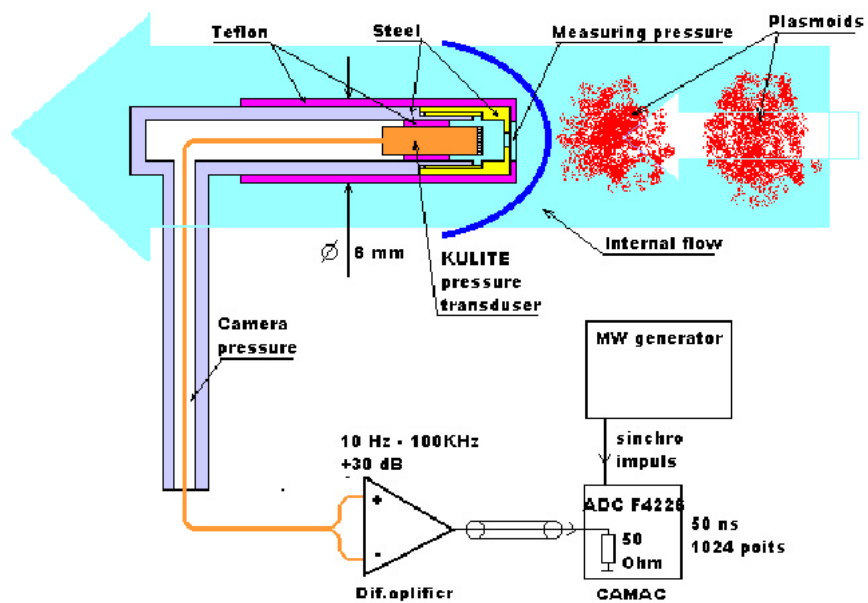


Fig. 2.2. Transient characteristic of the piezoelectric sensor and Kulite



Scheme of Kulite measurements in powerful MW fields

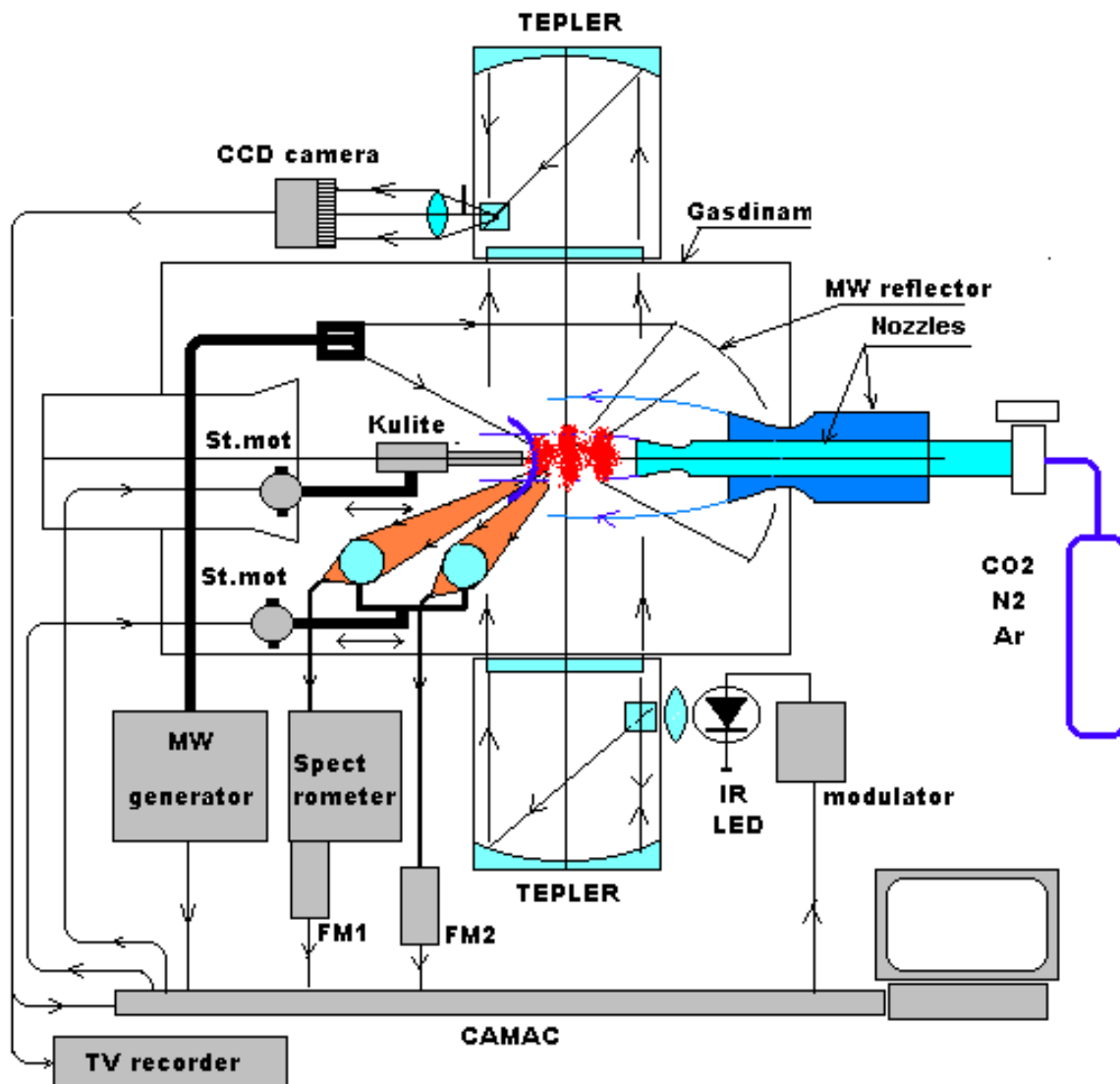


Fig.2.3. Scheme of optic measurements

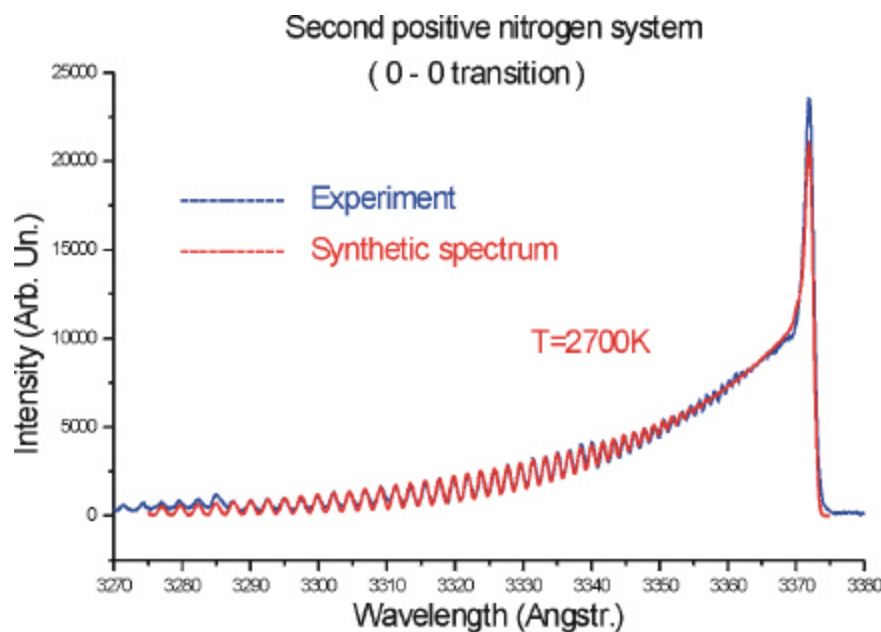


Fig.2.4. Optic spectrum fitting

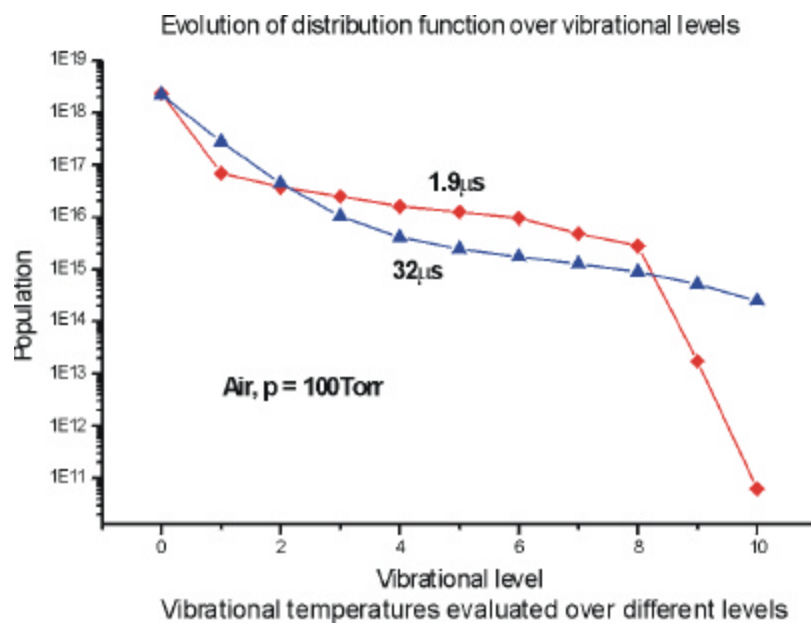
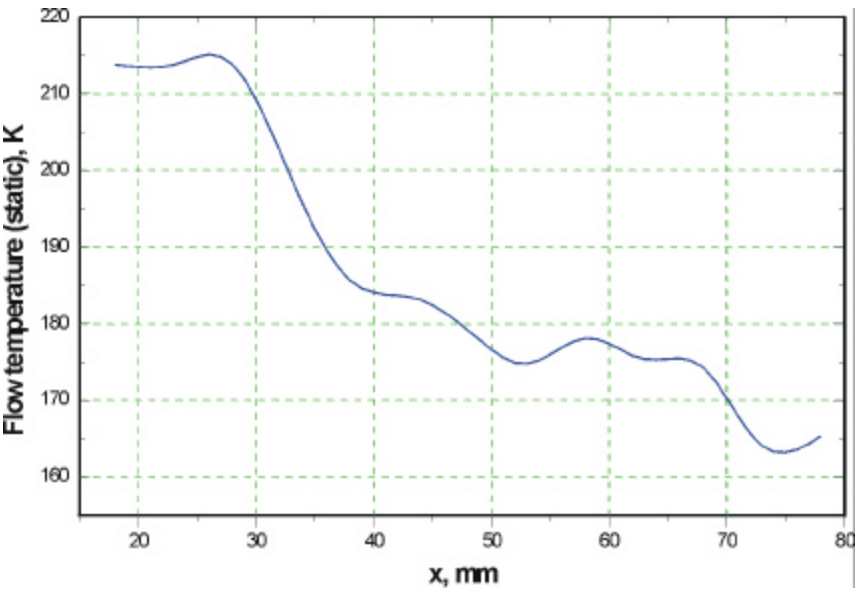
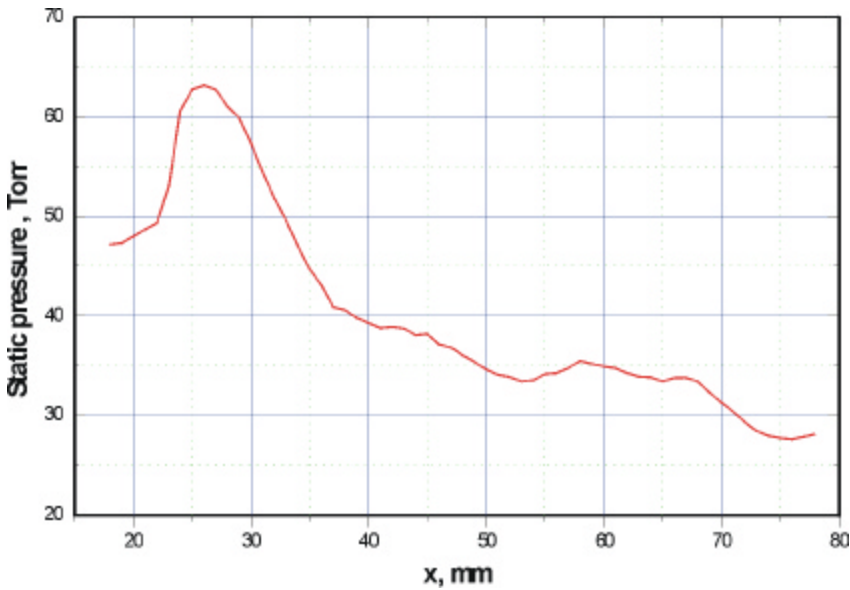
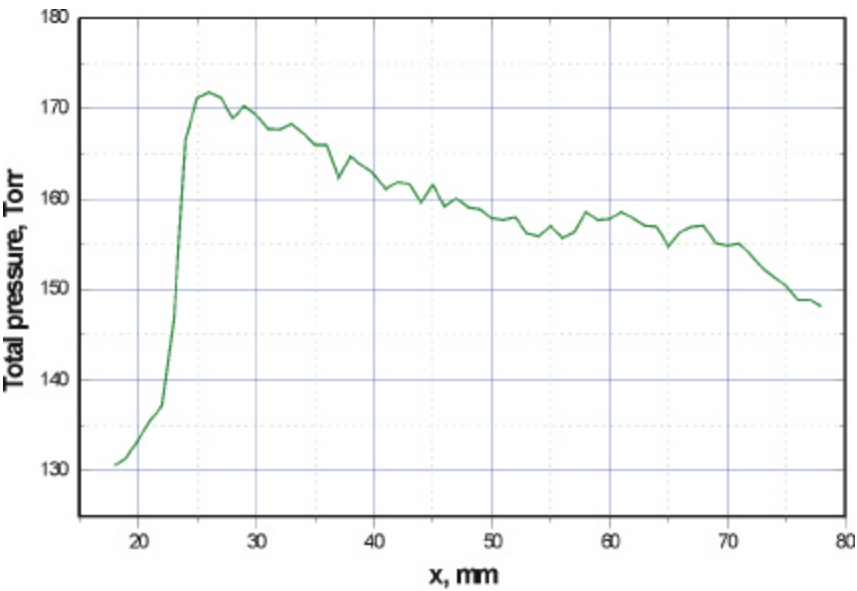


Fig.2.5. Distribution over vibrational levels of nitrogen by the end of MW pulse



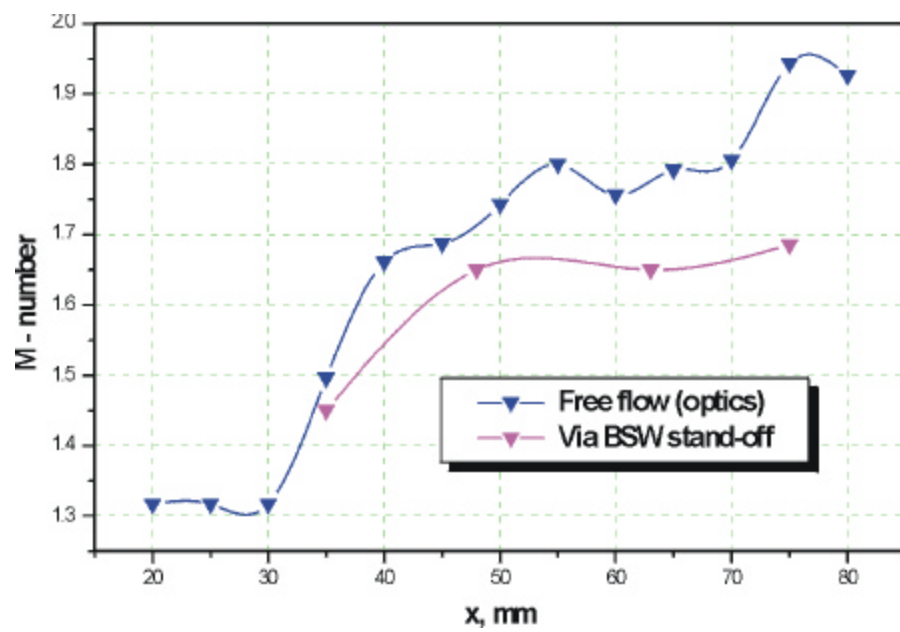
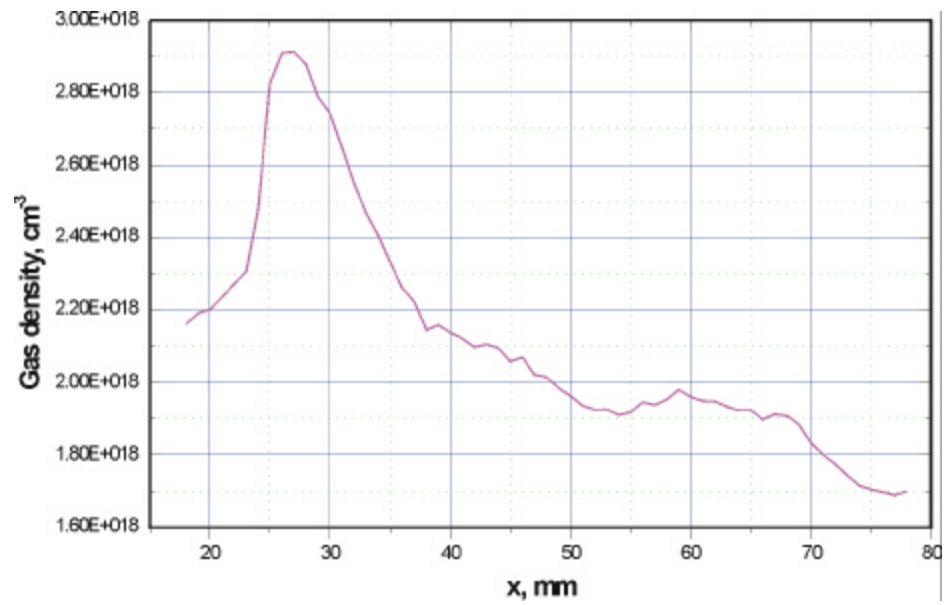


Fig.3.1.-3.2. Free flow parameters

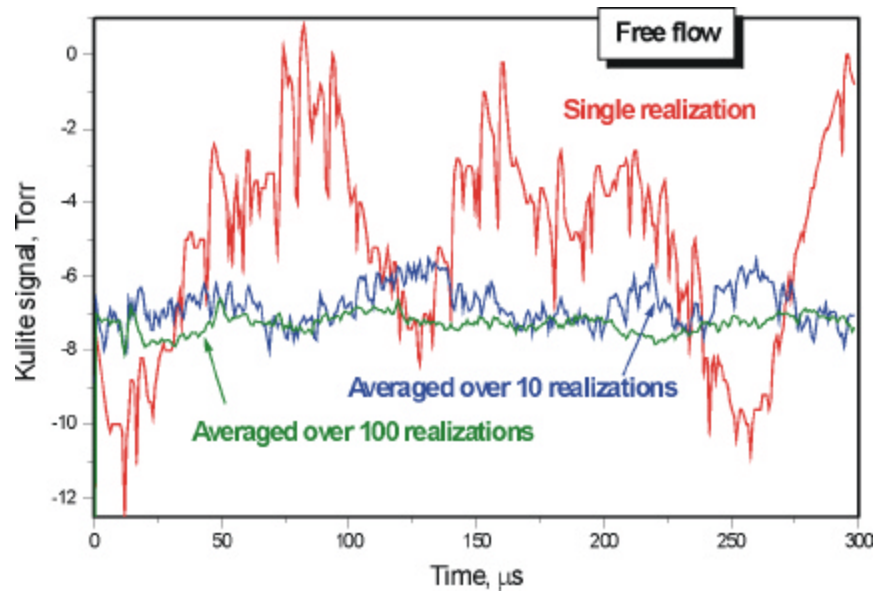


Fig.3.3. Pressure fluctuations of free flow

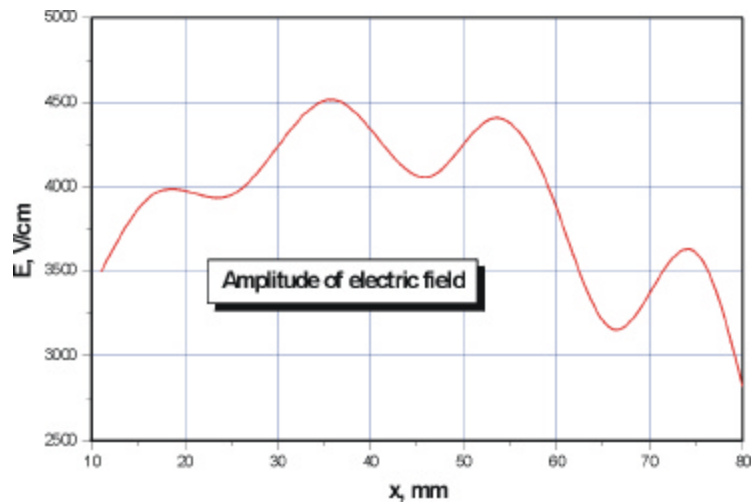


Fig.3.4. Electric field distribution along flow axis

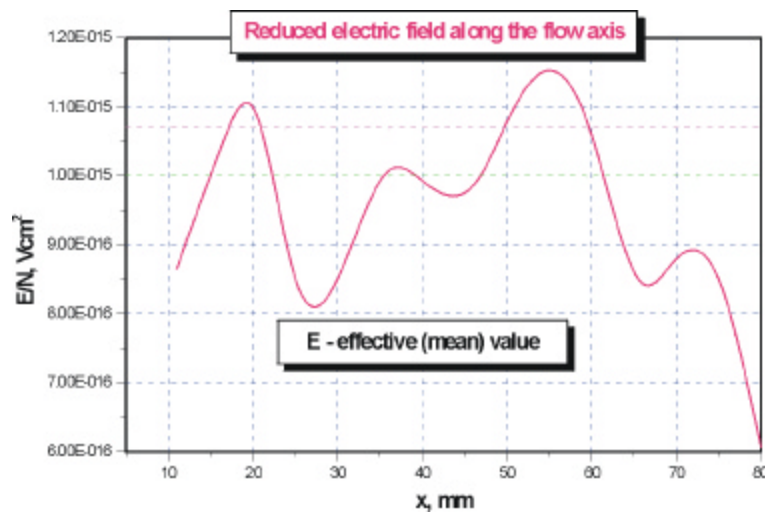


Fig.3.5. Reduced electric field distribution along flow axis

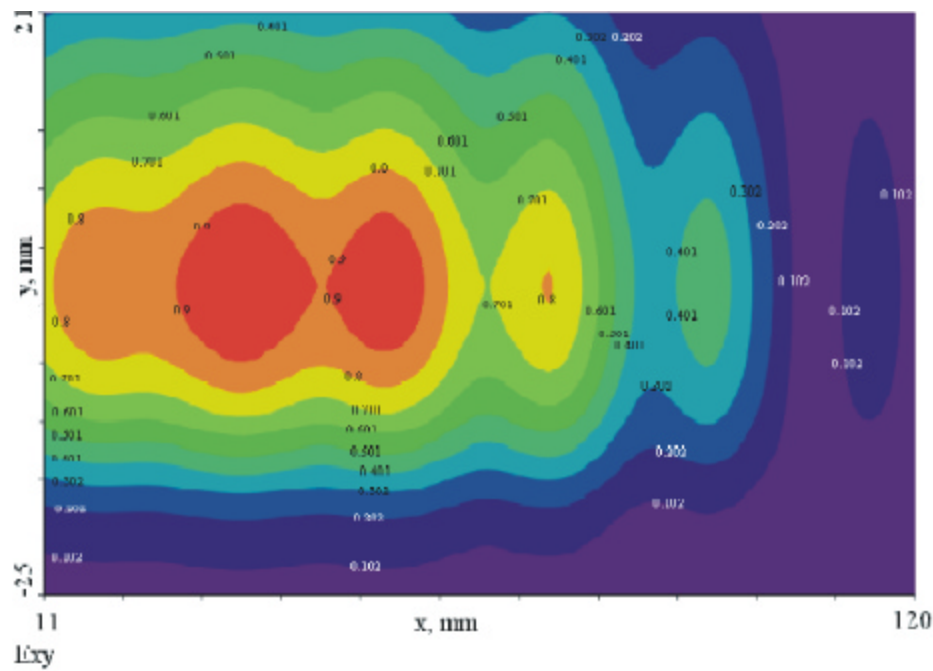


Fig4a. Electric field map in x-y plane

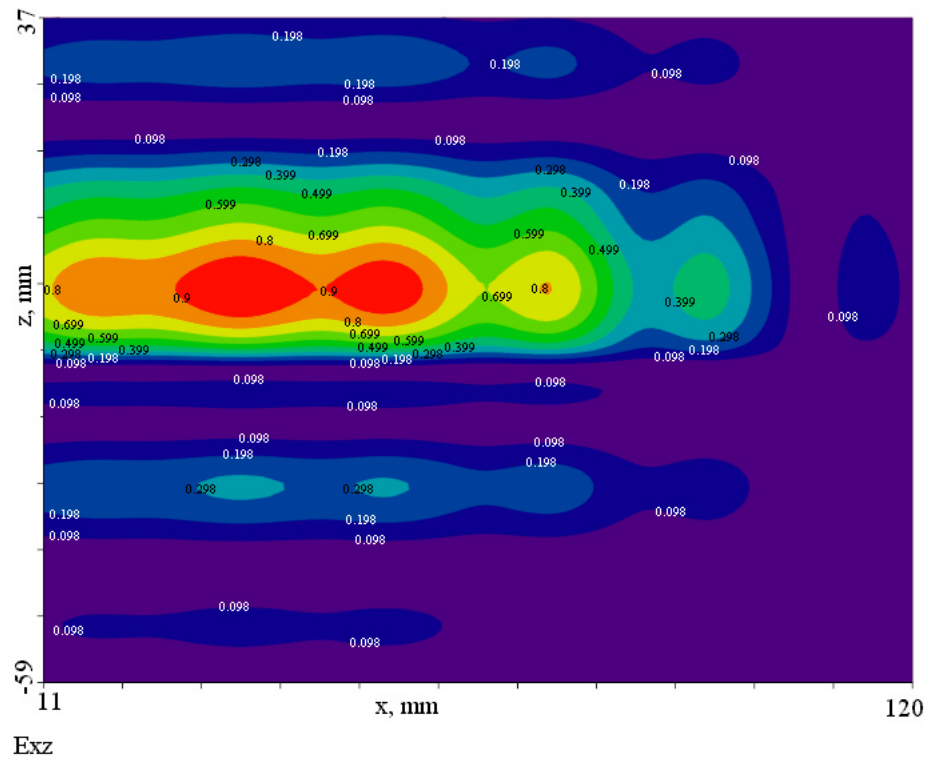


Fig4b. Electric field map in x-z plane

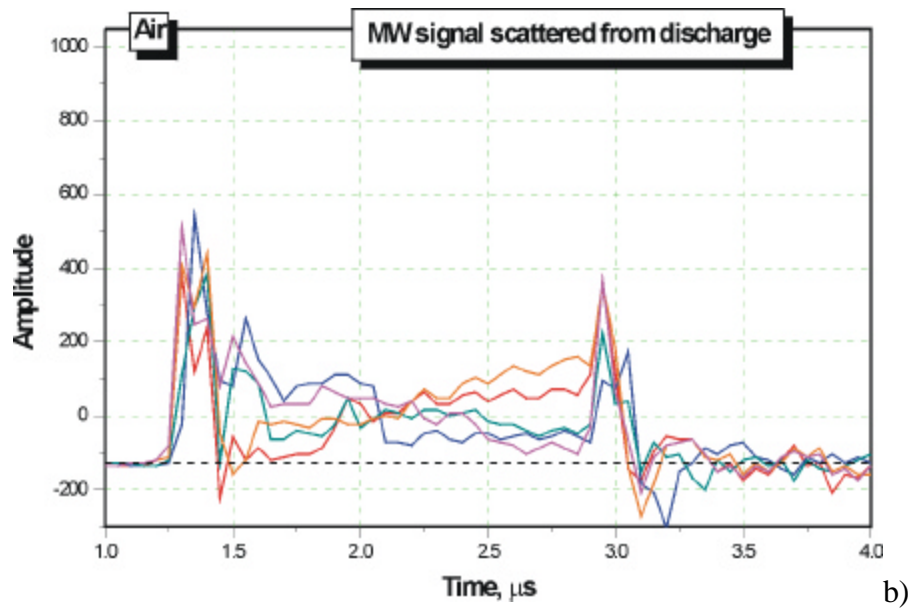
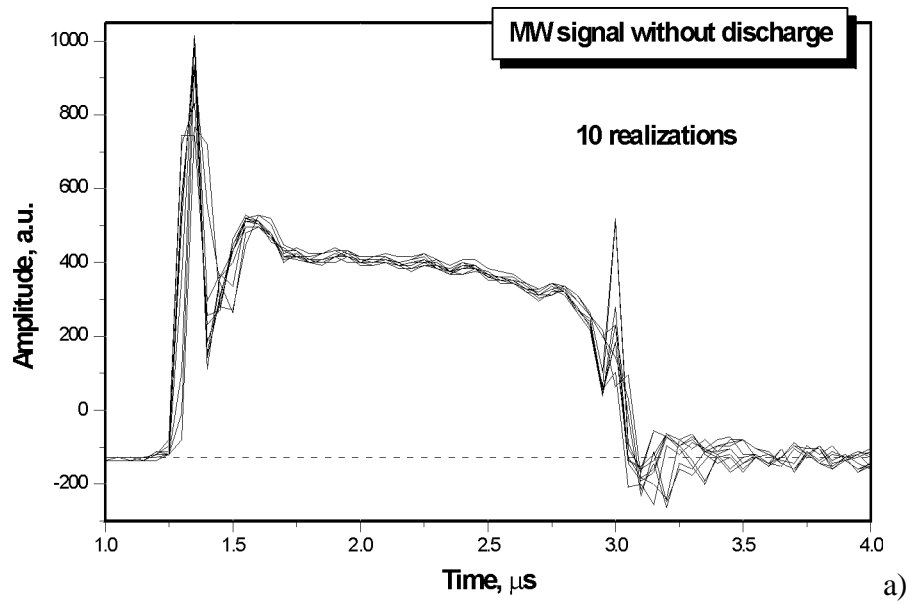


Fig.3.6. MW signal with (b) and without (a) discharge



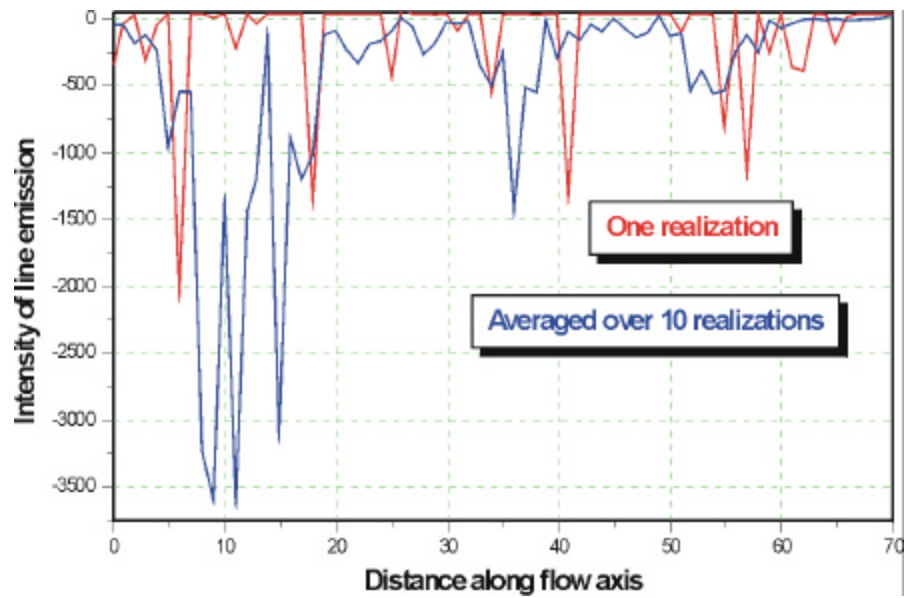


Fig.3.7. Discharge light emission distribution along flow axis

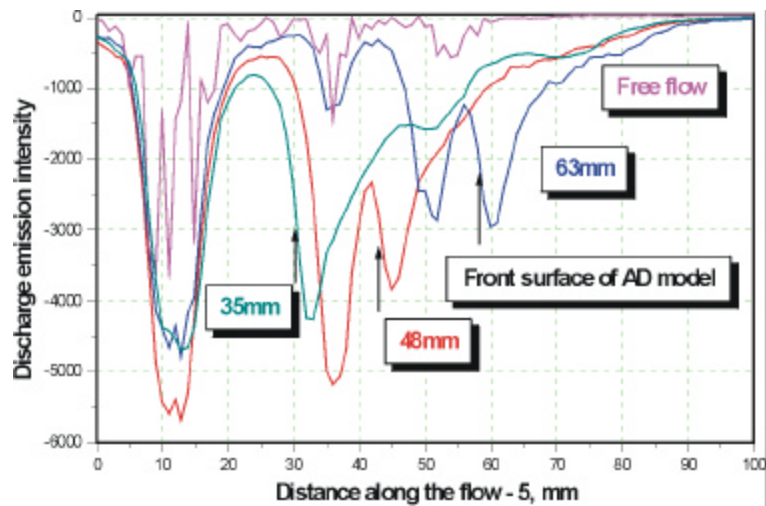


Fig.3.8. Discharge light emission distribution along flow axis

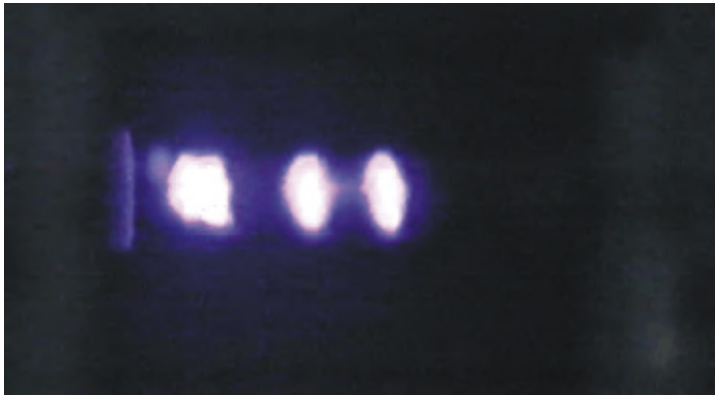
*Free flow**48mm position**63mm position**75mm position*

Fig.3.9. Photos of MW discharge in air

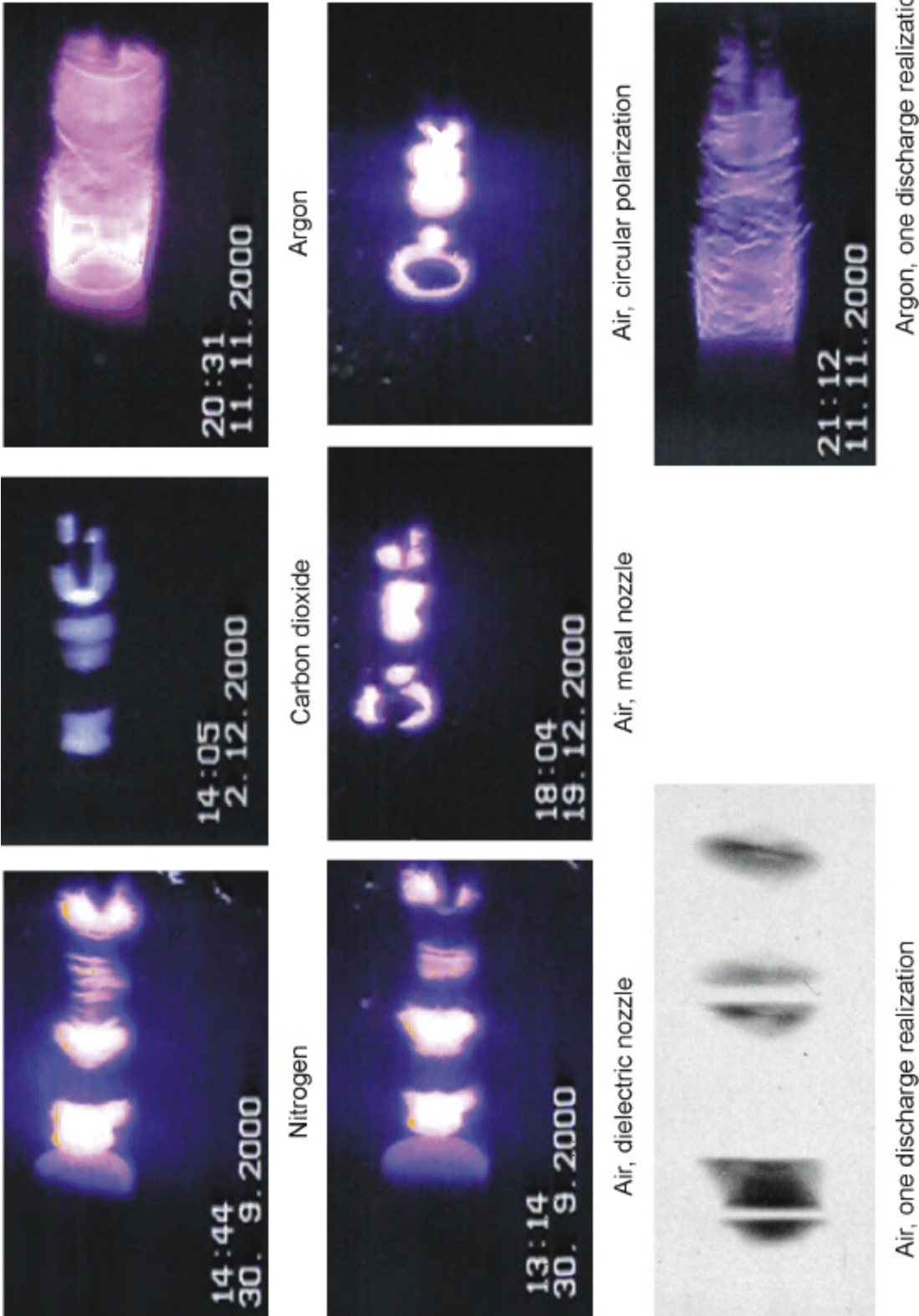
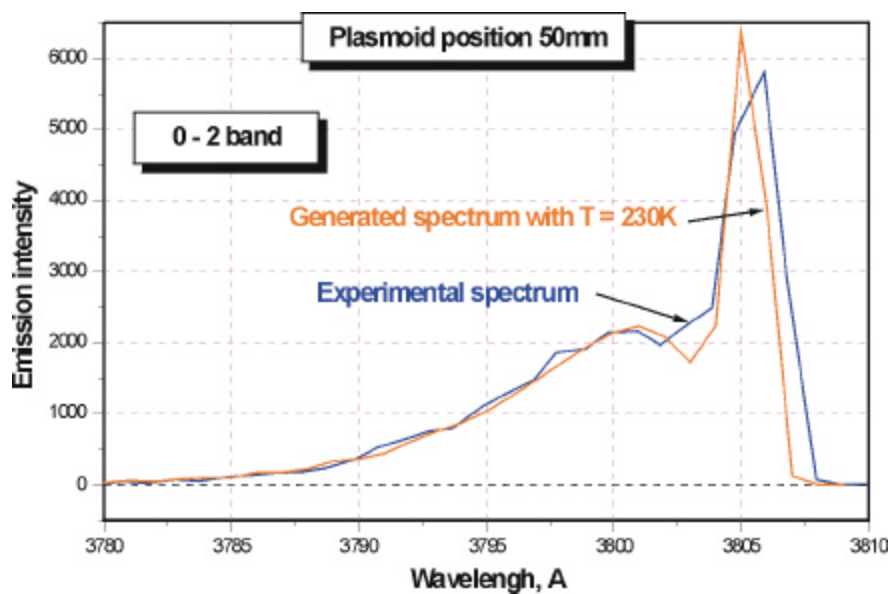
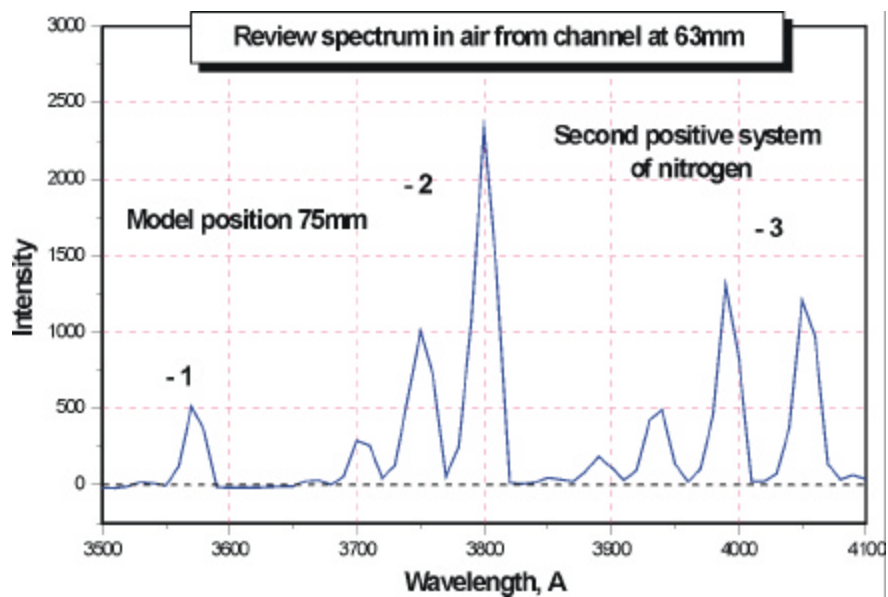


Fig.3.10. Discharge photos



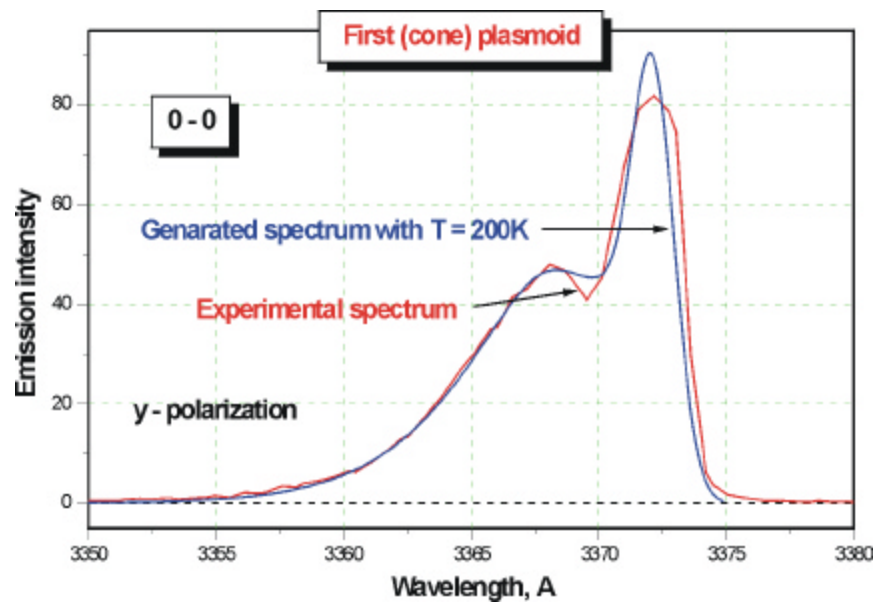
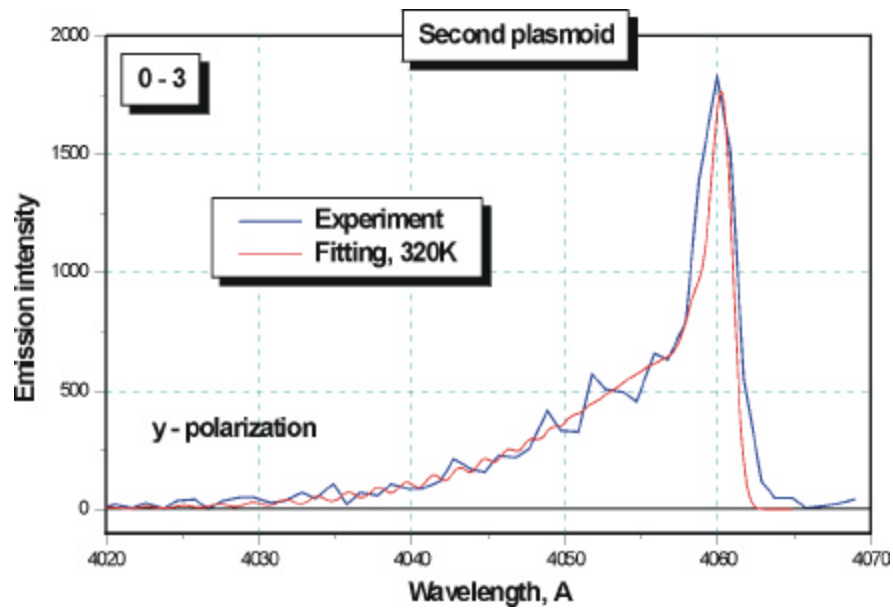


Fig.3.11a-d. Review and band spectra from different plamoids

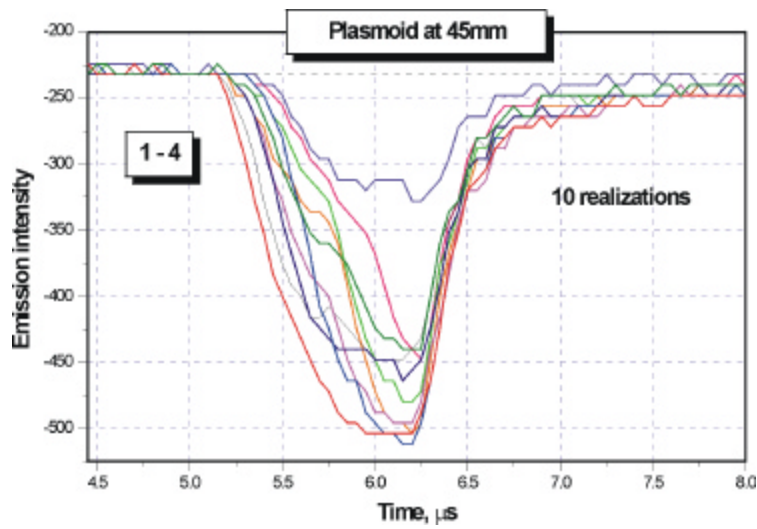
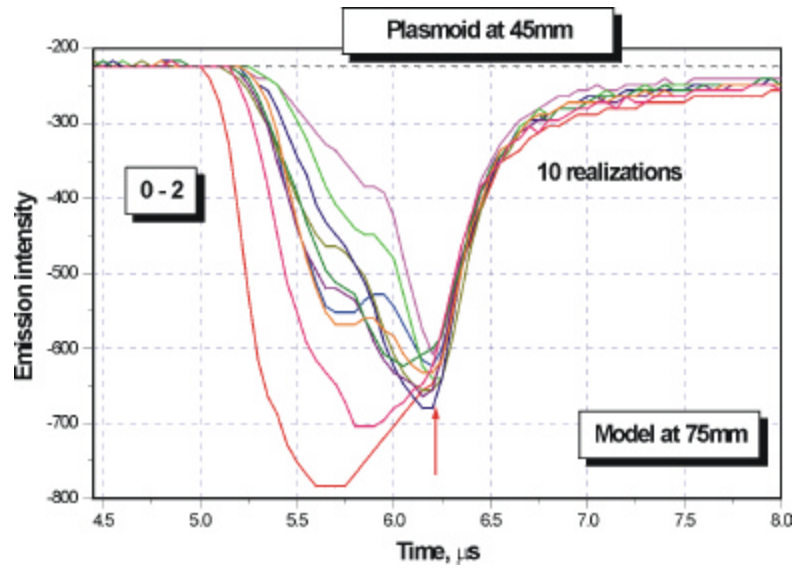


Fig.3.12, Fig.3.13. Time evolution of light emission from plasmoids



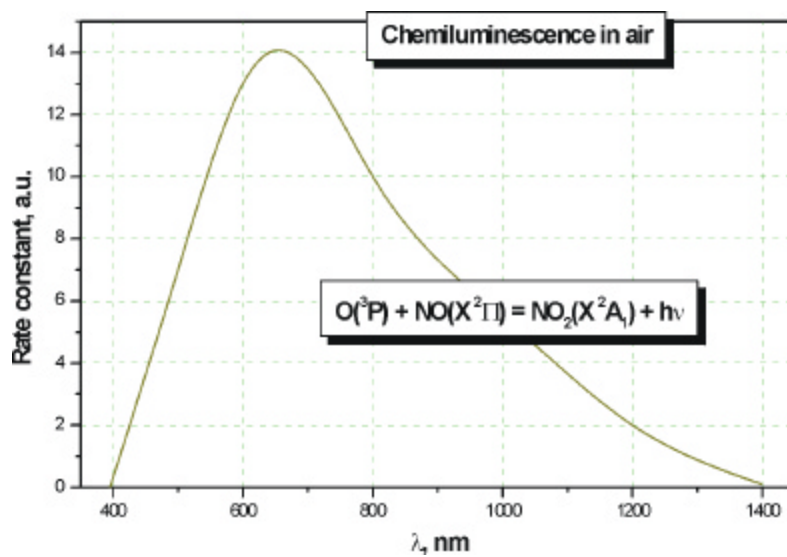


Fig.3.14. Spectrum of chemiluminescence

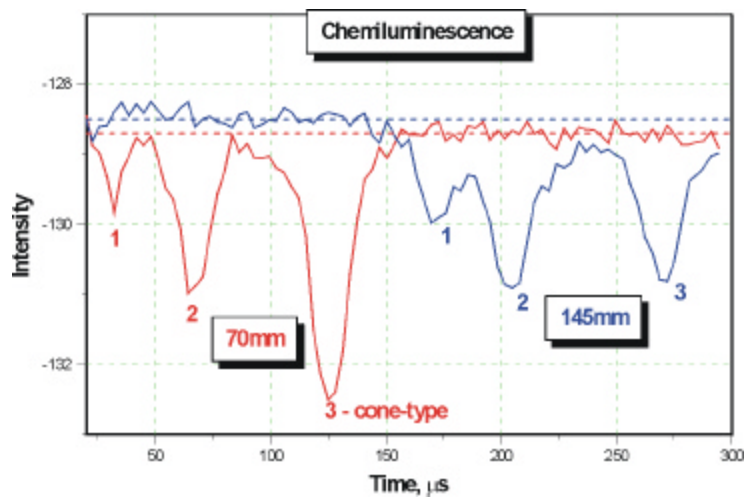


Fig.3.15. Evolution of weak luminescence at different spatial points

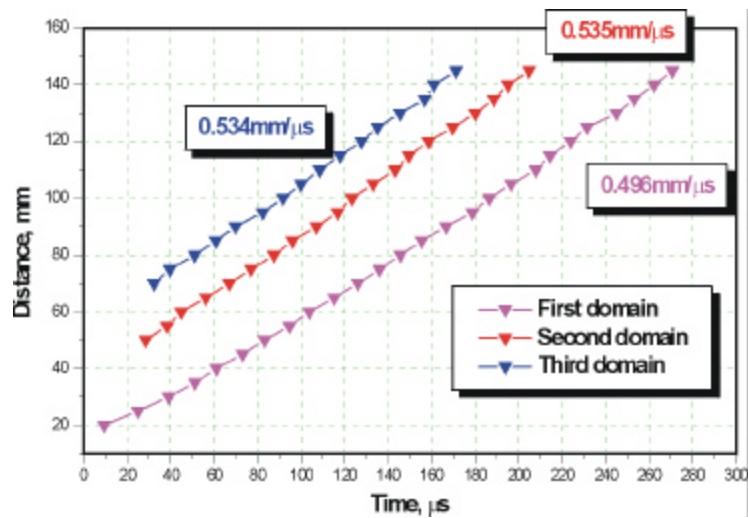


Fig.3.16. x-t diagrams of discharge domains

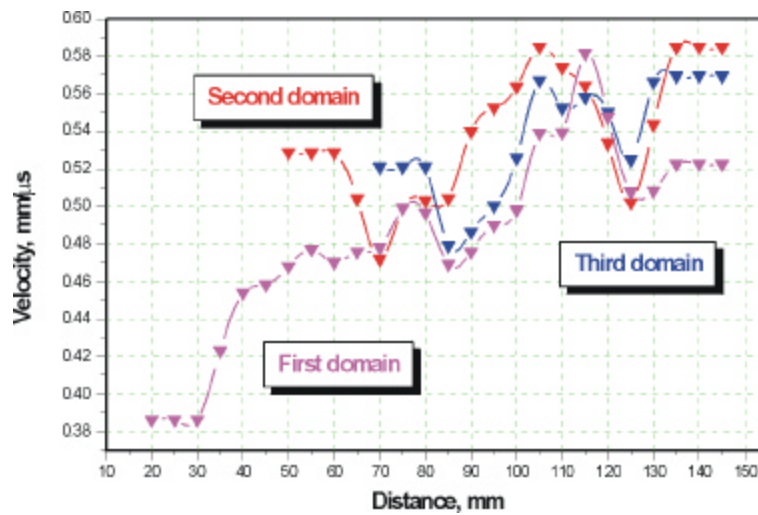
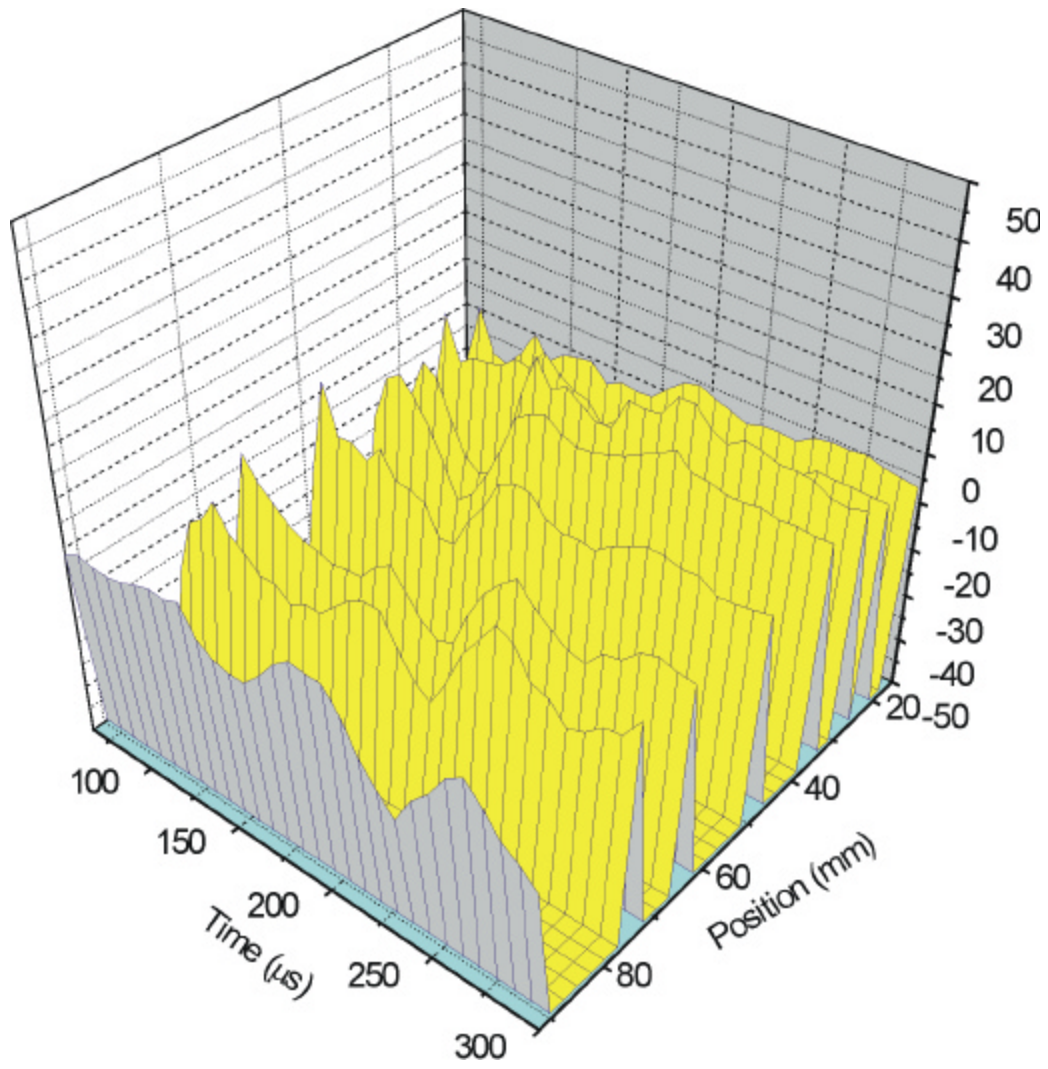


Fig.3.17. Drift velocities of discharge domains





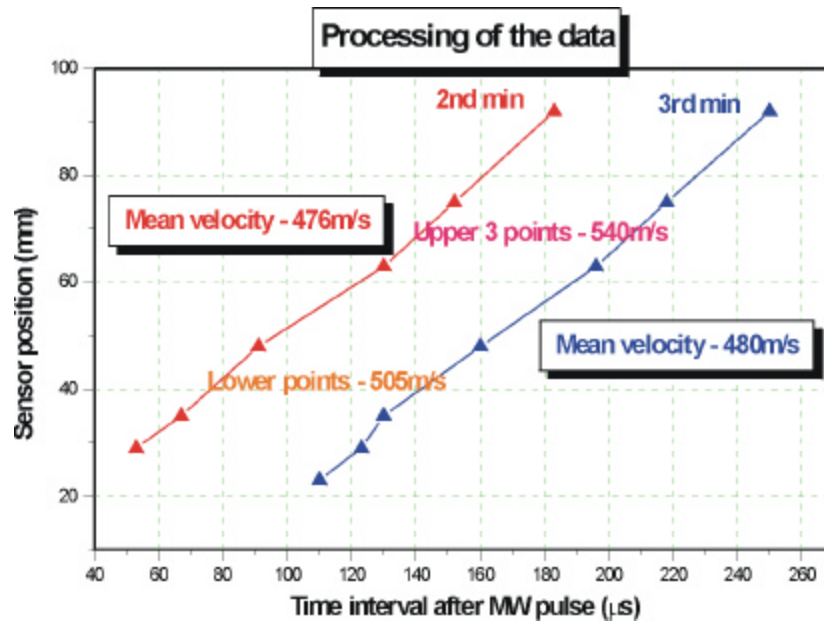


Fig.3.18a,b

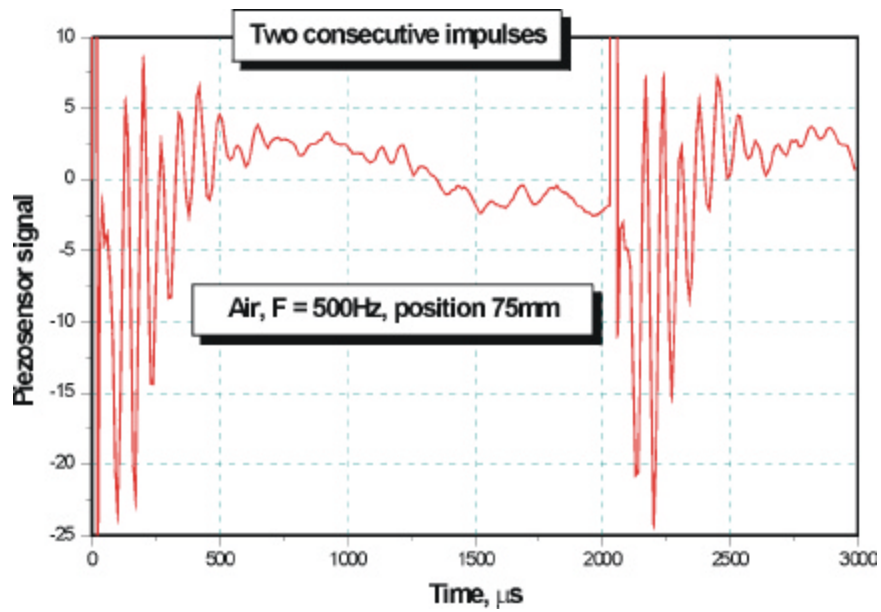


Fig.3.19. Stagnation pressure evolution in two consequent impulses

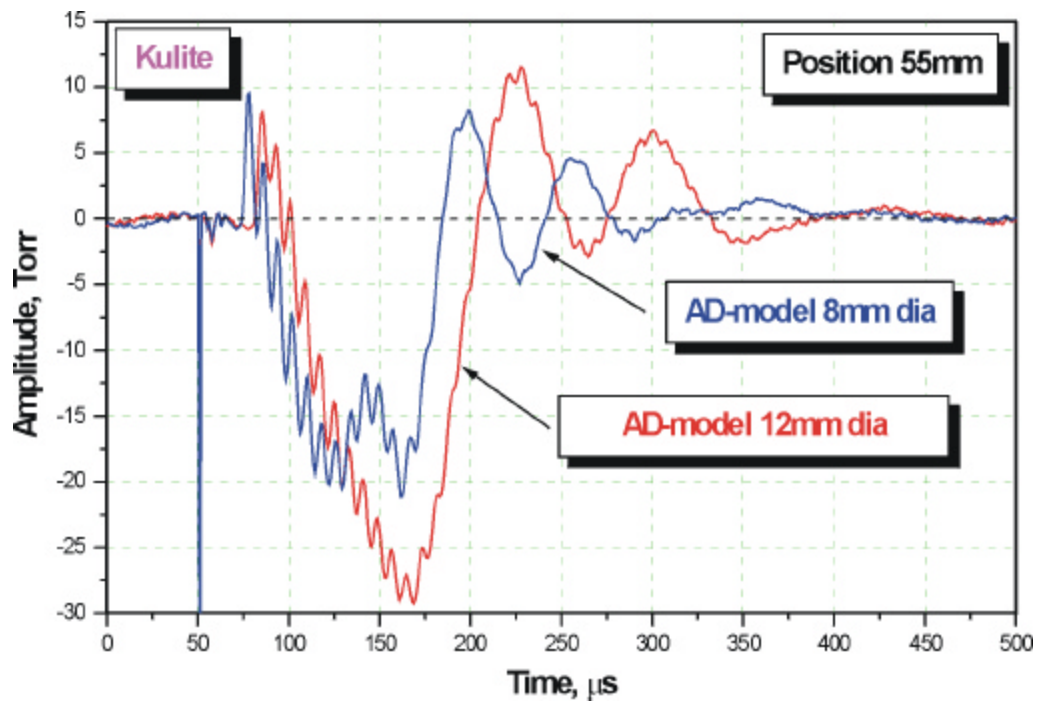


Fig.3.20. Evolution of stagnation pressure in air (Kulite sensor)

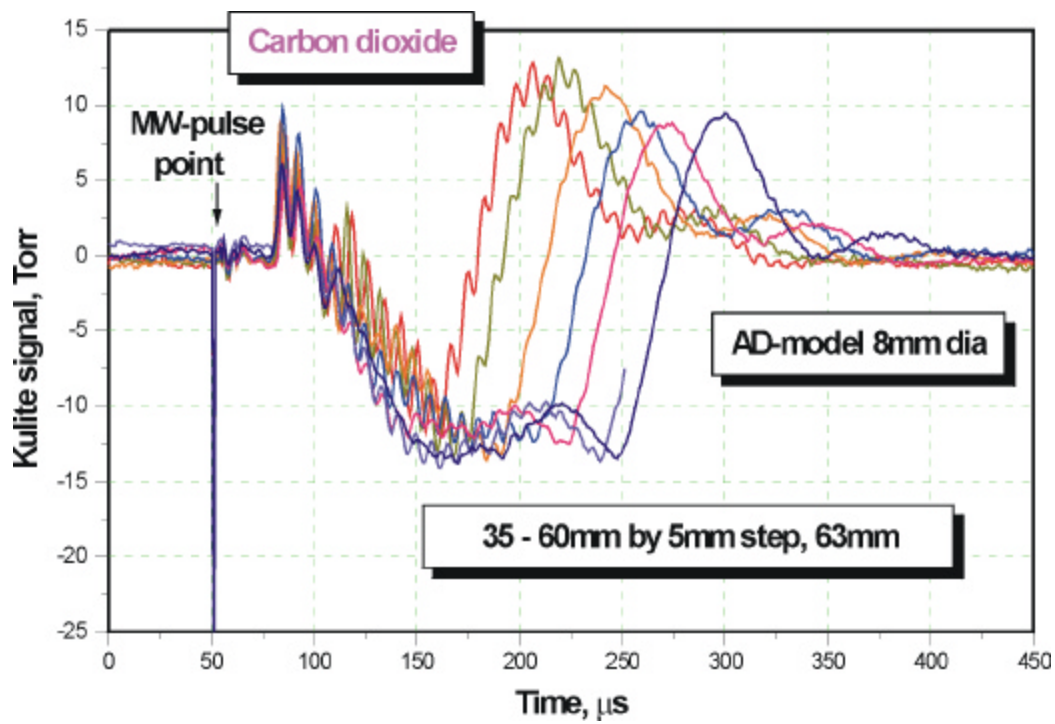


Fig.3.21. Evolution of stagnation pressure in CO<sub>2</sub> (Kulite sensor)

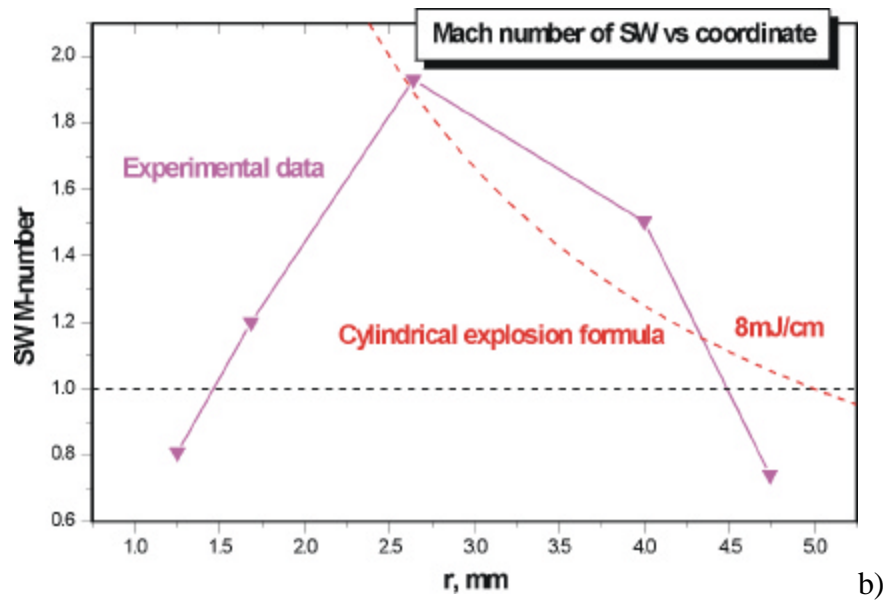
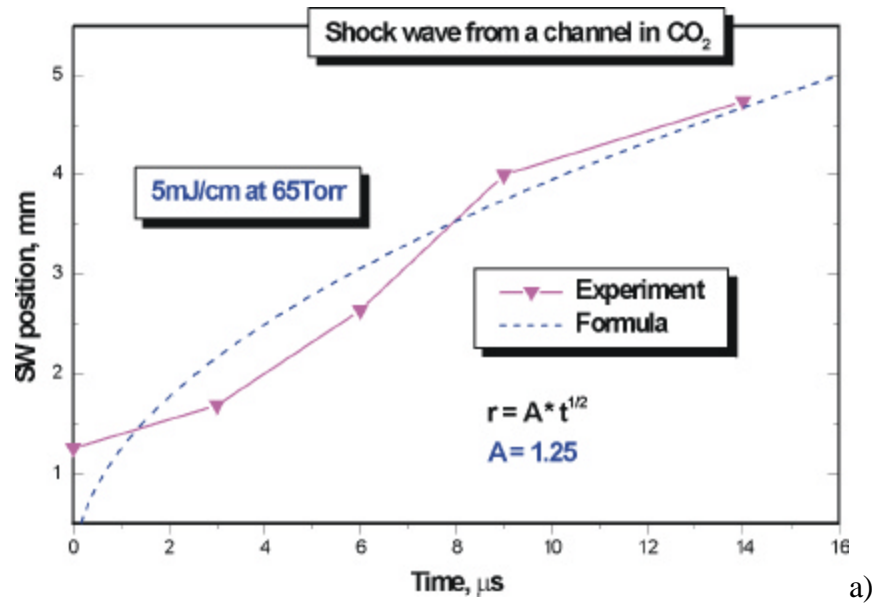


Fig.3.22a,b x-t (a) and v-x (b) diagrams of SW front from discharge channel

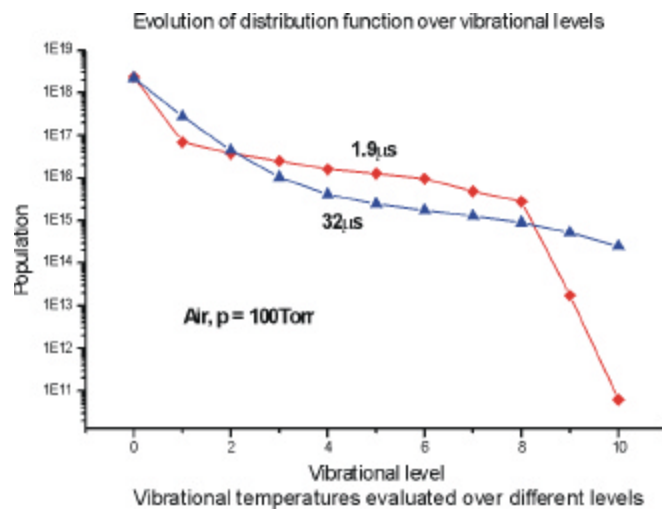


Fig.4.1. VDF of nitrogen

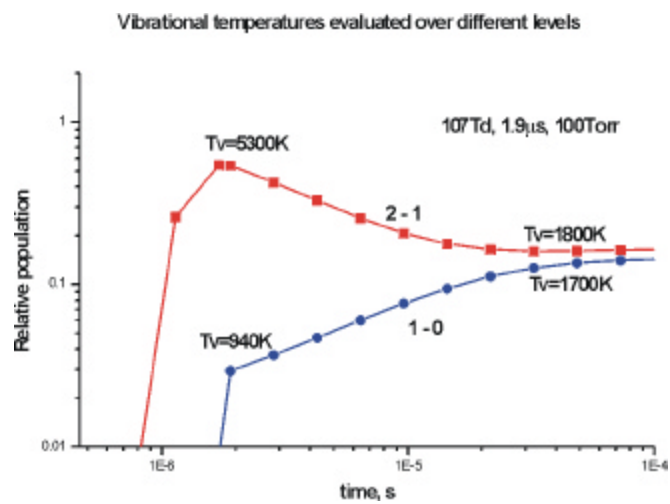


Fig.4.2. Vibrational “temperatures” by the end of MW pulse

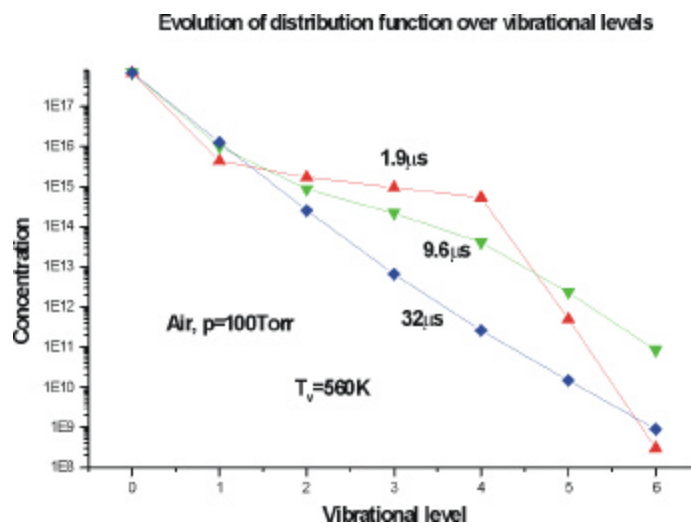


Fig.4.3. VDF of oxygen

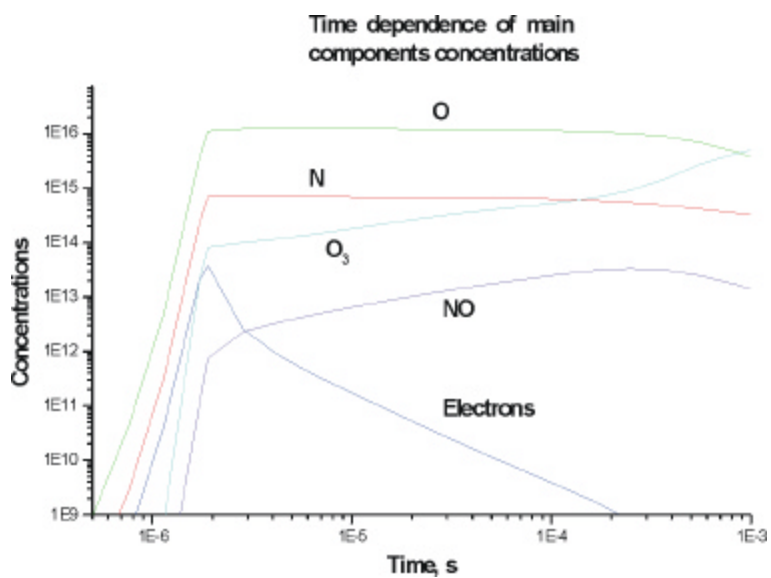


Fig.4.4. Kinetics of the main components in discharge during MW pulse and pause

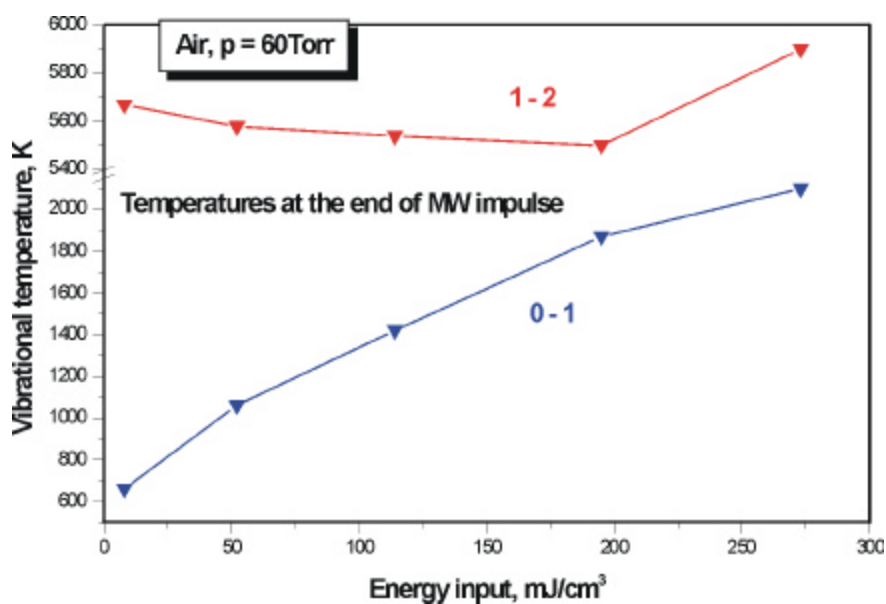


Fig.4.5. a Dependence of vibrational “temperatures” over energy input in nitrogen

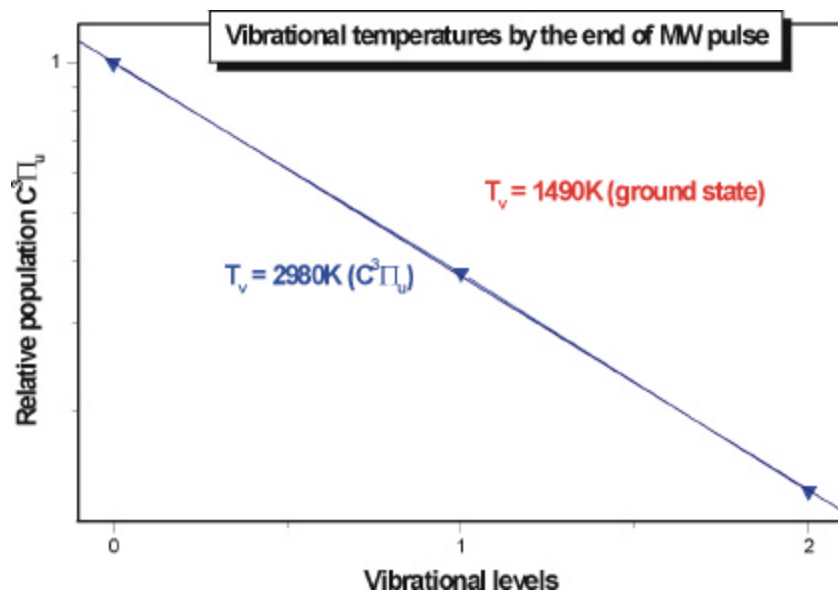


Fig.4.5b. b) Determination of vibrational “temperature” of nitrogen by the end of MW pulse (tv-e.doc)

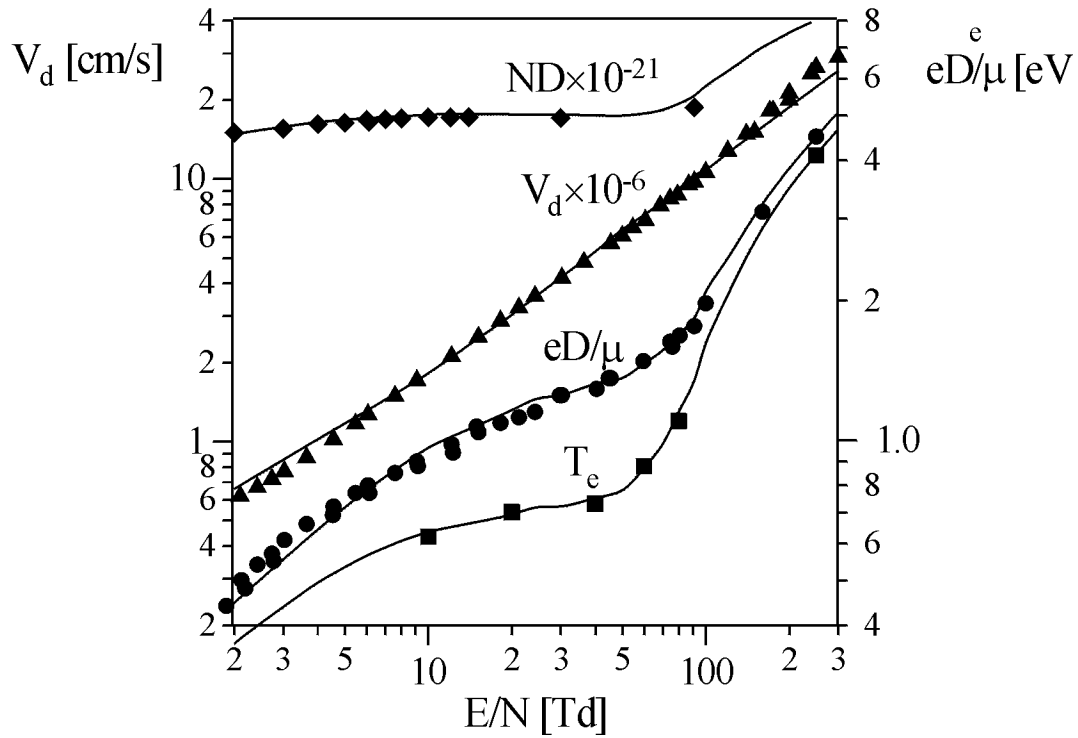


Fig.4.6. Dependencies of diffusion coefficient  $ND$ , drift velocity  $V_d$ , "characteristic temperature"  $eD/\mu$  and main temperature  $T_e$  of electrons vs. reduced electric field in discharge  $E/N$ . Symbols-experimental data, solid curves-calculation

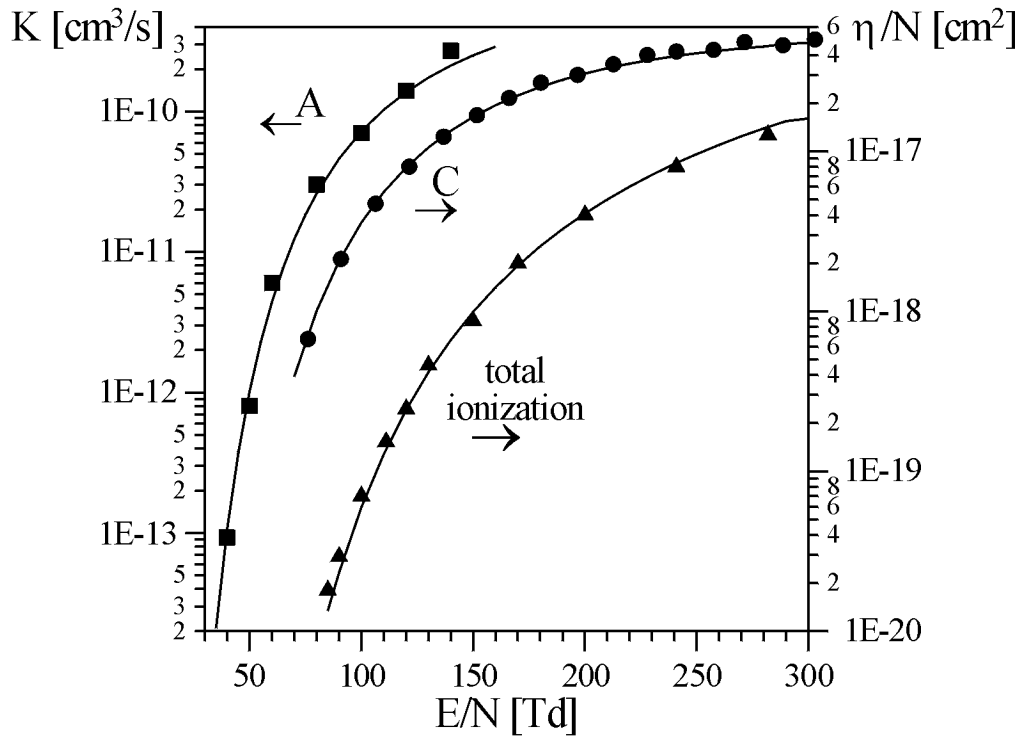


Fig.4.7. Dependencies of rate constants and Townsend coefficients vs. reduced electric field. A-  $A^3\Sigma_u^+$  state excitation, C-  $C^3\Pi_u$  state excitation. Symbols-experimental data, solid curves-calculation



Table 1. Coefficients of approximation for electron states excitation in vibrationally non-excited  $N_2$

state	$B \cdot 10^7$	$n$	$(E/N)_0$
$A^3\Sigma_u^+$	9.52	0.988	494
$B^3\Pi_g$	179	1.467	489
$C^3\Pi_u$	110	1.261	602
$a'^1\Sigma_u^-$	1.05	0.844	493
$w^1\Delta_u$	7.75	1.272	523
$w^3\Delta_u$	4.15	0.920	472
$B'^3\Sigma_u^-$	1.16	0.835	492
$a^1\Pi_g$	2.80	0.827	480
$N_2^+$	0.0287	-0.116	797

Table 2. Coefficients of approximation for correction item considering “two-temperature” vibrational excitation  $N_2$

state	$B \cdot 10^8$	$a$	$b$	$U$	maximal error %
$A^3\Sigma_u^+$	12.7	1.189	6881	15920	3.1
$B^3\Pi_g$	9.40	1.088	5736	12950	8.5
$C^3\Pi_u$	26.6	1.430	7732	15570	8.7
$a'^1\Sigma_u^-$	2.89	1.053	5778	14940	3.1
$w^1\Delta_u$	3.29	1.049	6289	15950	4.0
$w^3\Delta_u$	9.98	1.079	6019	14980	2.7
$B'^3\Sigma_u^-$	3.86	1.083	6005	15160	2.7
$a^1\Pi_g$	4.71	0.916	4752	13860	2.7
$N_2^+$	25.3	0.953	5136	20860	7.3

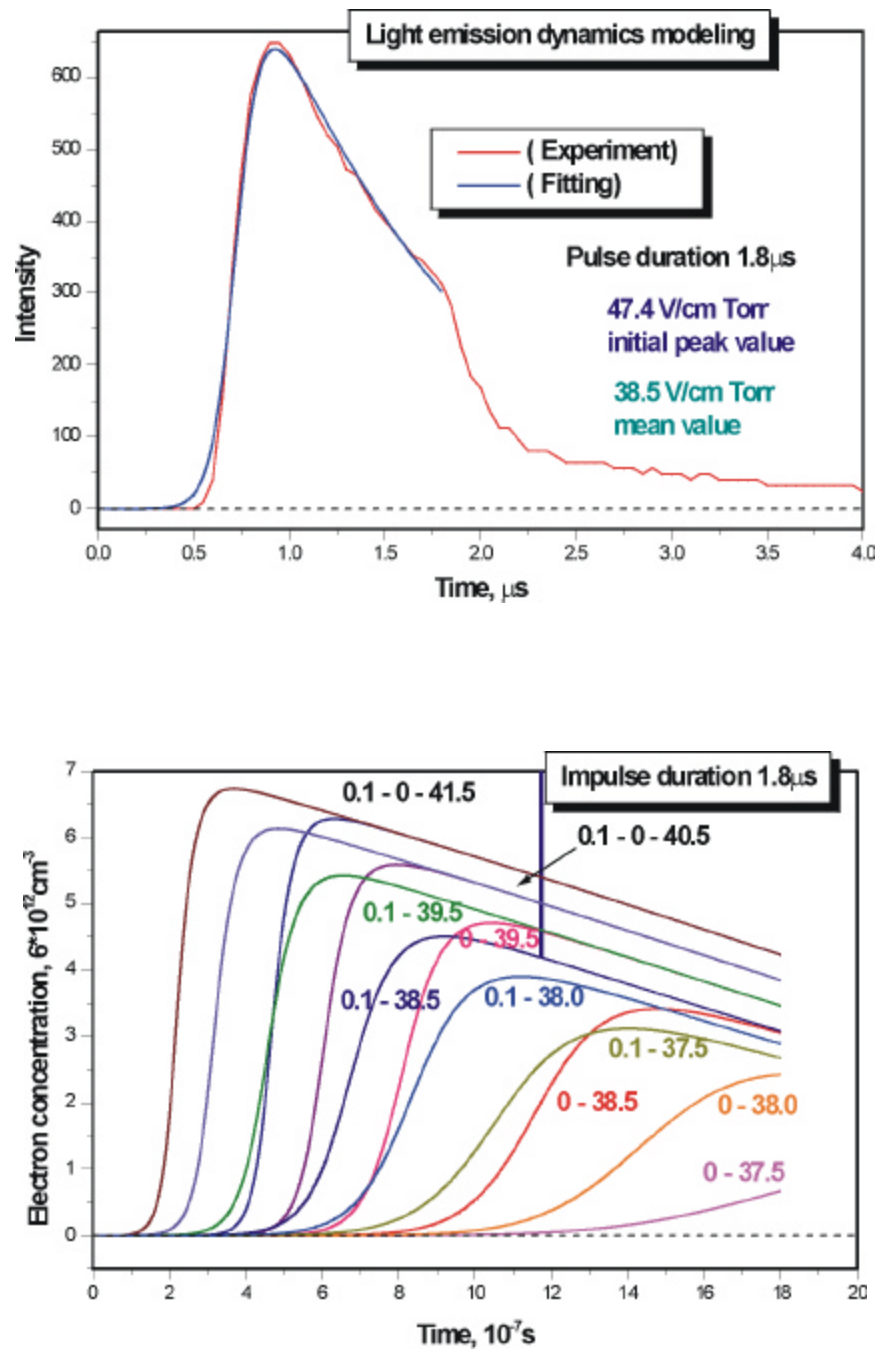


Fig.4.8a,b. Optic signal fitting (a), (b) Influence of MW-signal parameters on the optic emission

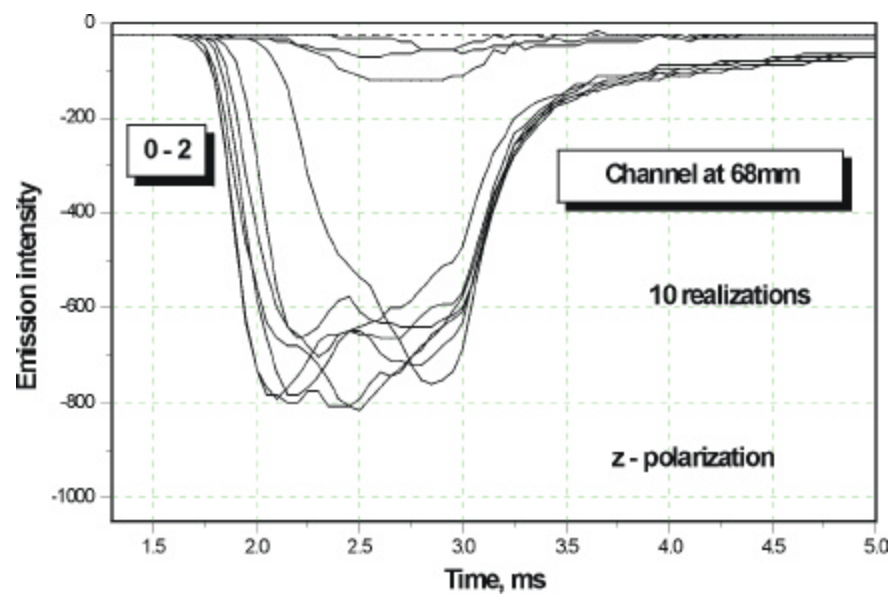
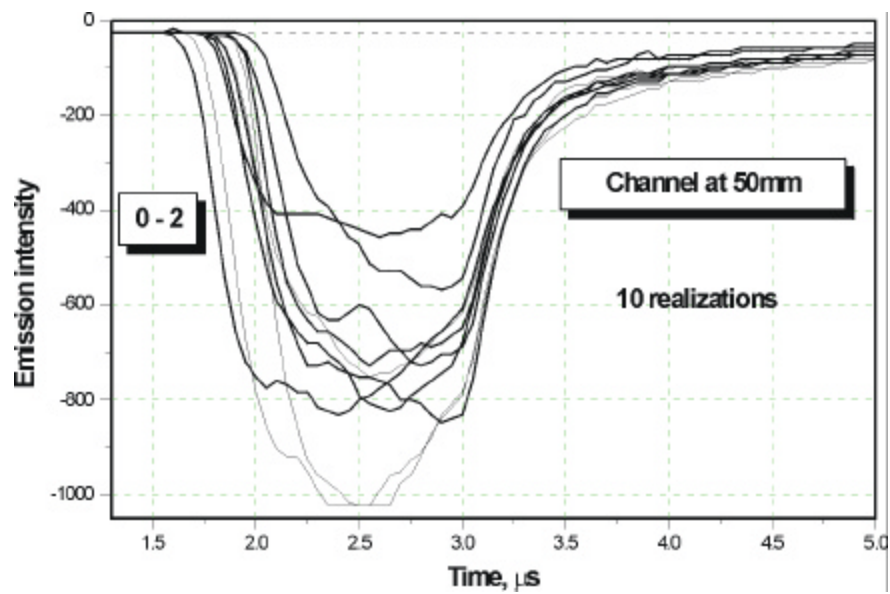
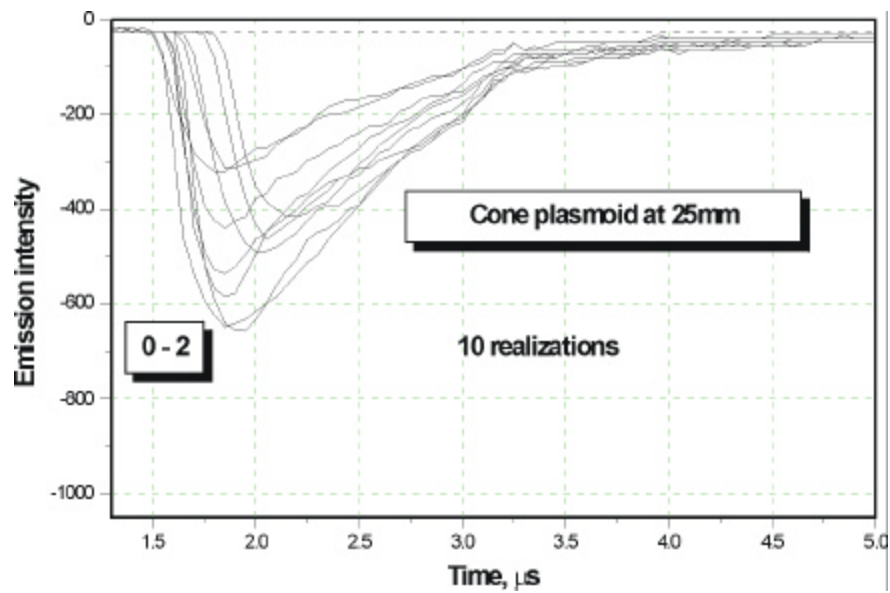


Fig.4.9. Light emission evolution from plasmoids

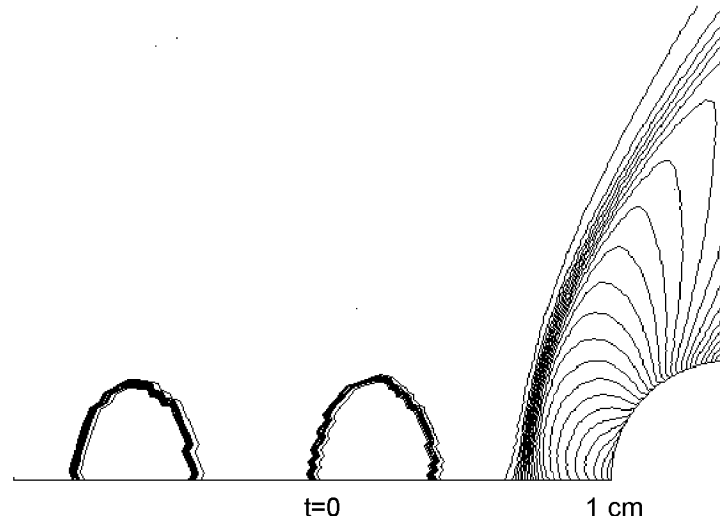
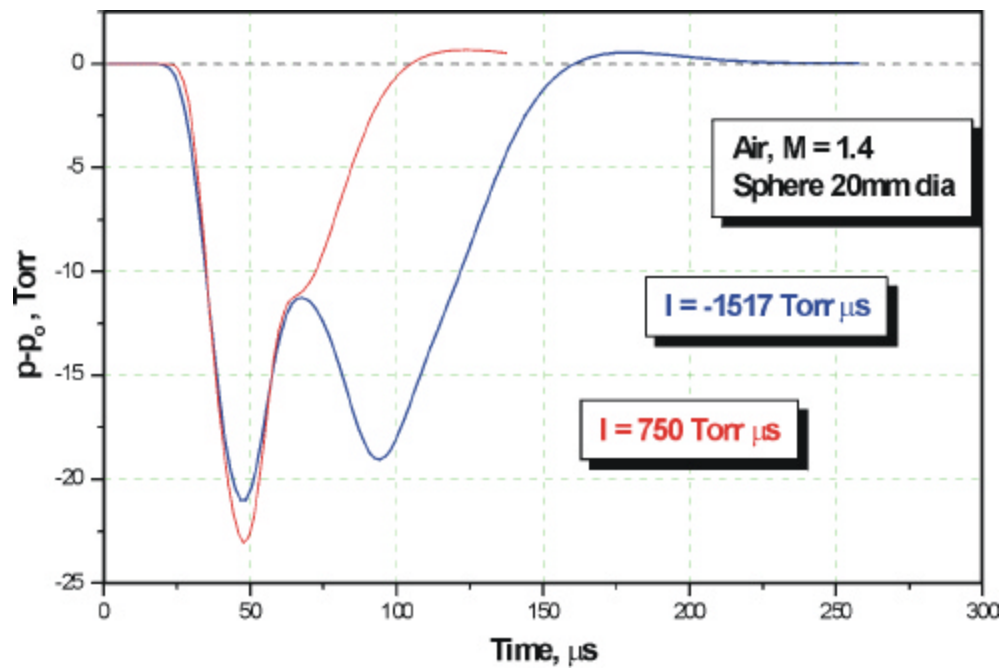
Fig.4.10. Problem formulation at  $t = 0$ 

Fig.4.11. Evolution of stagnation pressure

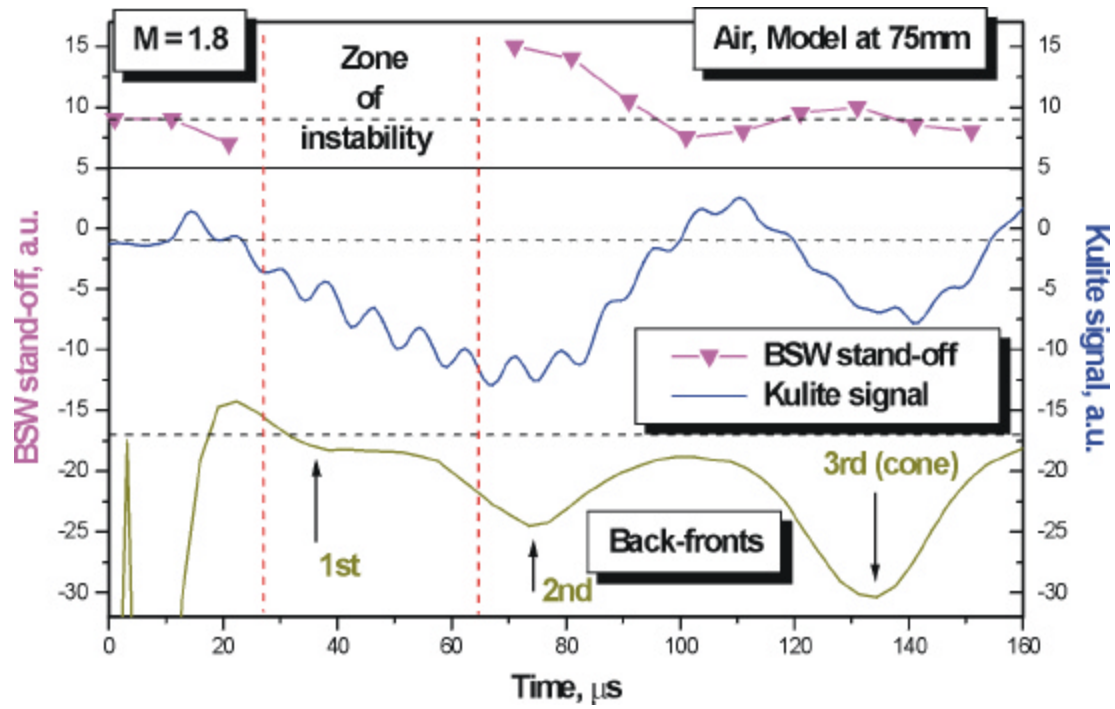


Fig.5.1. Synchronized evolution of gas-dynamic parameters and optics

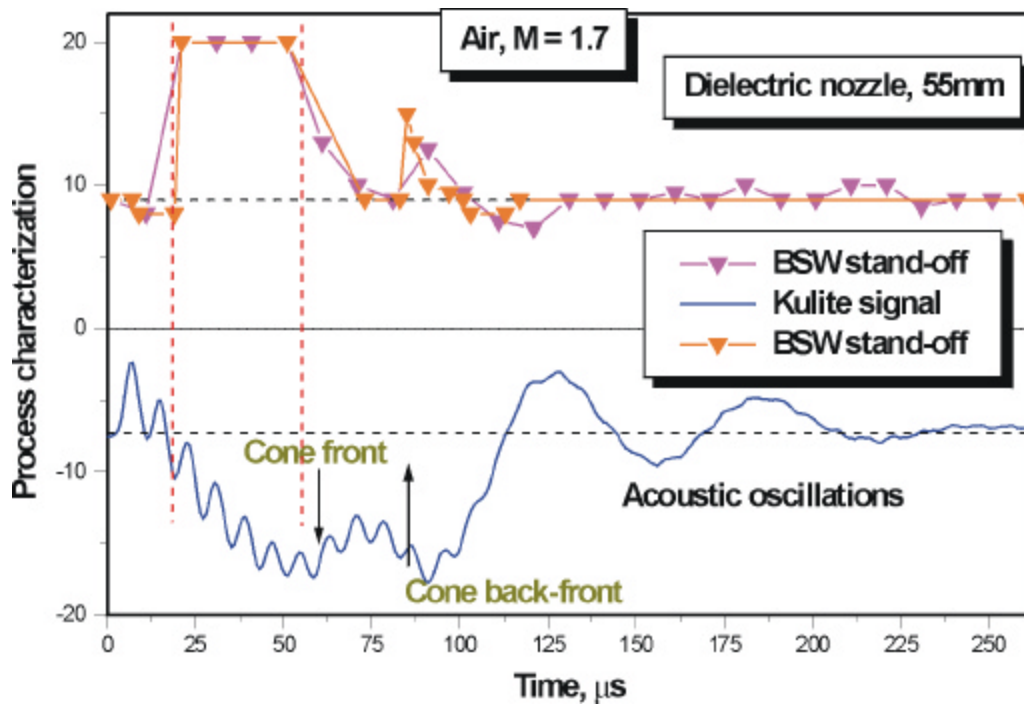


Fig.5.2. Synchronized evolution of gas-dynamic parameters



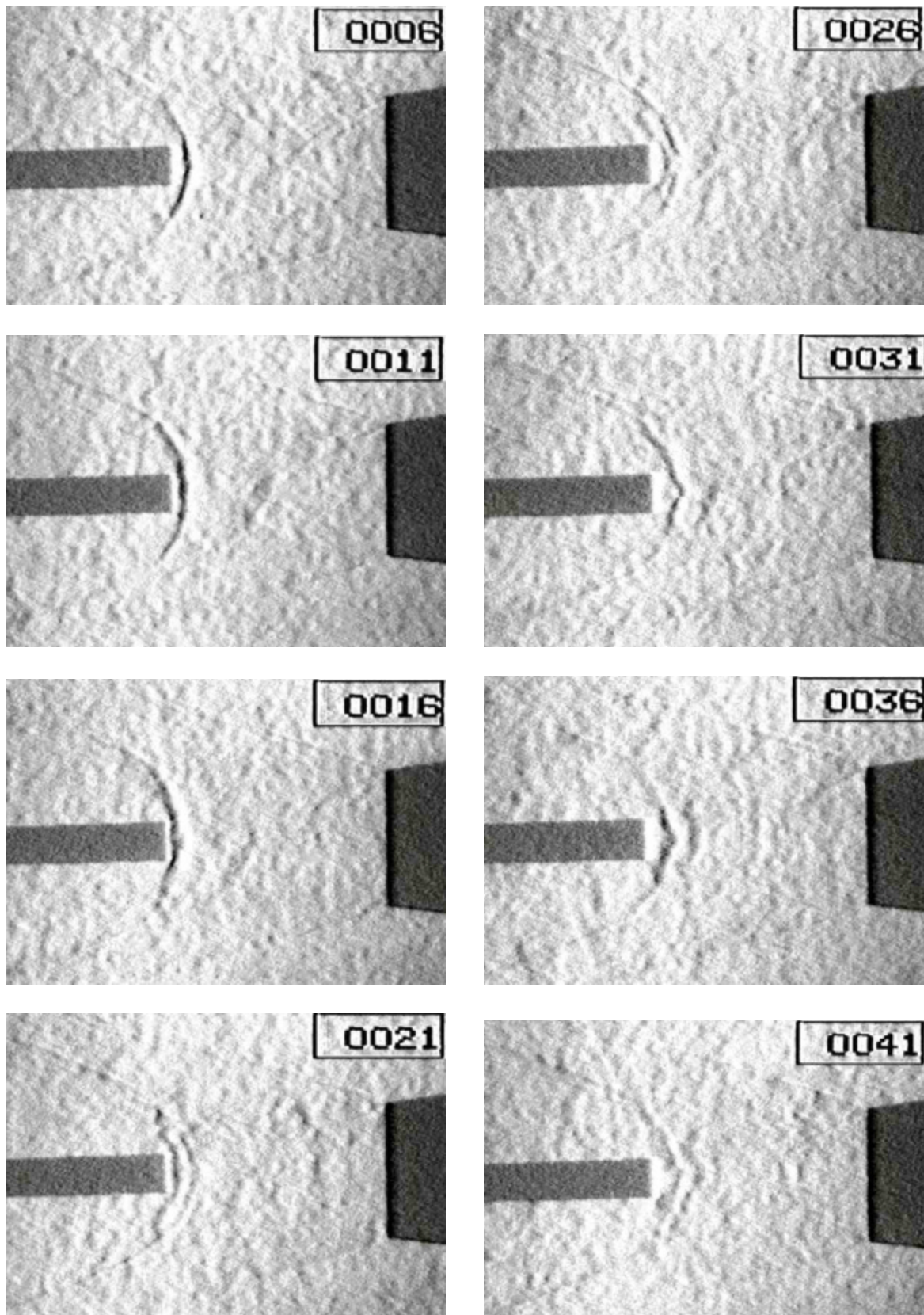


Fig.5.3. Schlieren images of MW discharge interaction with 8mm AD-body in  $\text{CO}_2$  – (1)

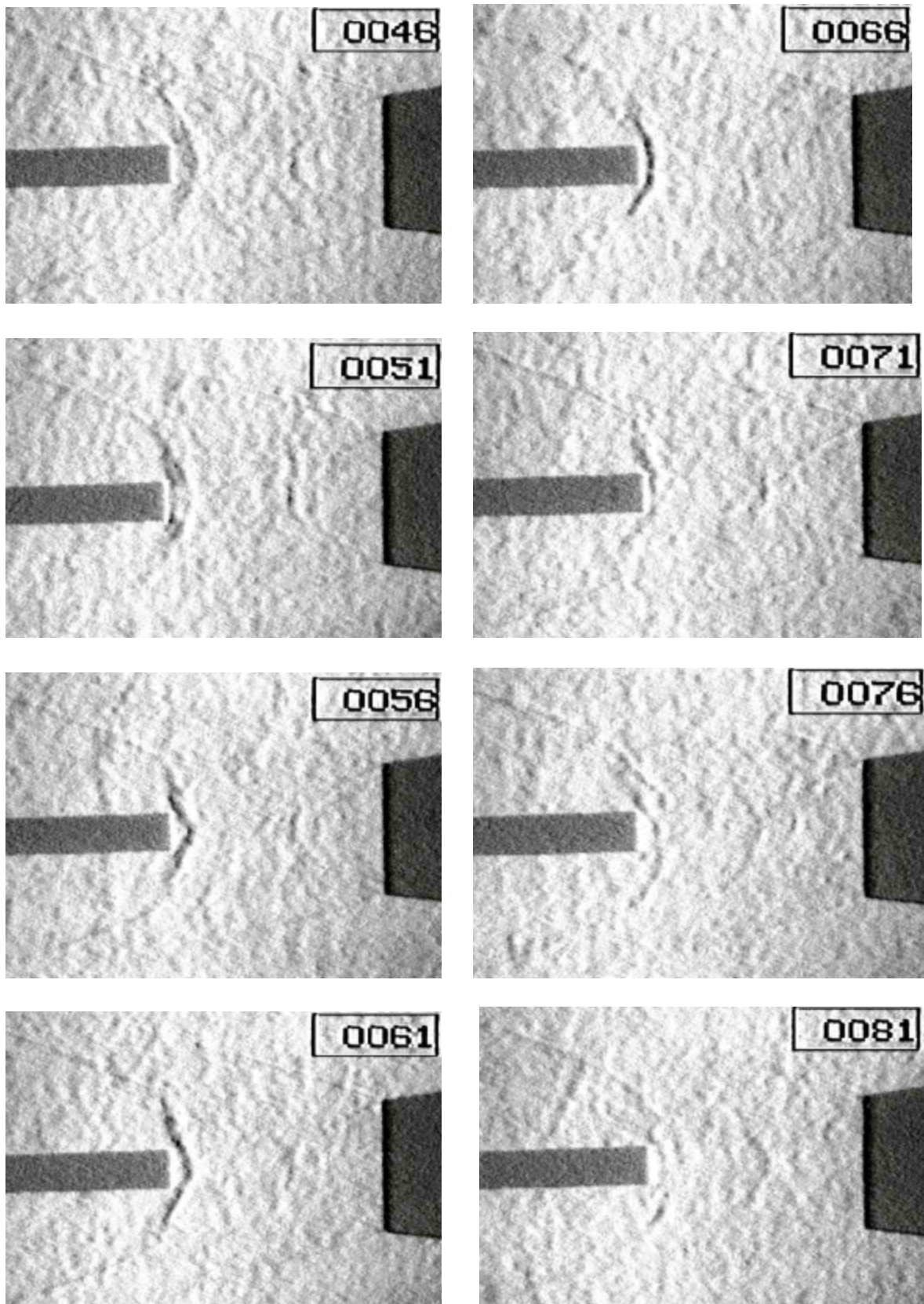


Fig.5.3. Schlieren images of MW discharge interaction with 8mm AD-body in  $\text{CO}_2$  – (2)



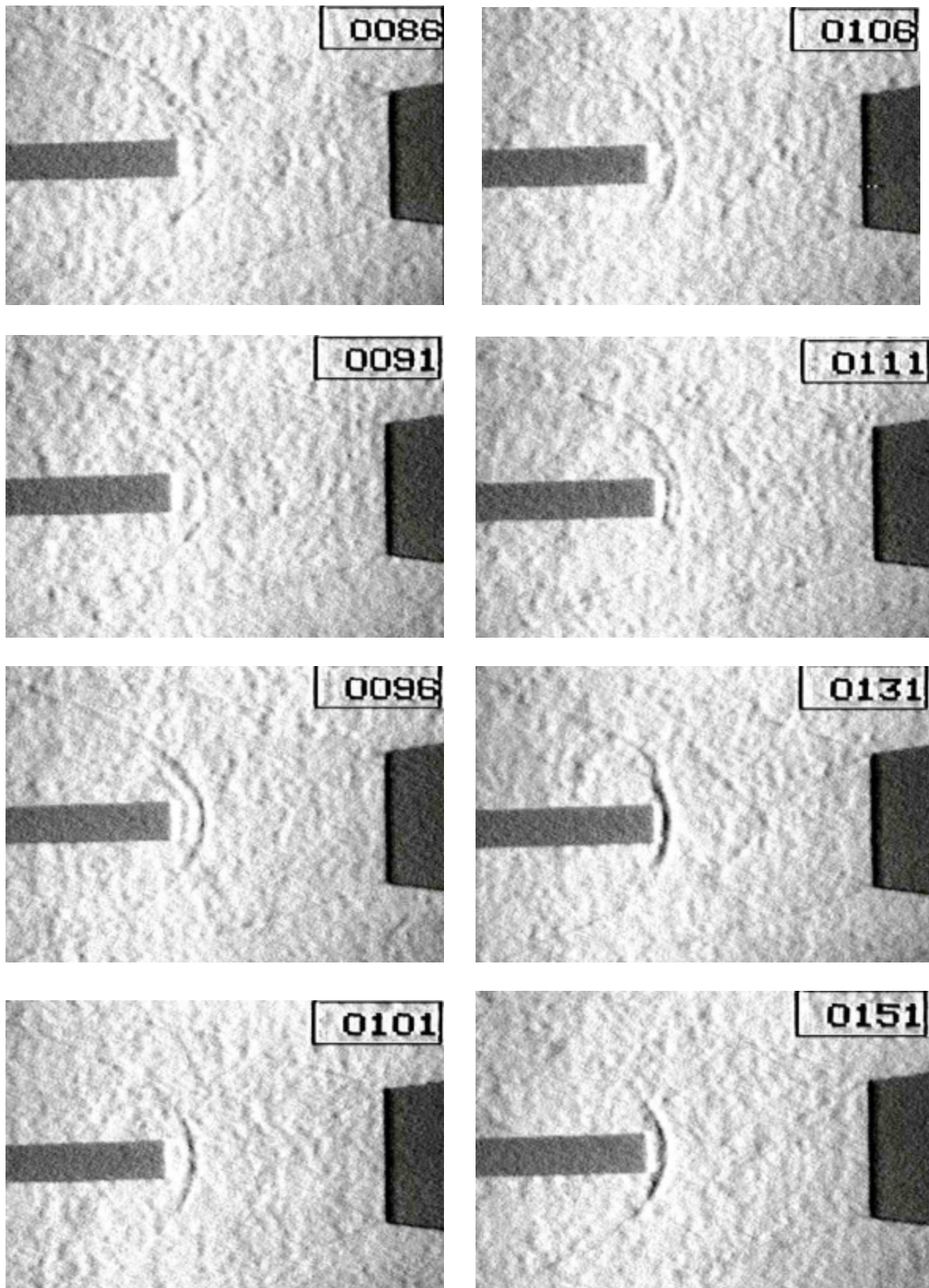


Fig.5.3. Schlieren images of MW discharge interaction with 8mm AD-body in  $\text{CO}_2$  – (3)



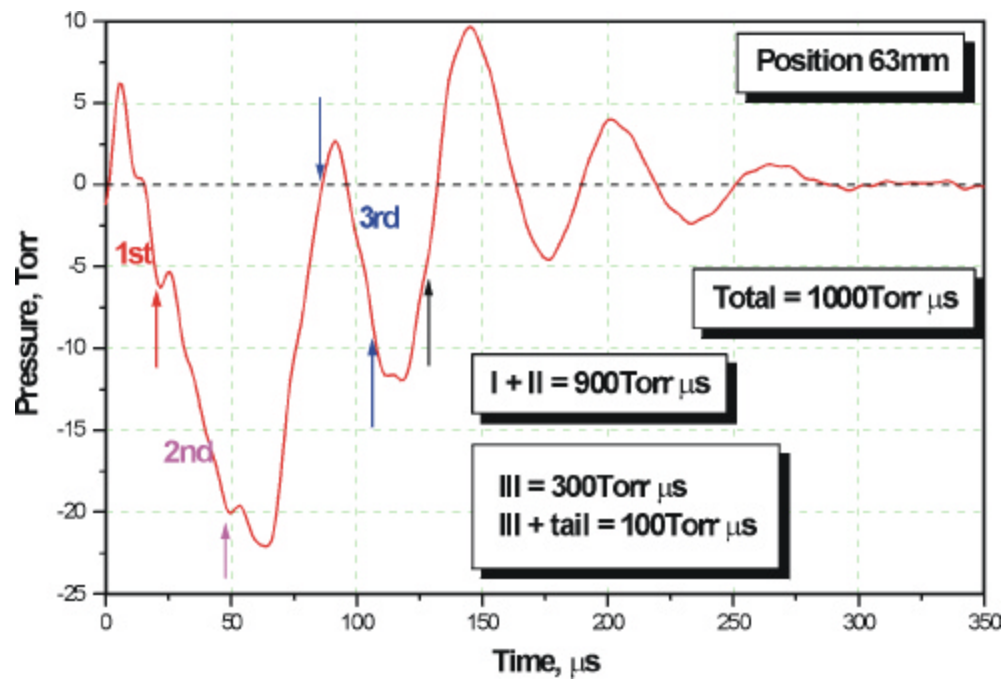


Fig.5.4. Differentiation of discharge regions effect at stagnation point

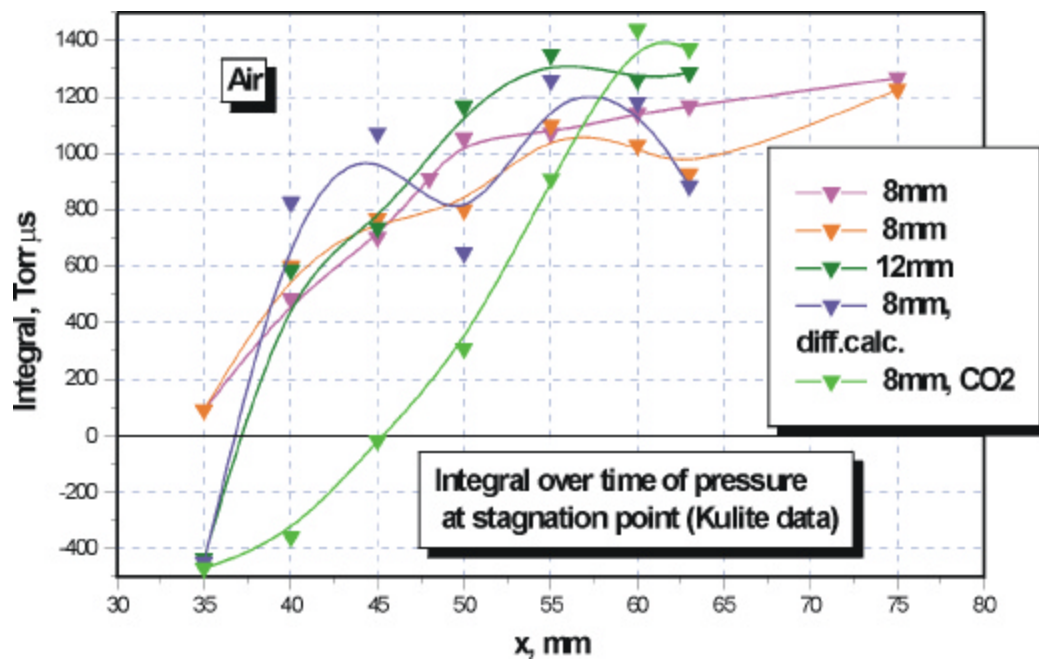


Fig.5.5. Integral effect of MW discharge at stagnation point vs model position

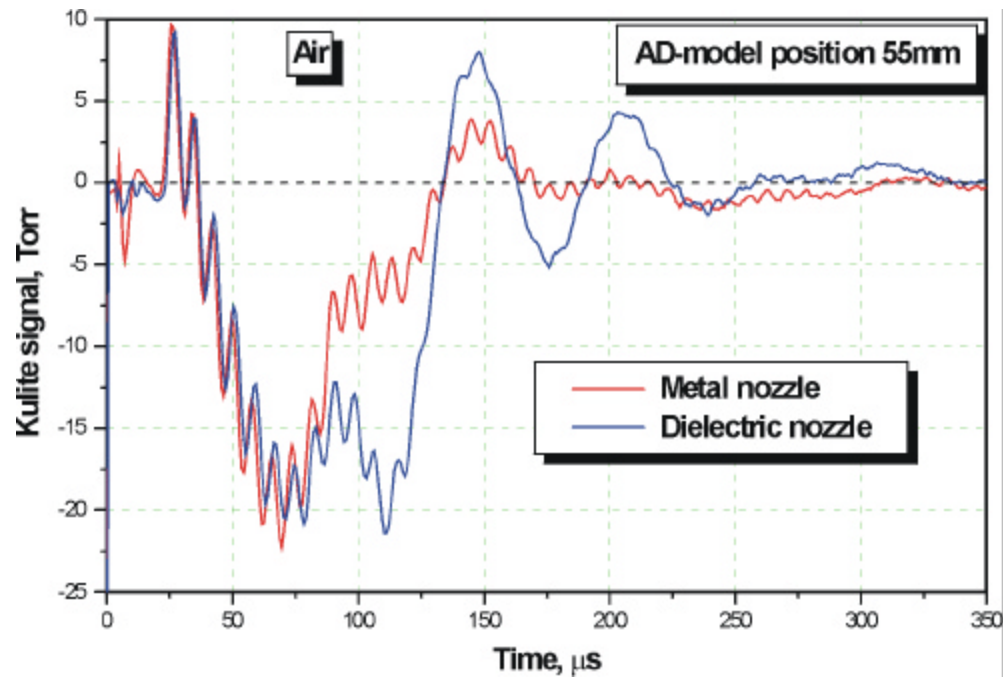


Fig.5.6. Illustration of the cone-domain effect as a function of domain dimension

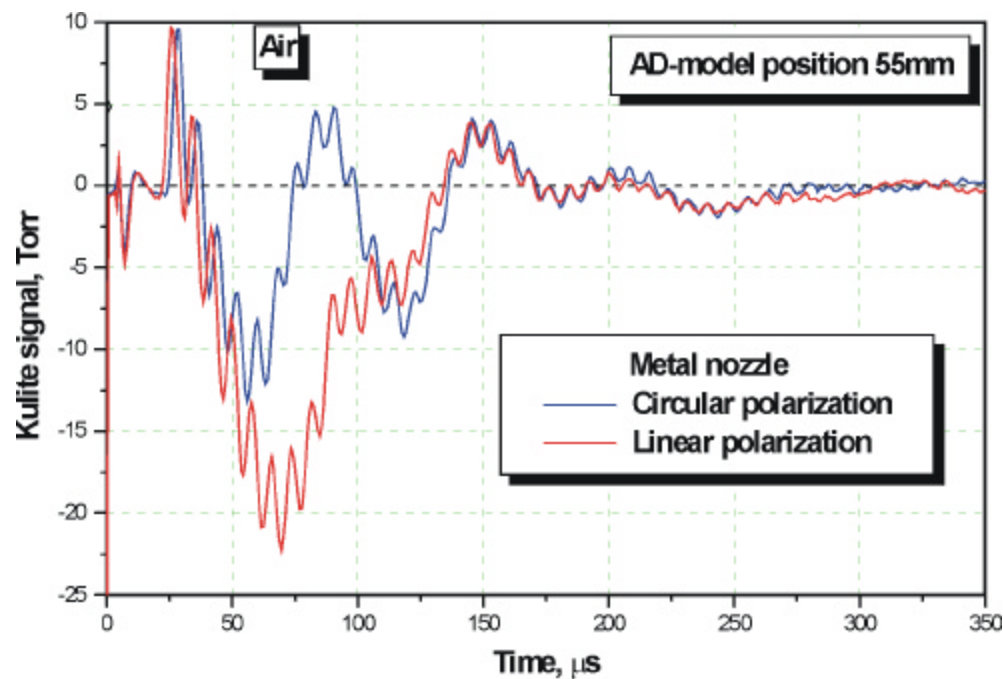
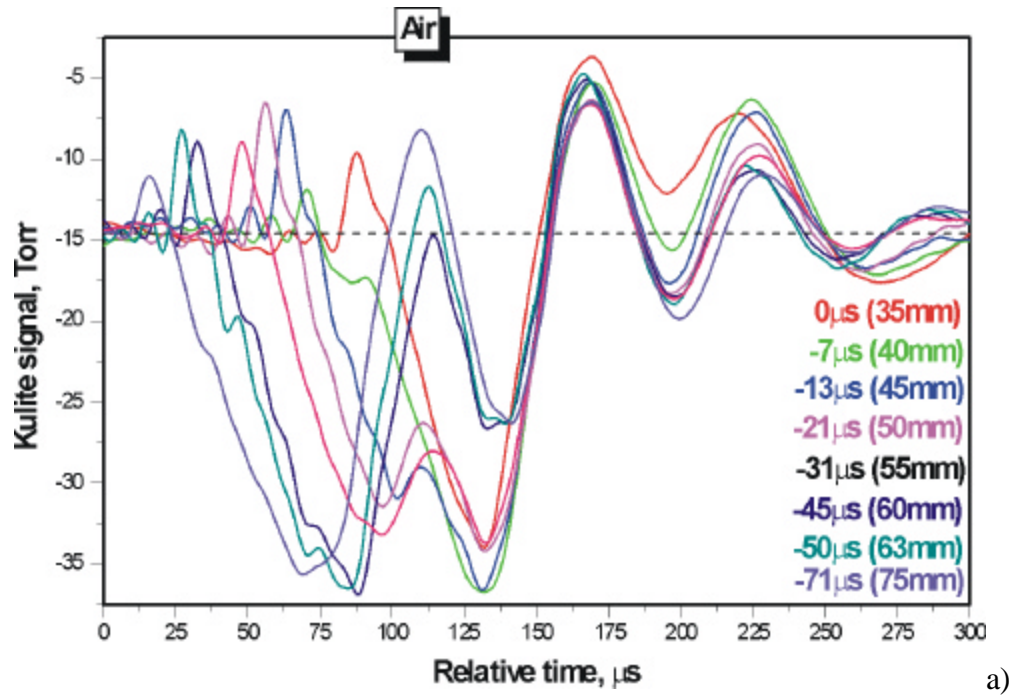
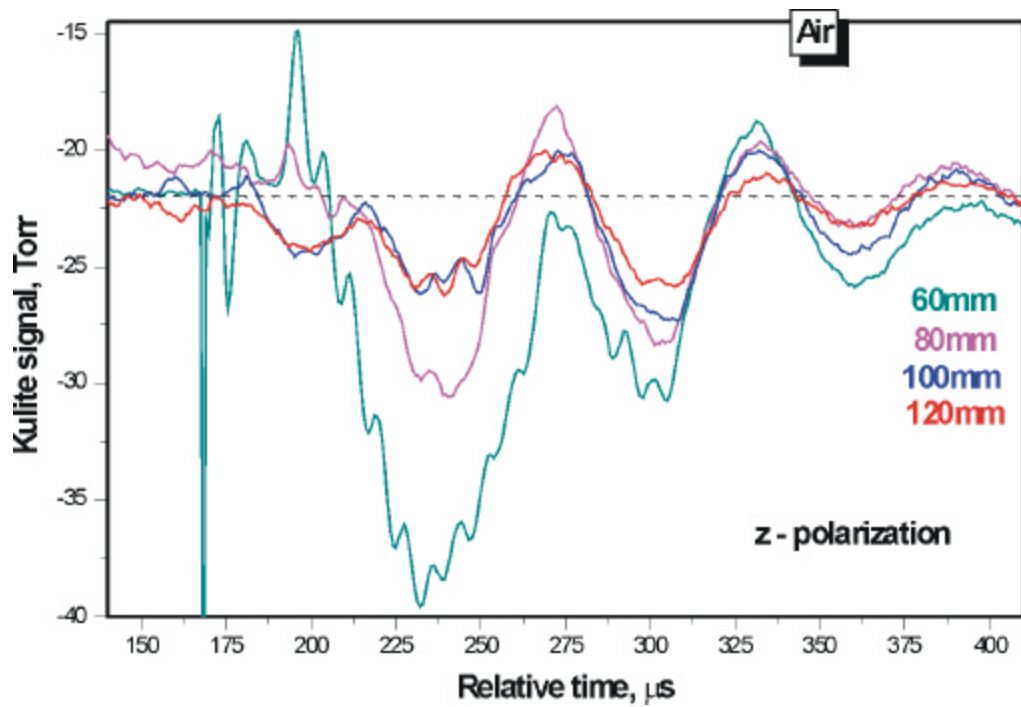


Fig.5.7. Illustration of energy concentration effect



a)



b)

Fig.5.8a,b. Stagnation pressure evolution at different AD-model positions in working (a) and remote (b) domains

## Supplement

### **S1. Realization of x-elongated configuration of MW field in the working flow region**

Elongation of plasmoids in the direction of gas flow for increasing of intensity and duration time of gas dynamic disturbance interaction with the AD model is one of the ways for the process optimization. To realize this scheme, the direction of MW flux coming to the working flow region was to be changed. This has been done by installation of additional (new) radiating and focusing systems. The view of the chamber after this modification is presented at Fig.S1.1. In this scheme MW energy is radiated by a pyramidal emitter (which is covered by radio-transparent shirt), passes through the gas streams and lightens the parabolic mirror, the last being installed near the upper plain of the chamber. The mirror focuses MW flux in such a way that the main maximum of electric field is positioned along the central axis of the working region of the flow. The measured distributions of EM field in xy- and xz-planes are shown in Fig.S1.2.

*Discharge structure.* The first experiments for MW discharge ignition in this configuration have been provided. The photos of discharge in air and argon under different AD model positions are presented at Fig.S1.3- S1.4. MW discharge structure which is seen at these photos confirms the field structure presented above. According to this distribution, x-elongated discharge channel is burned along the central axis of the flow. The length of discharge in x-direction in air is about half a wave, also smaller plasmoids are burning 10mm above and below the main one, just at the border of the working and external (ejector) flows. When AD model occupies the total focal region, the discharge covers the model practically along its full length. Discharge in carbon dioxide had practically the same structure.

Experiments in argon were provided at a reduced impulse MW power. It can be seen that only single plasmoid is formed in this case and it has elongation in the direction of the flow. The BSW is visualized by the discharge when the last is displaced downstream the flow from the focal region.

Despite of the MW field structure has been changed in comparison with the previous case, i.e. y-polarization, the dimensions of the channel-type plasmoid (the cone-type one was absent now) turned out to be same. The channel was 17...18mm in length and 4...5mm in diameter in air. In carbon dioxide it was more consolidated and the channel resembled a thread, its diameter being more than twice less than in air.

The energy absorption in MW discharge was a function of the model position and, as in the cases of y- and z-polarization had a distinct maximum in interval 50...60mm from the central nozzle.

*Schlieren imaging.* Schlieren pictures with time gating of gas-dynamics in the case of x-polarized discharge were obtained in air and carbon dioxide. For 8mm AD-model (blunt nose cylinder) the BSW stand-off attained the value of 9...10mm, whereas the standard one is about 4mm. The maximum in stand-off position in air was observed after 50...60μs after MW pulse. Modification of the BSW under its interaction with MW discharge region is well seen at Fig.S1.5.

Very similar effects were obtained in carbon dioxide, but in contrast with y- and especially z-polarized discharge, these effects were not so distinct, may be due to not so developed discharge.

*Pressure evolution at stagnation point.* Measurements of pressure evolution at stagnation point of AD-models in air were also provided. AD-models were blunt nose cylinders 8mm, 12mm and 16mm in diameter. Thus, testing was made for the models with dimensions from noticeably less to approximately equal to the discharge channel length.

The structure of the Kulite signal turned out to be very similar to that obtained in y- and z-polarized discharge (Fig.S1.6-S1.7). Moreover, the values of maximum pressure deficit practically coincide with those obtained in previous experiments with y-polarized discharge (at least for the situation of the most intensive action, i.e. model position 55...60mm). These maximum values depend upon the model radius, demonstrating the linear increase in the radii range 8...12mm and being saturated for the 16mm model. In opposition, the integral pressure impulse  $I = \int \partial Dp \times dt$  rises practically linear with the model radius (Fig.S1.9).

High and low frequency oscillations are also present in the case of x-polarized discharge (compare appropriate curves at Fig. S1.6-S1.7), the values of their frequencies being also the same.

Effect value strongly depend on the model position downstream the flow (Fig.S1.8), decreasing with the increasing of the distance from the discharge. At model positions after 55mm the discharge structure is not influenced by the model and such a comparison of efficiency is valid.

As a brief summary of this part of investigation a conclusion can be made that at AD model position where the effect attains its maximum, it does not depend of the type of

polarization – both perpendicularly and parallel disposed plasmoids in respect to the BSW exert the same action. It is rather unexpected result which demands further clarification.

Thus, plasmoids of different spatial organization in supersonic flow were tested for the first time. Preliminary analysis shows that effect is sensitive more to the discharge volume, than to its spatial organization. At the base of investigations fulfilled thermal basis of the effect seems to be most probable.

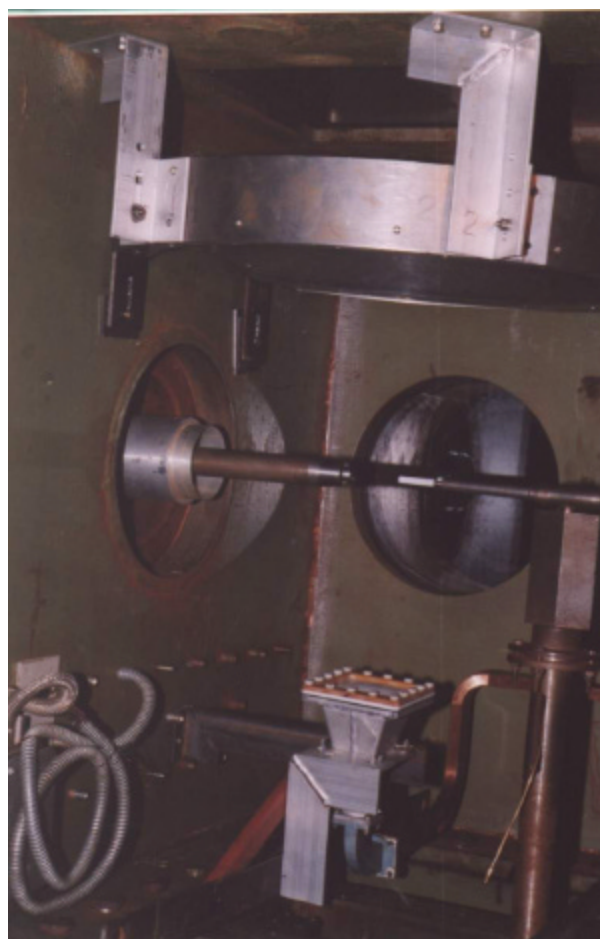
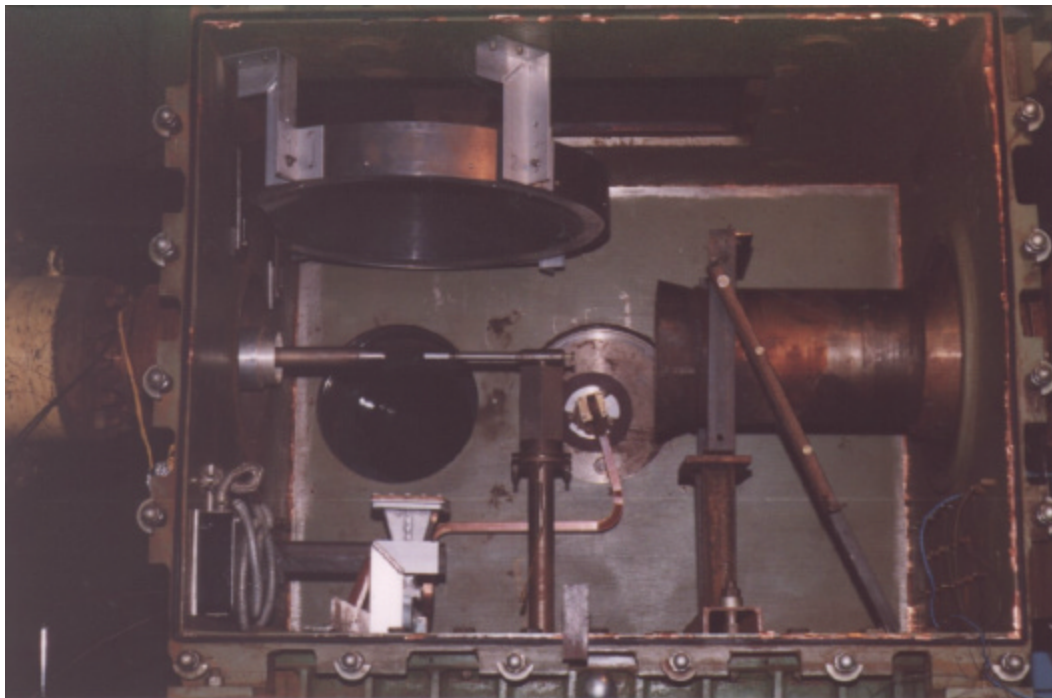


Fig.S1.1. The view of the chamber after this modification



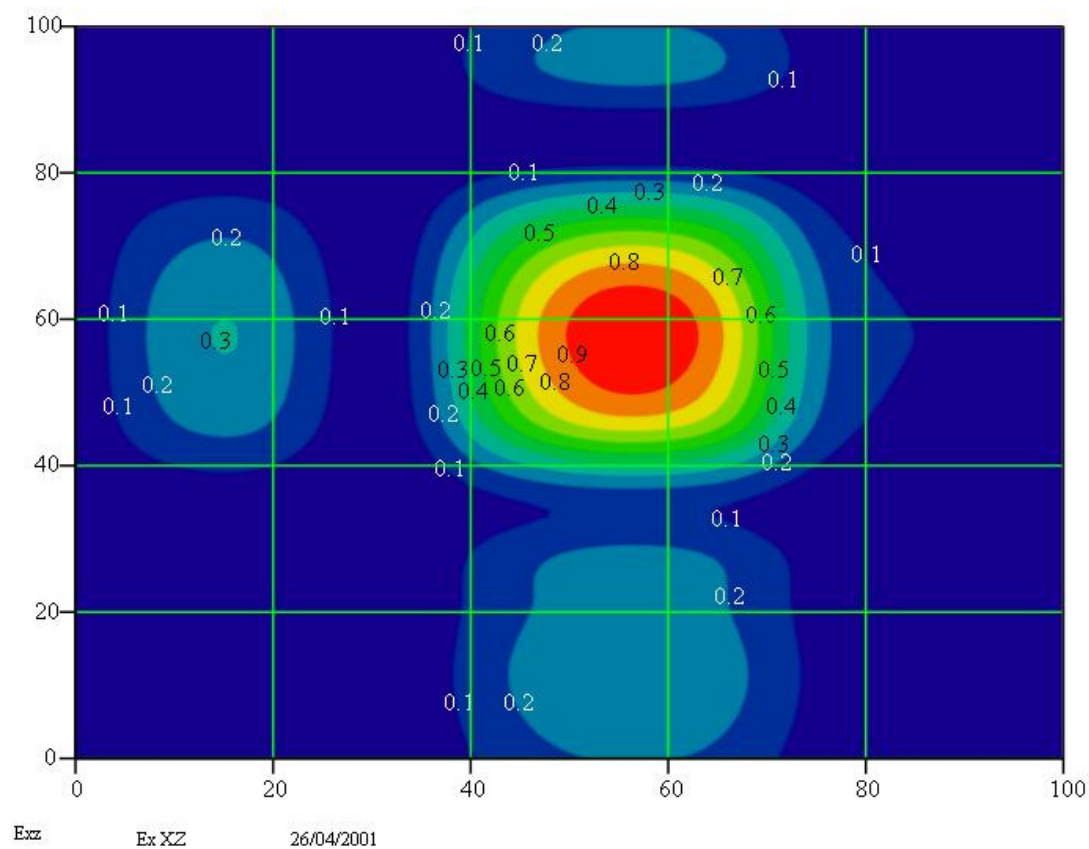
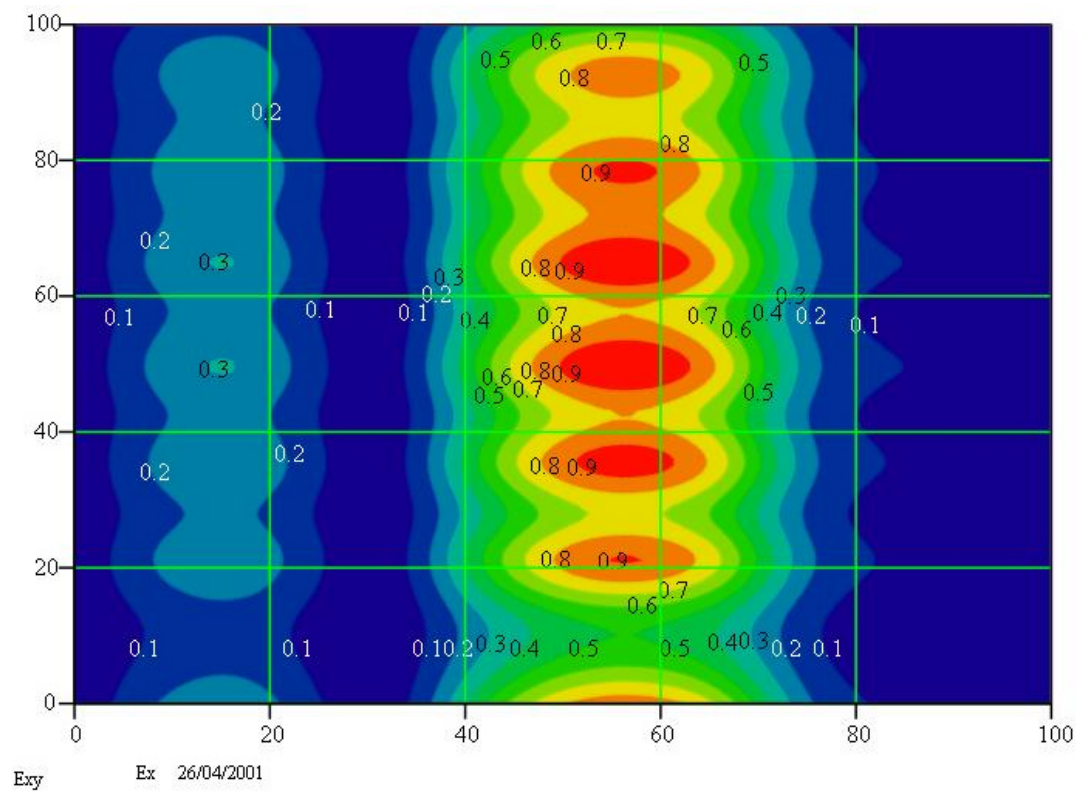


Fig.S1.2. The measured distributions of EM field in xy- and xz-planes



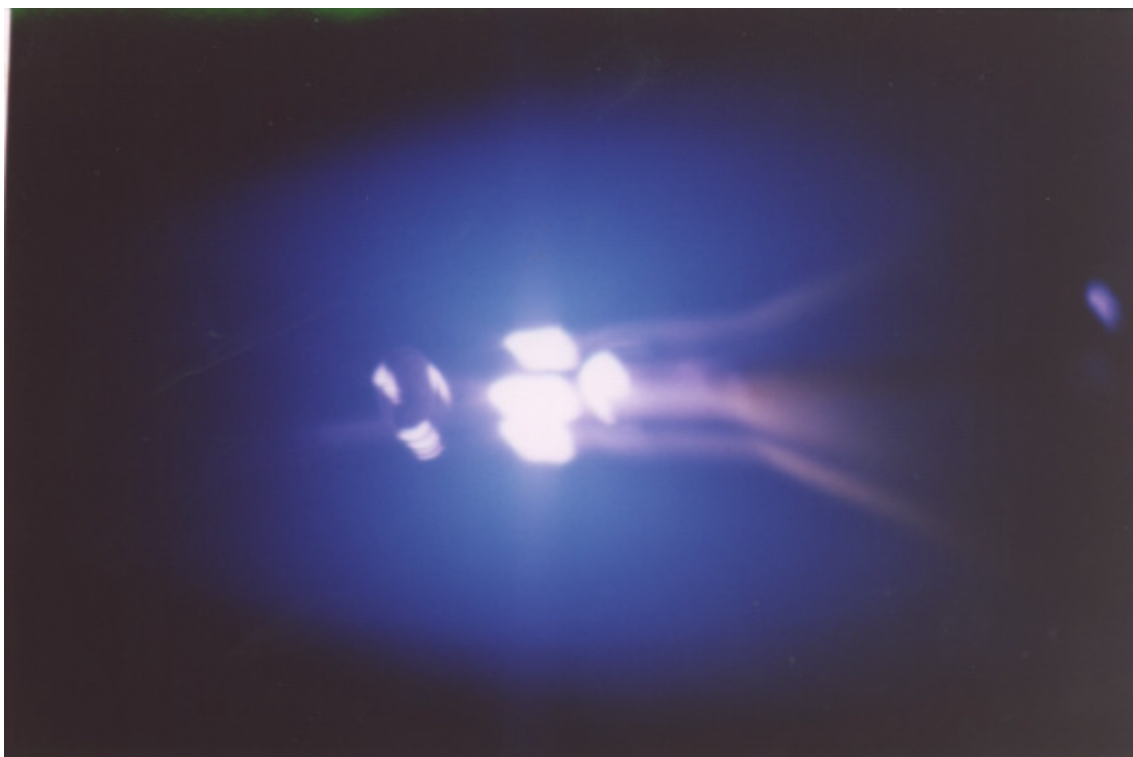
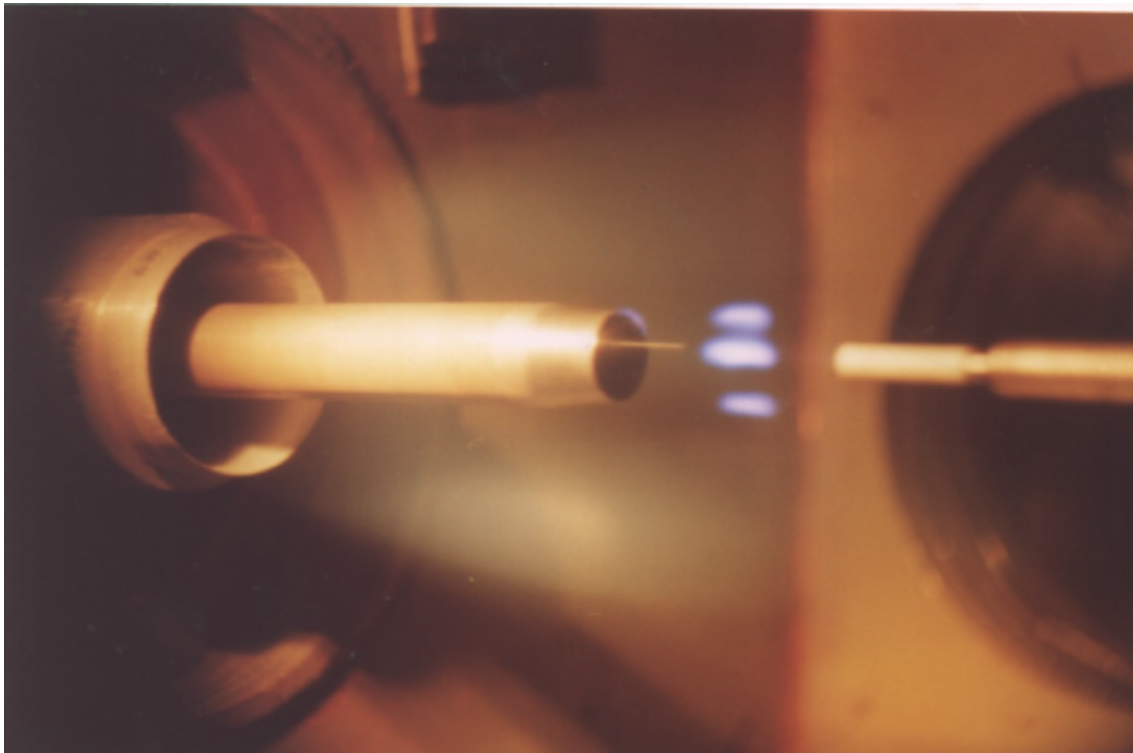


Fig.S1.3. The photos of discharge in air under x-polarized MW beam

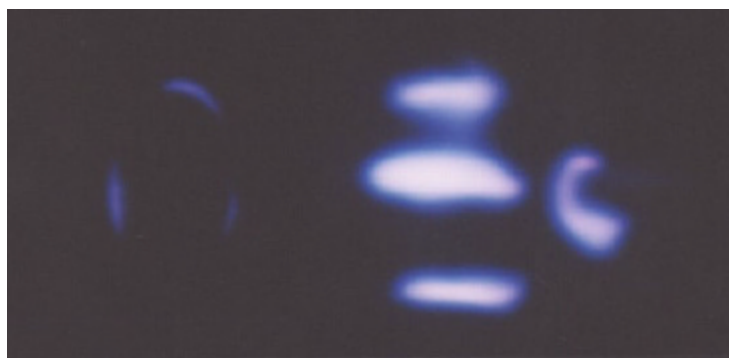


Fig.S1.4. The photos of discharge in air and argon under x-polarized MW beam

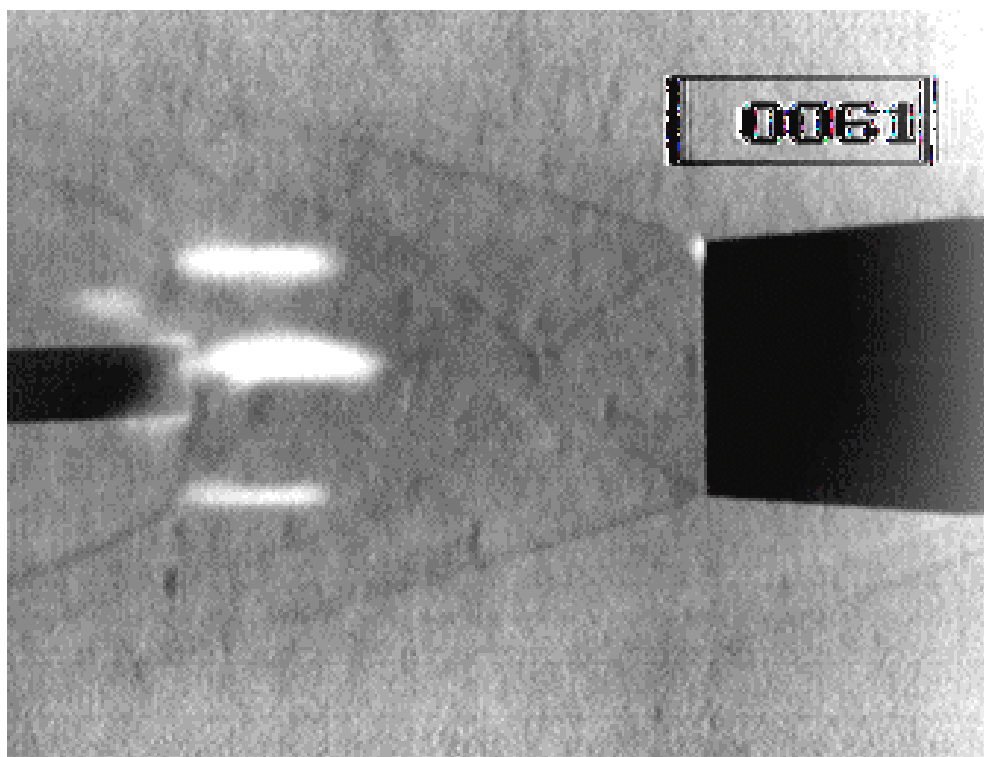
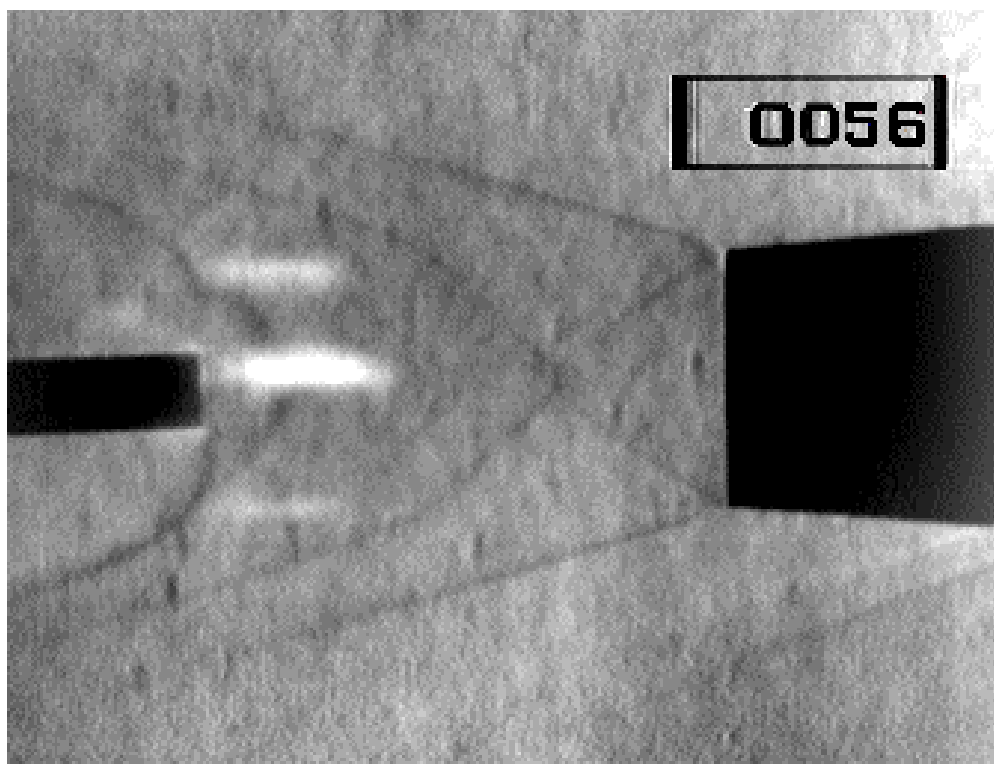


Fig.S1.5. Modification of the BSW under its interaction with MW discharge region

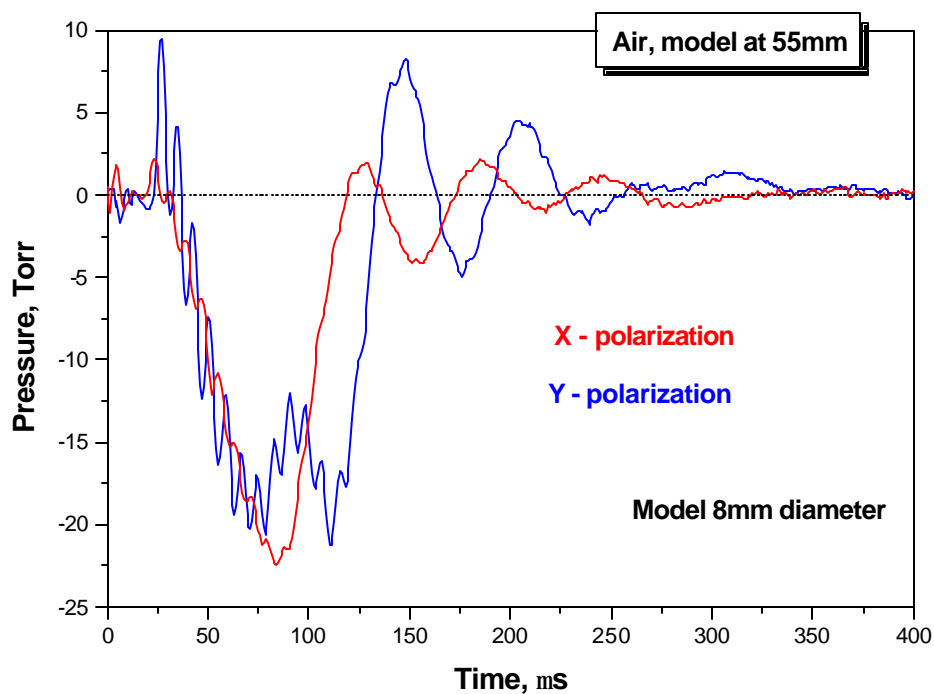


Fig.S1.6. Kulite signal obtained for 8mm AD model in y- and z-polarized discharge

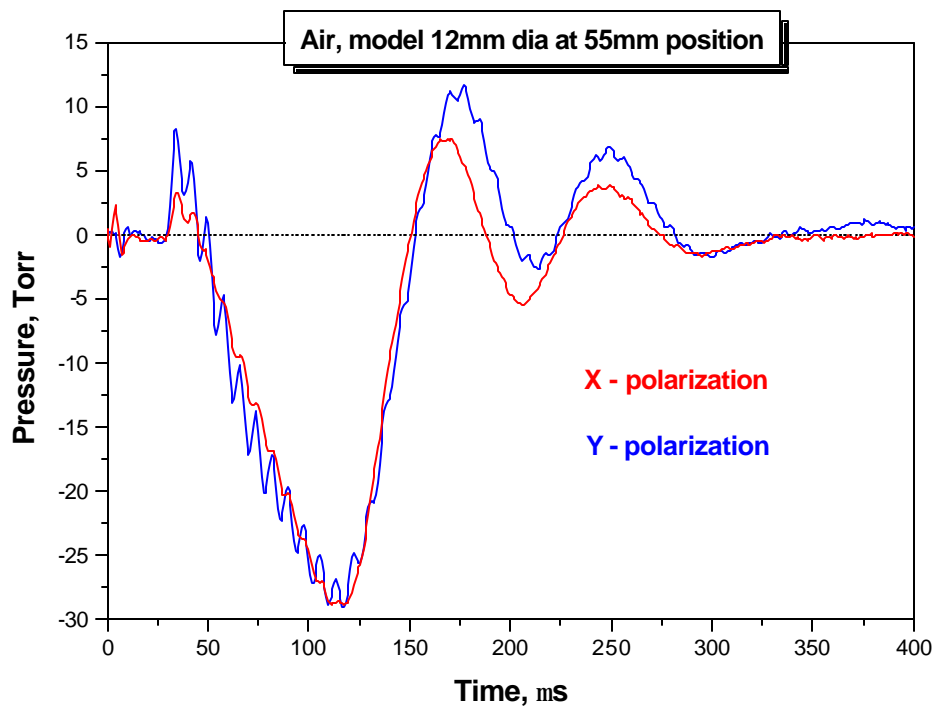


Fig.S1.7. Kulite signal obtained for 12mm model in y- and z-polarized discharge

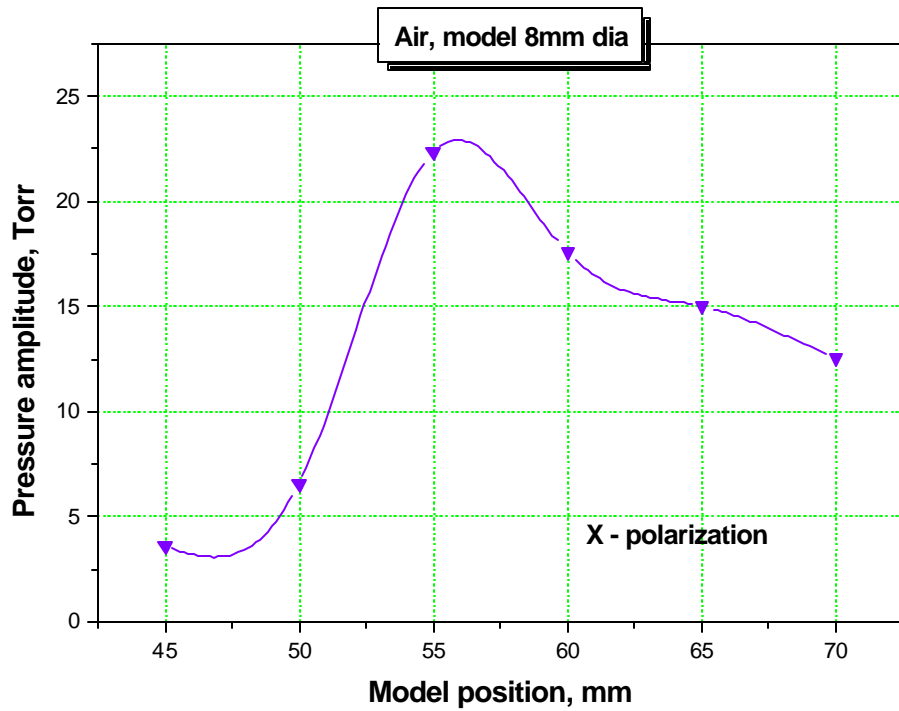
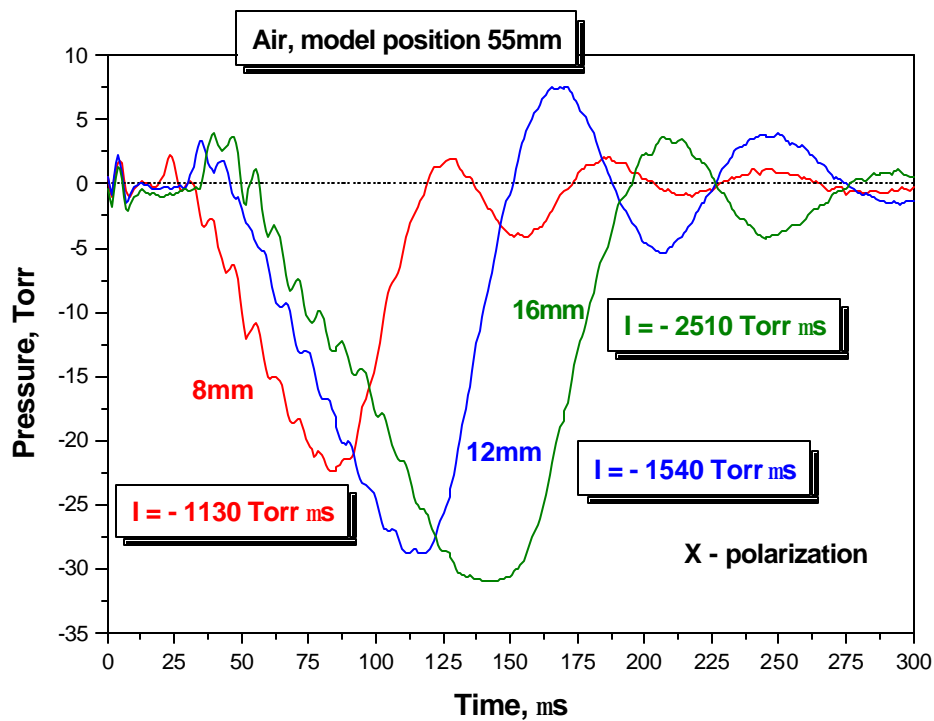


Fig.S1.8. Effect value with the model position downstream the flow



FigS1.9. Stagnation pressure characteristics variation with the model diameter

## **S2. Schlieren images of MW discharge regions interaction with the BSW**

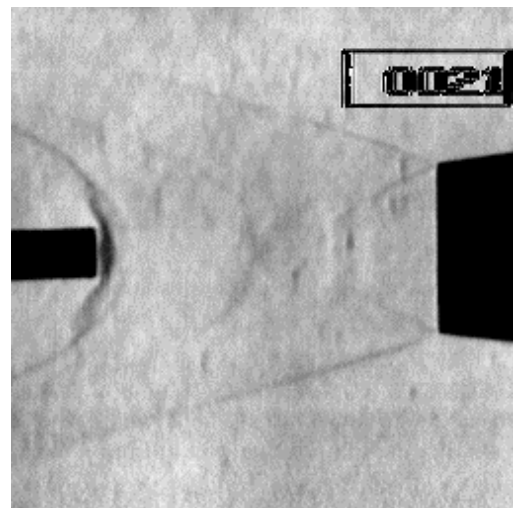
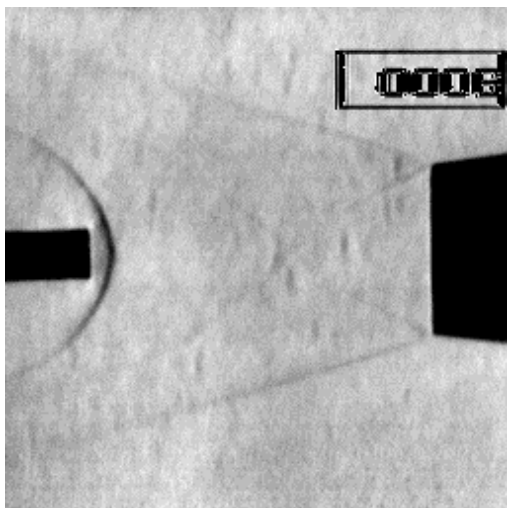
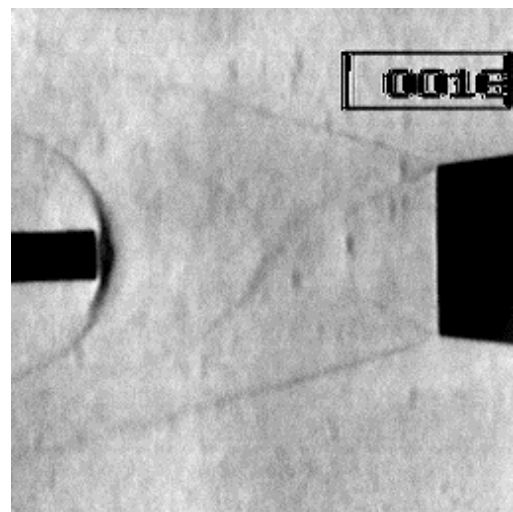
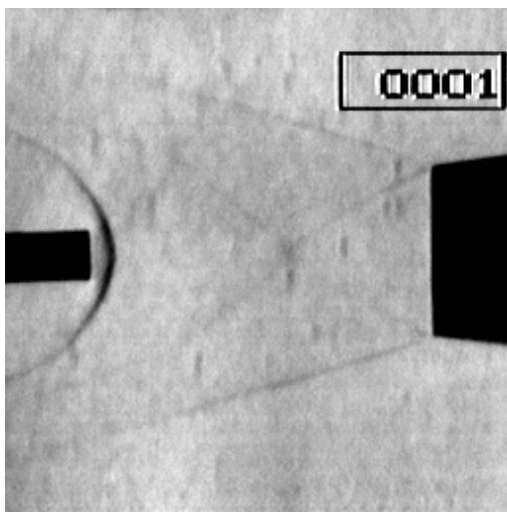
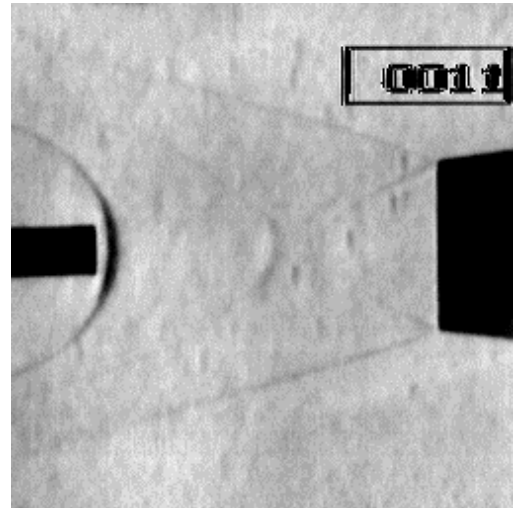
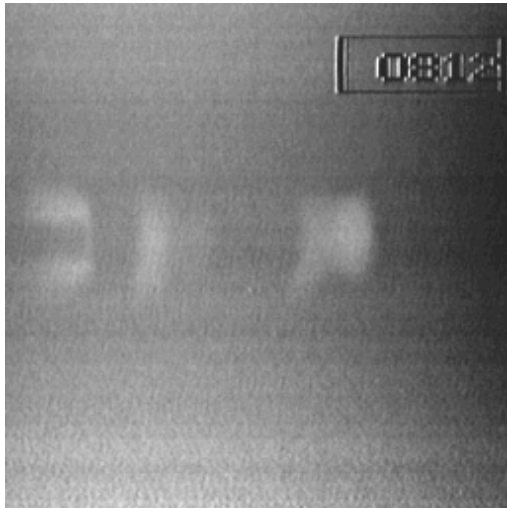
**Gas: Carbon dioxide**

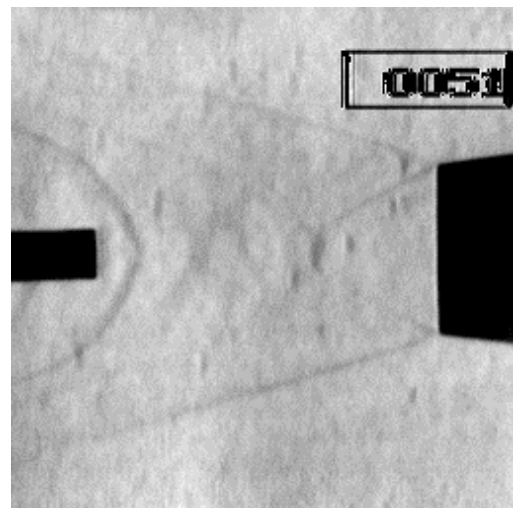
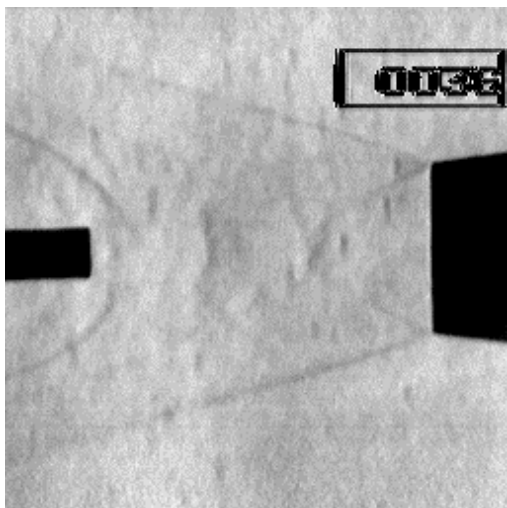
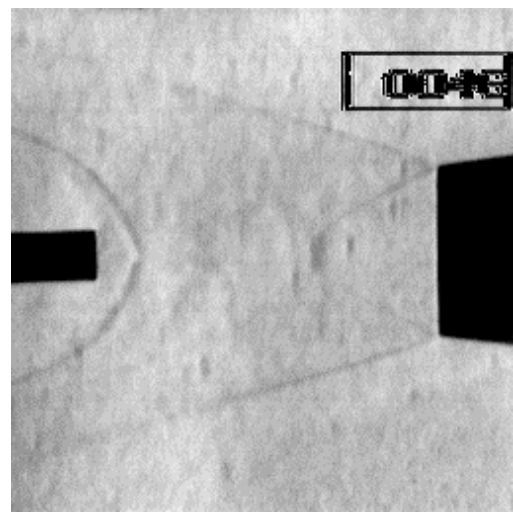
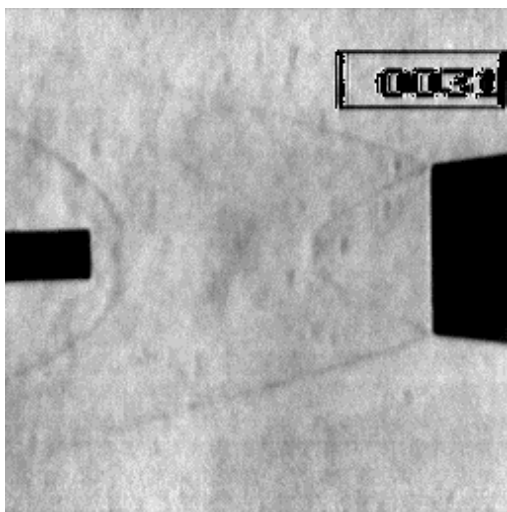
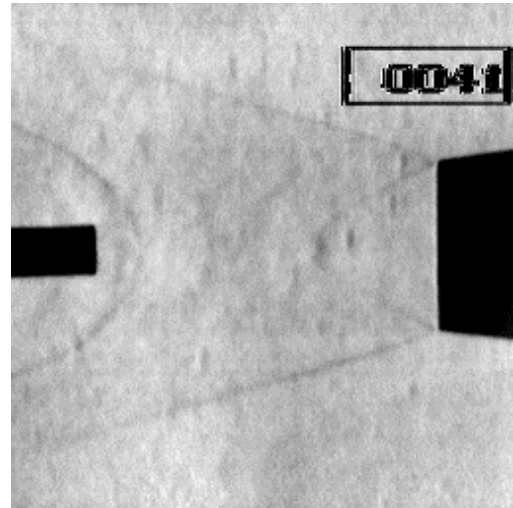
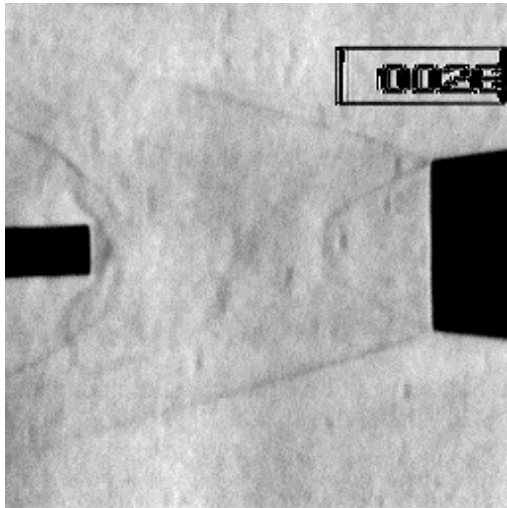
**Model: 8mm diameter**

**Model position: 55mm from the central nozzle**

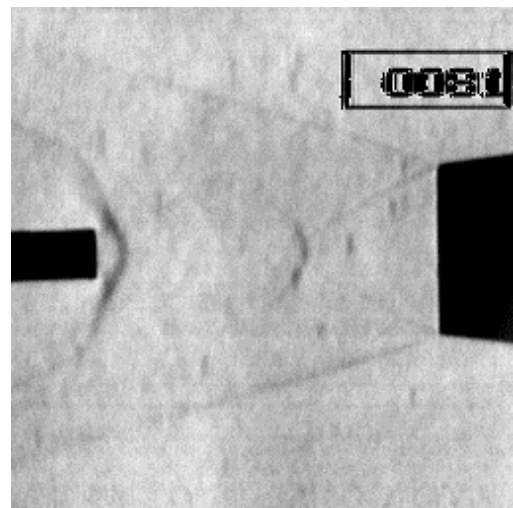
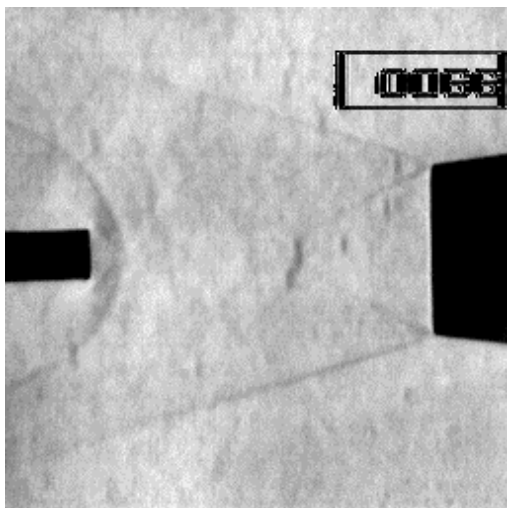
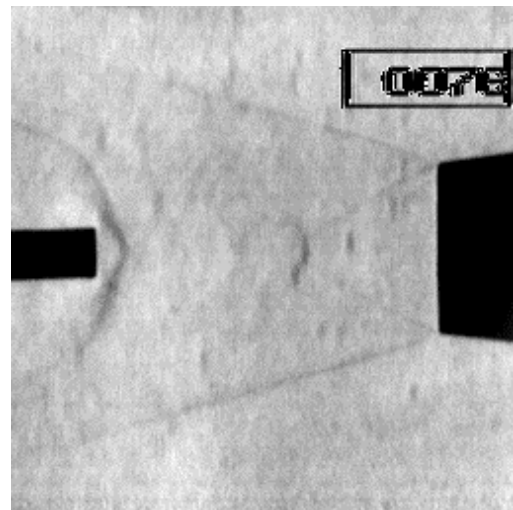
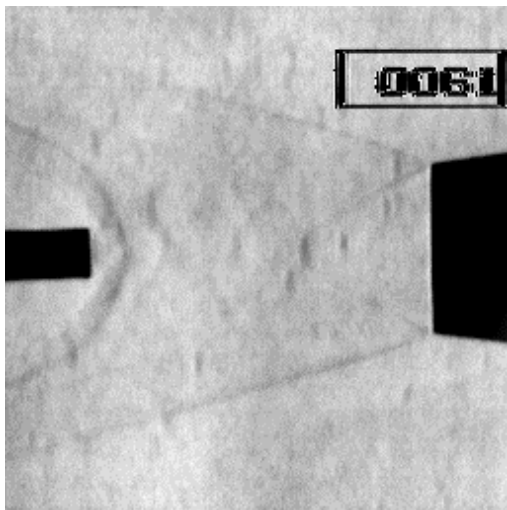
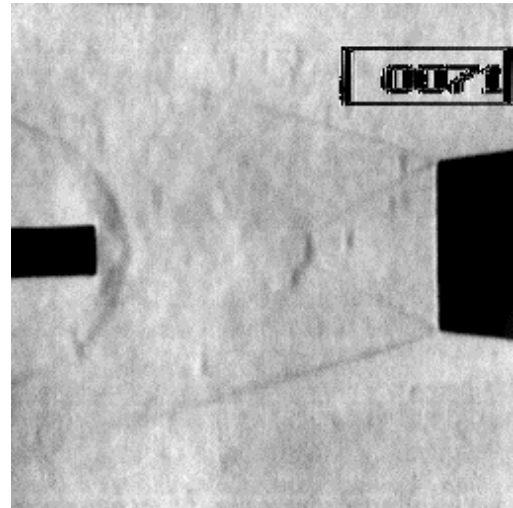
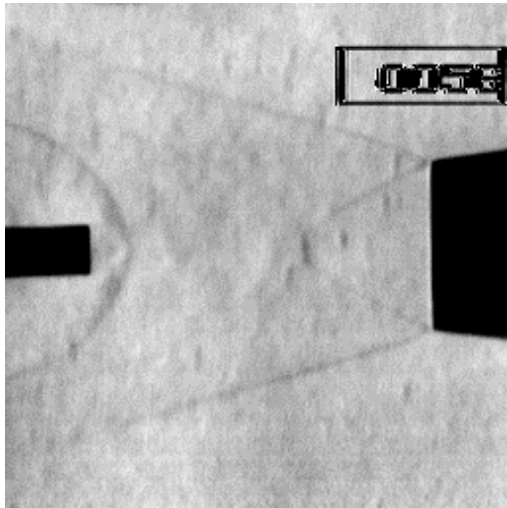
**Electric field: Y – directed**

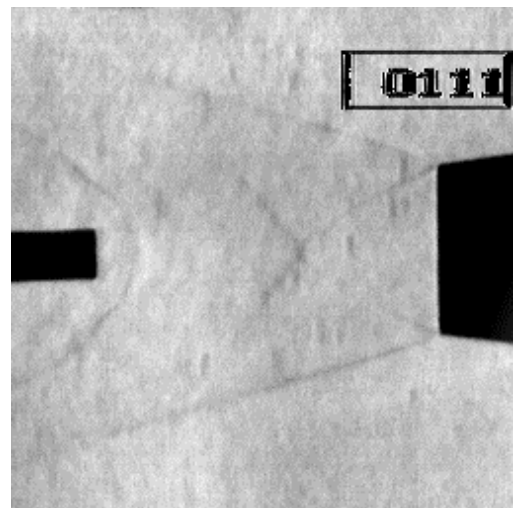
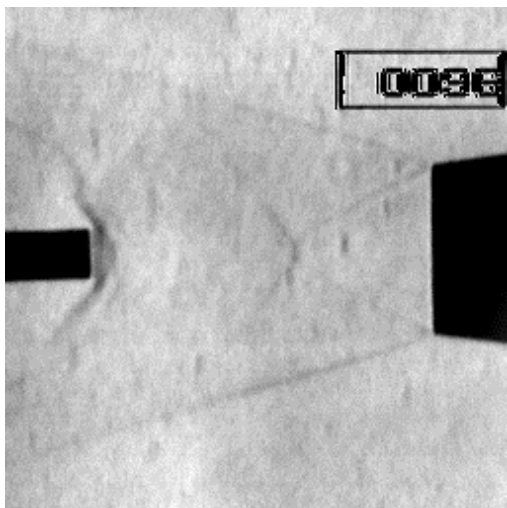
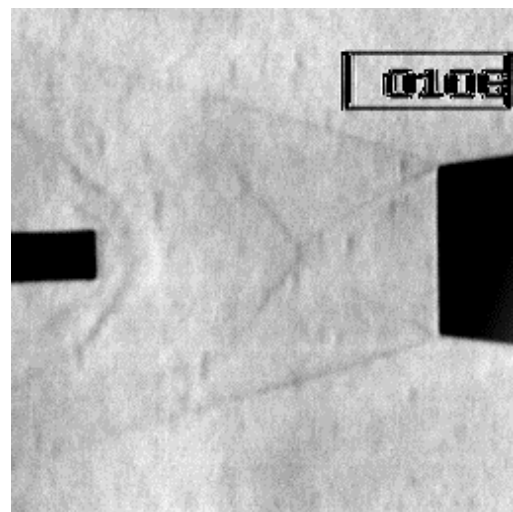
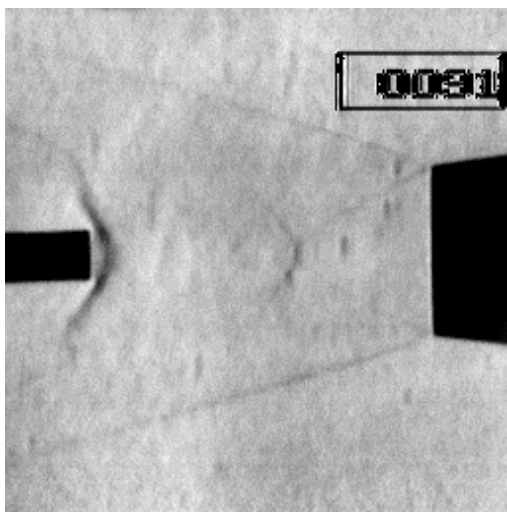
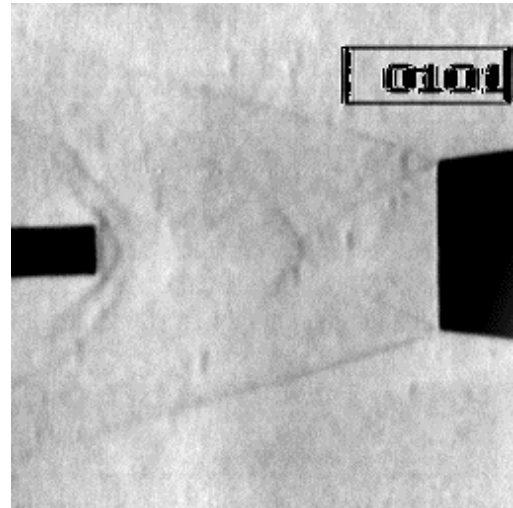
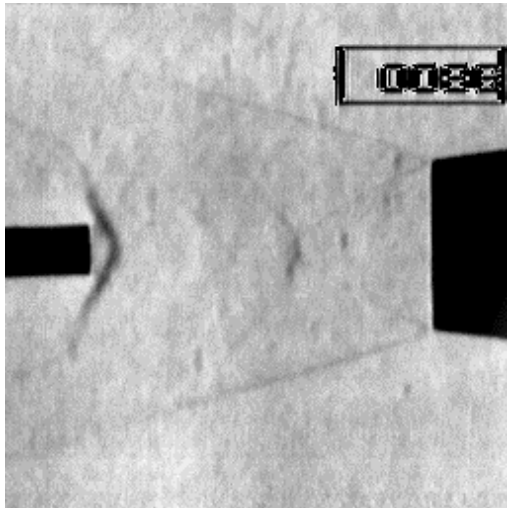
**The figure in the right upper corner of each frame is time interval  
(in microseconds) after MW pulse.**

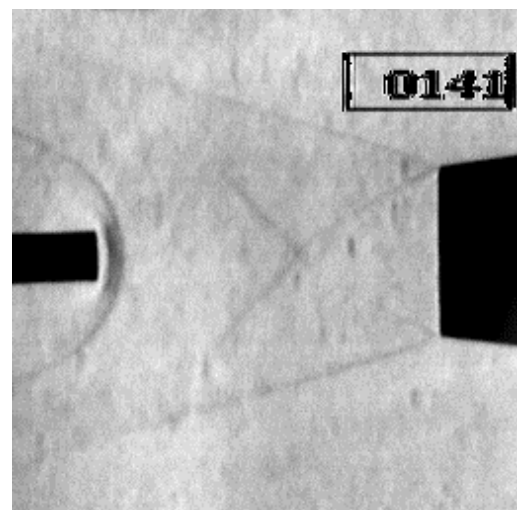
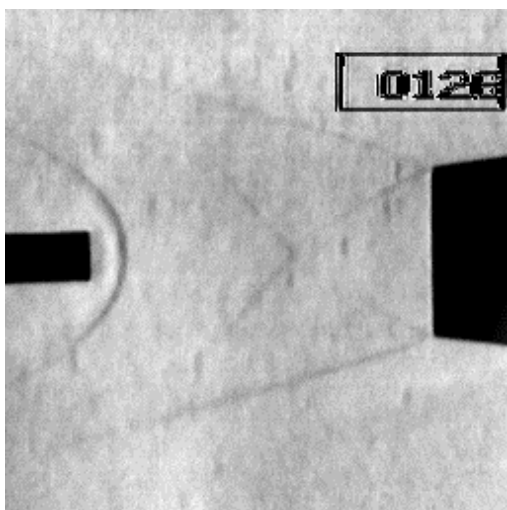
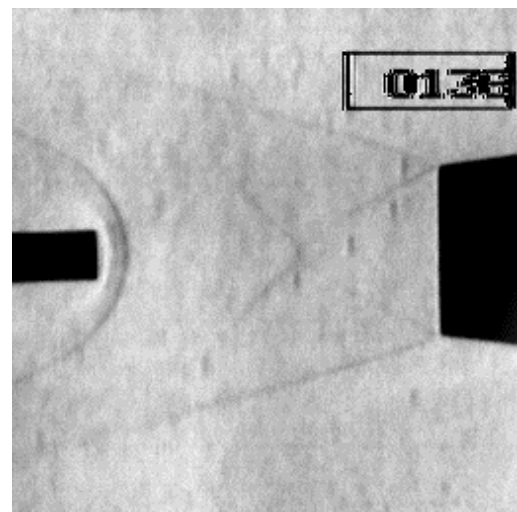
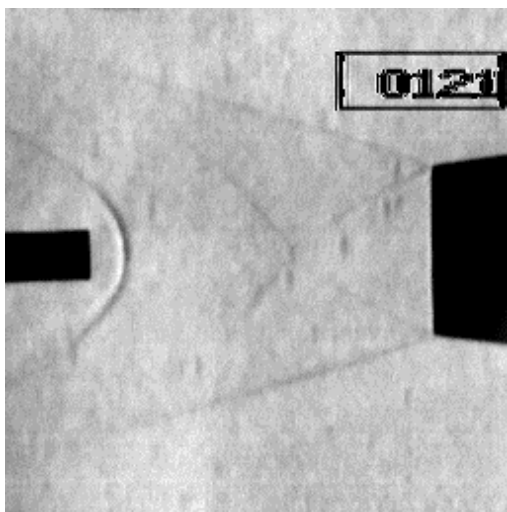
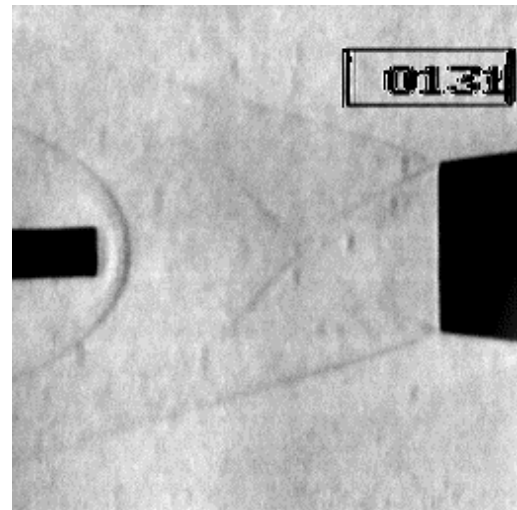
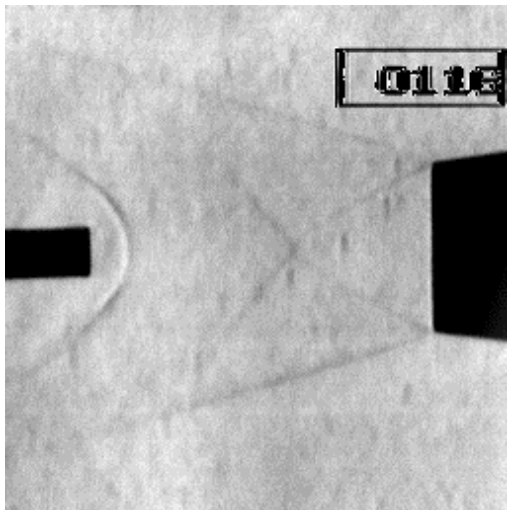


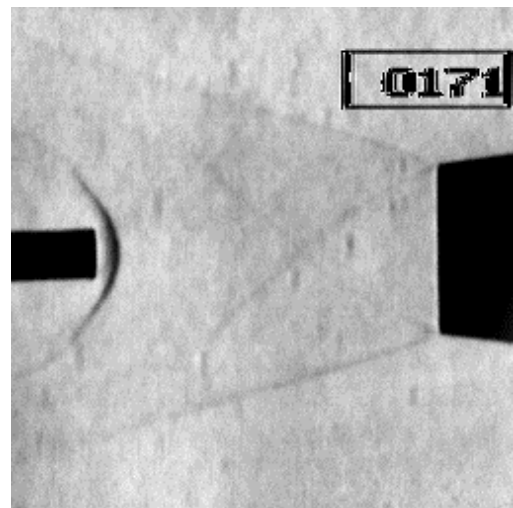
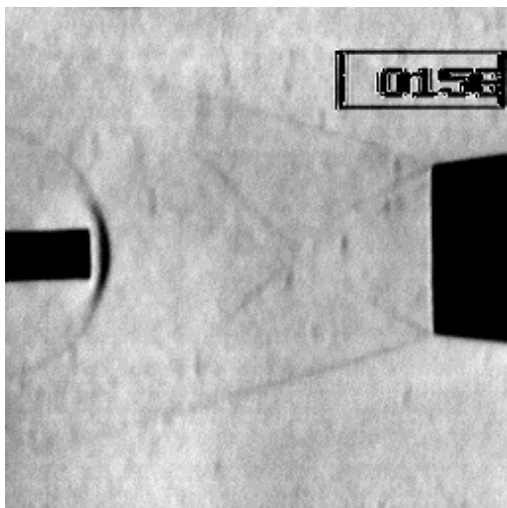
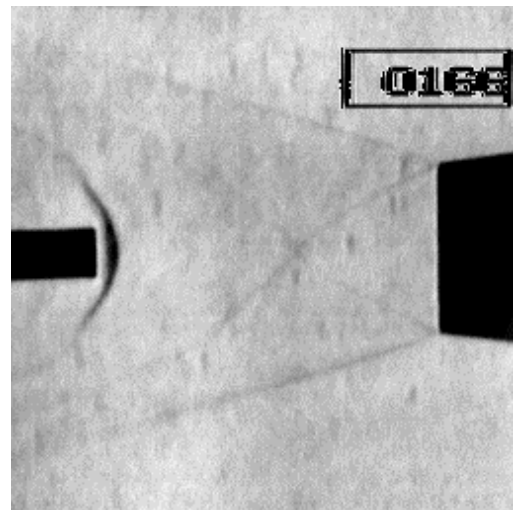
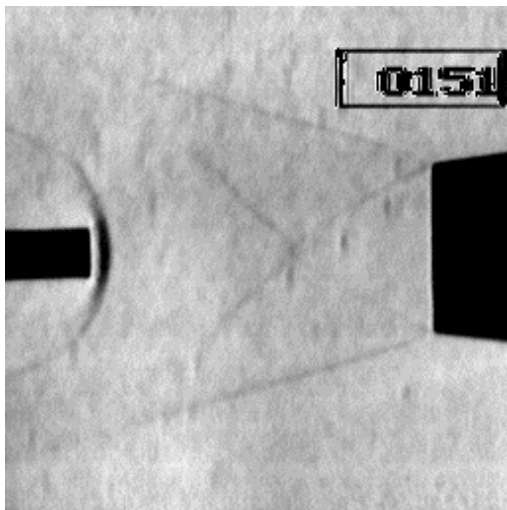
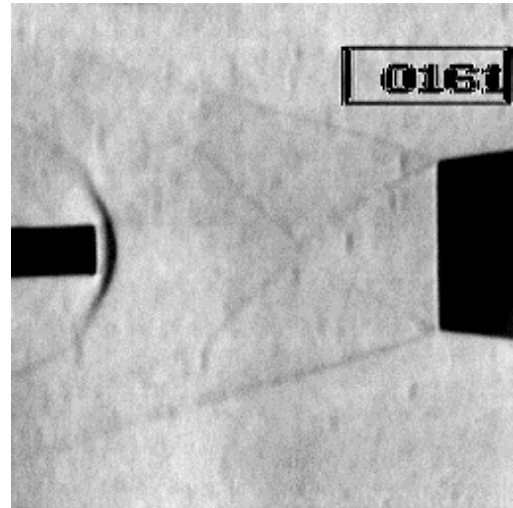
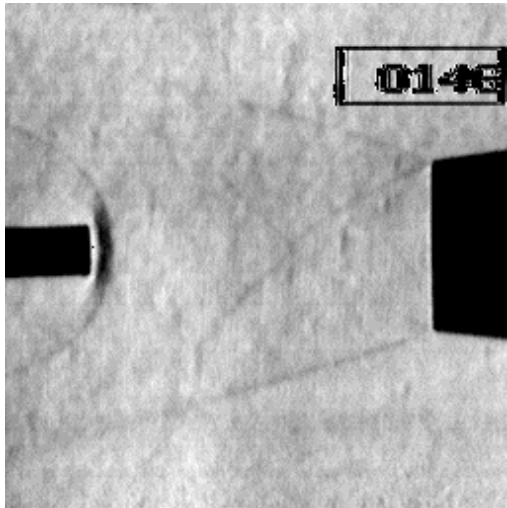


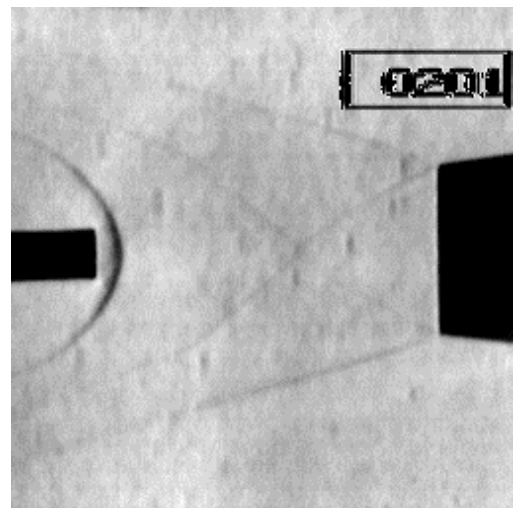
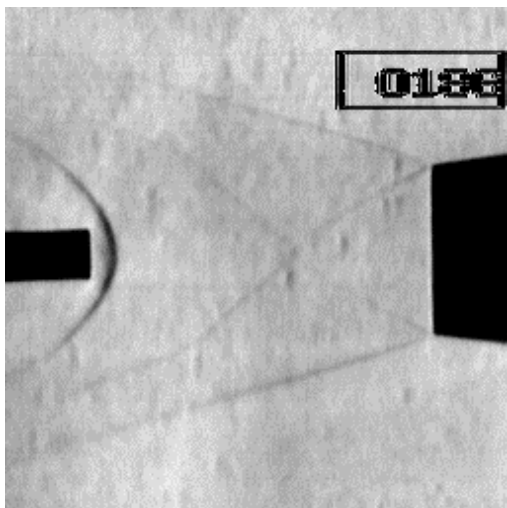
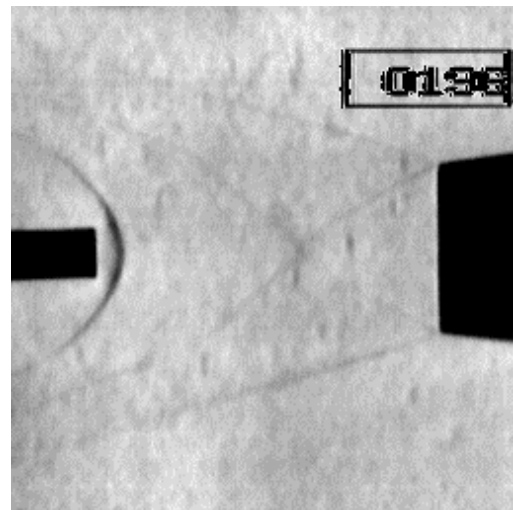
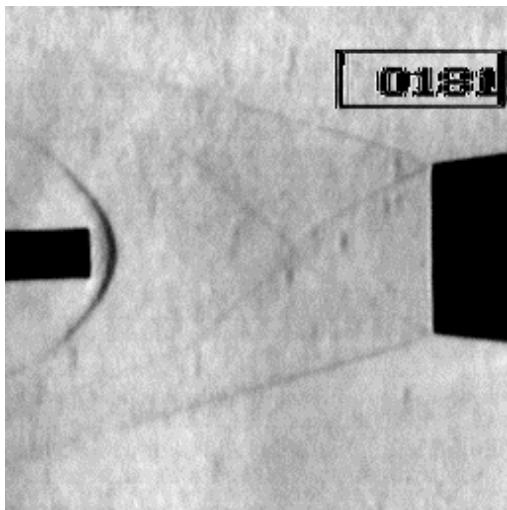
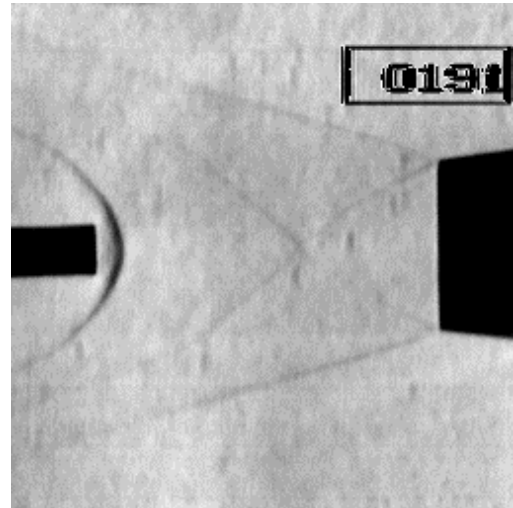
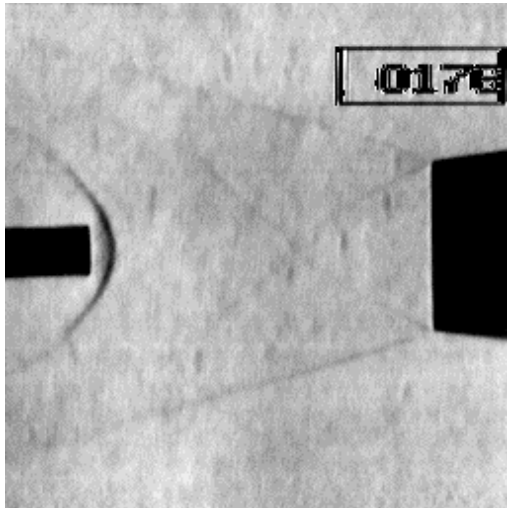


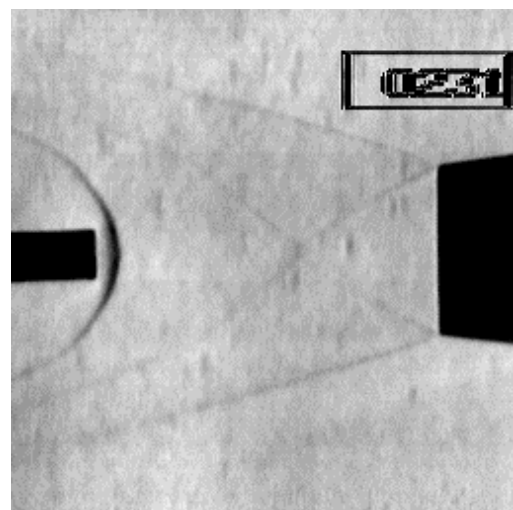
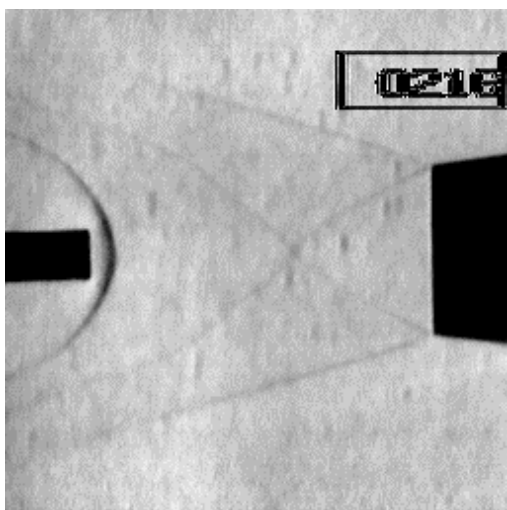
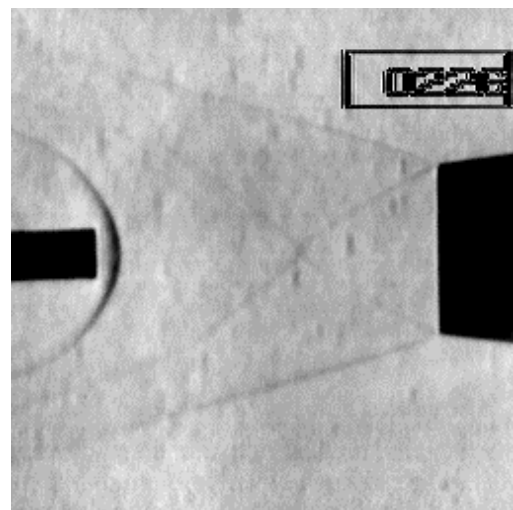
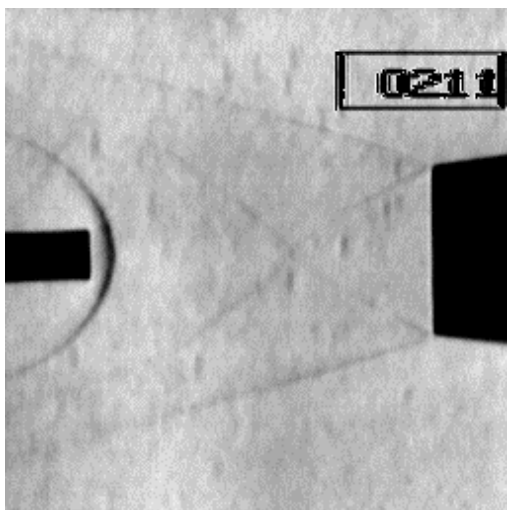
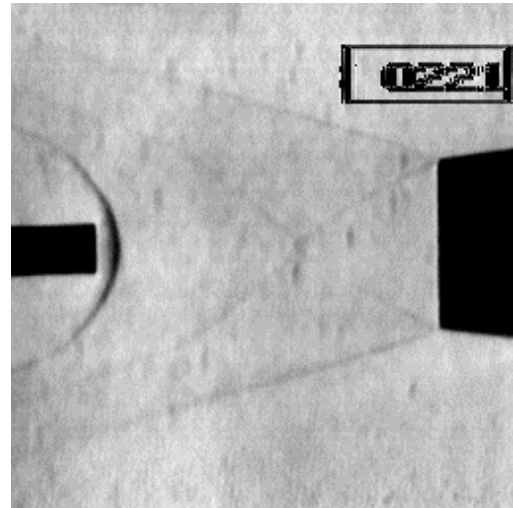
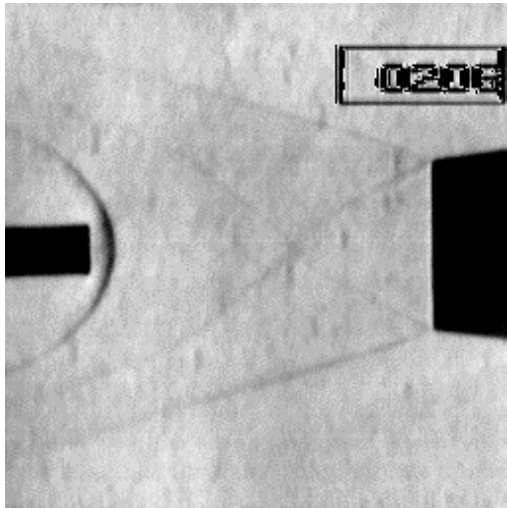




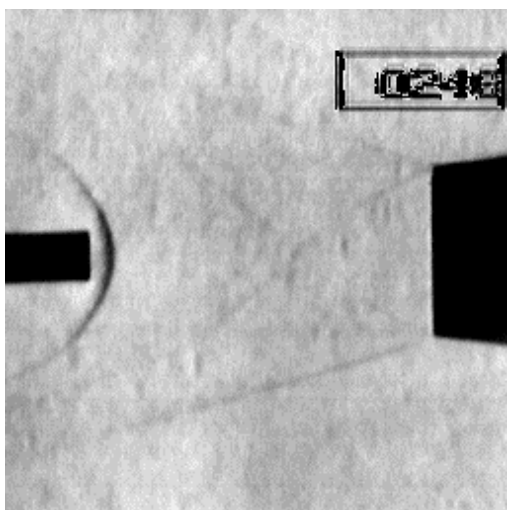
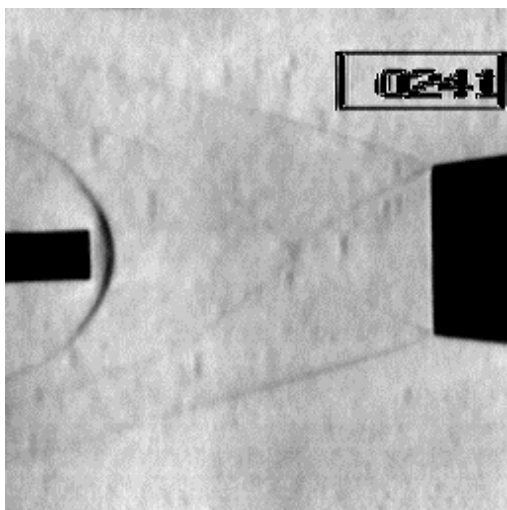
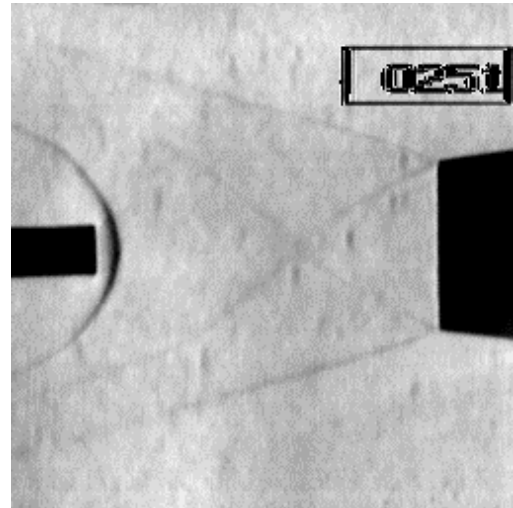
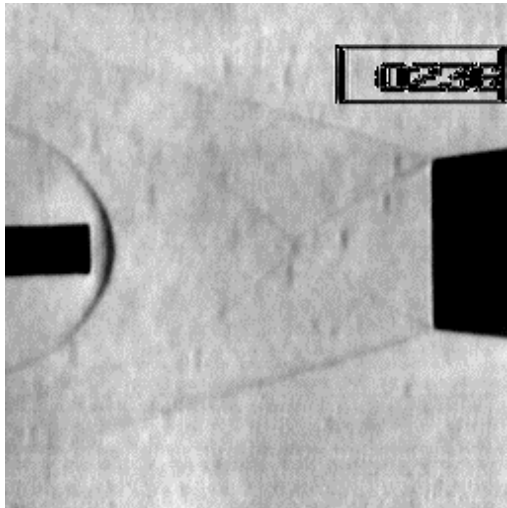












### **S3. Schlieren images of MW discharge regions interaction with the BSW**

**Gas: Carbon dioxide**

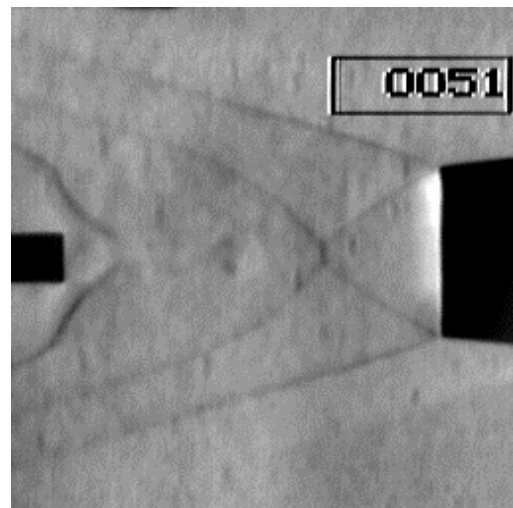
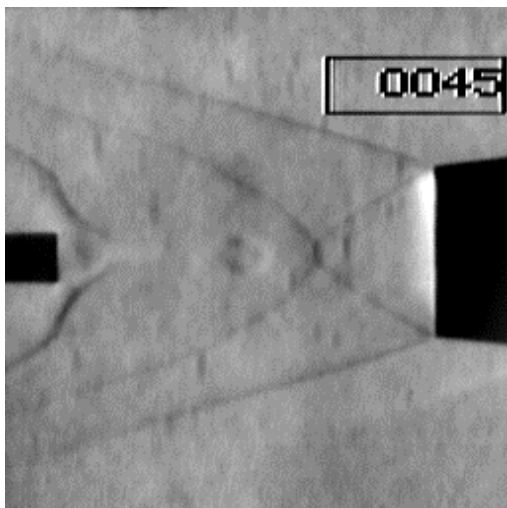
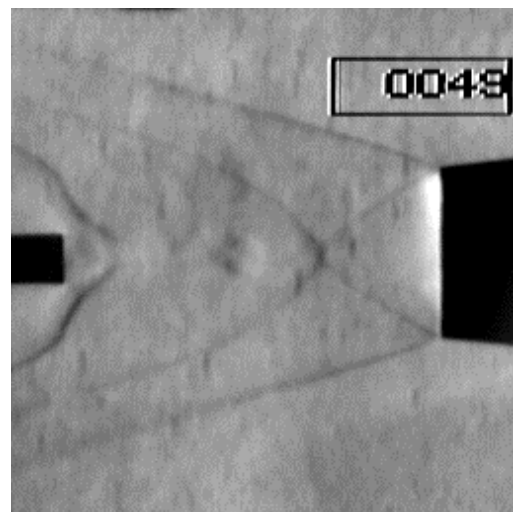
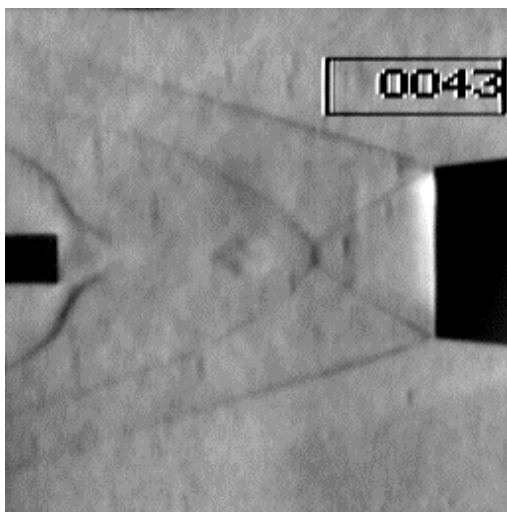
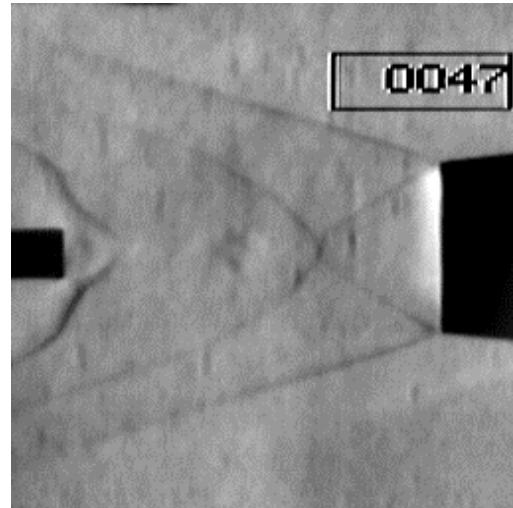
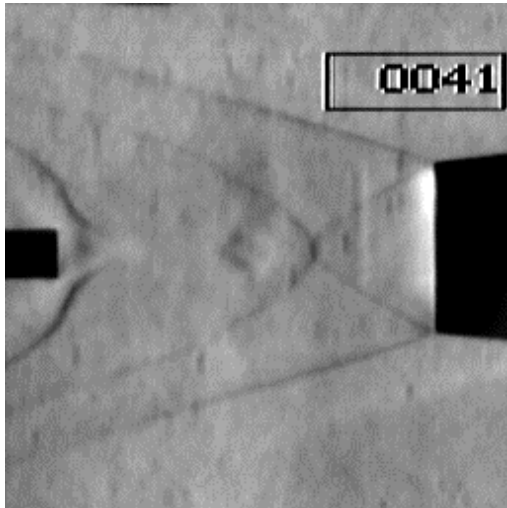
**Model: 8mm diameter**

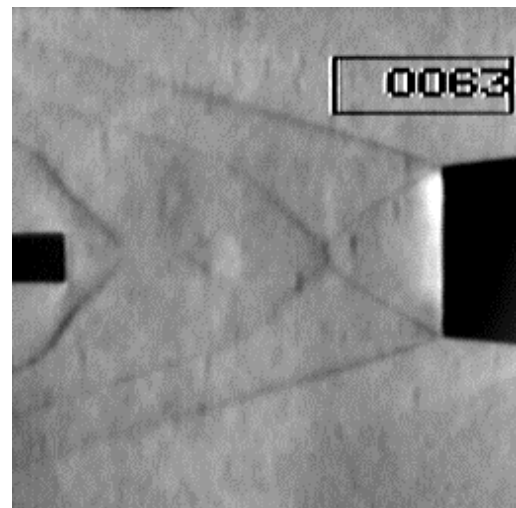
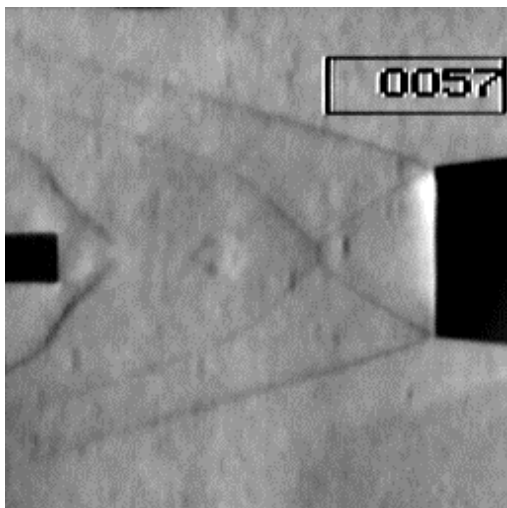
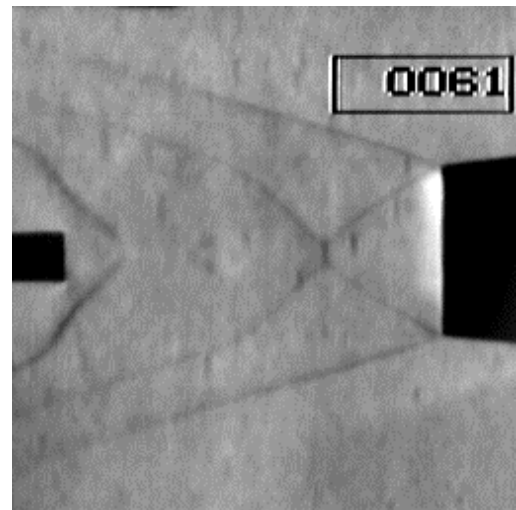
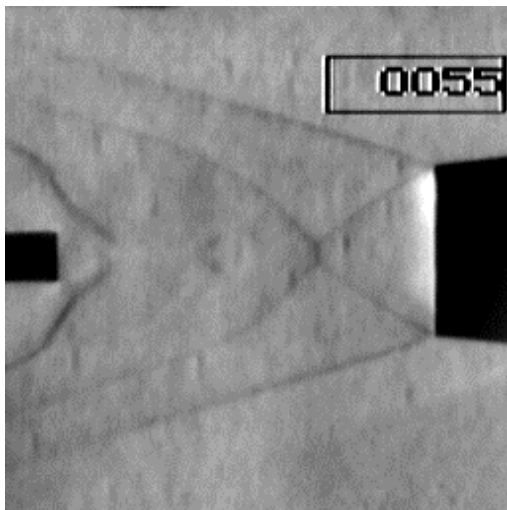
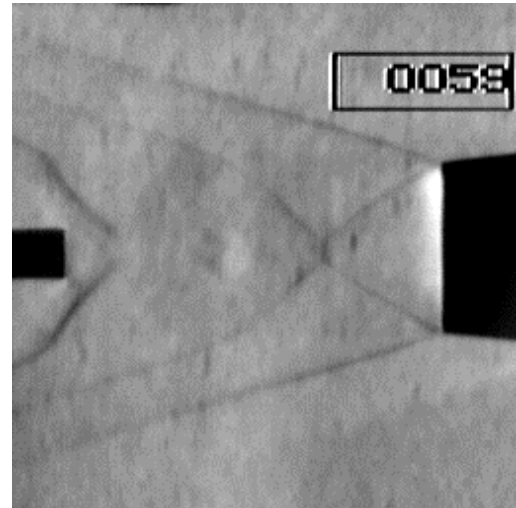
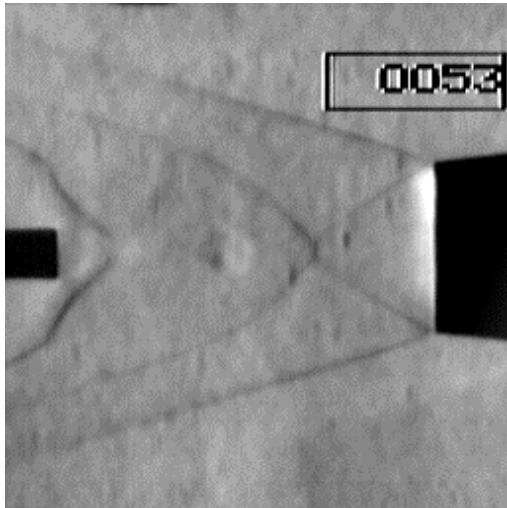
**Model position: 55mm from the central nozzle**

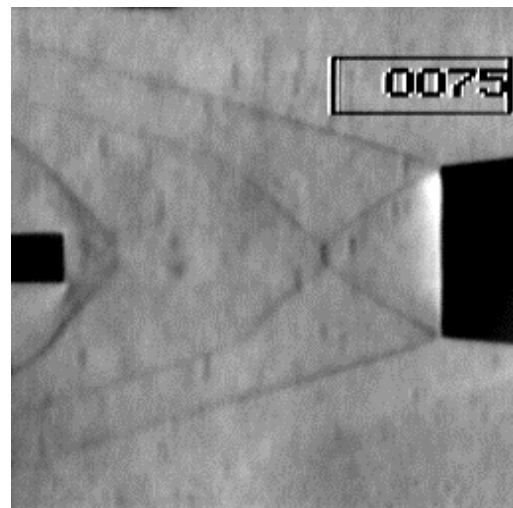
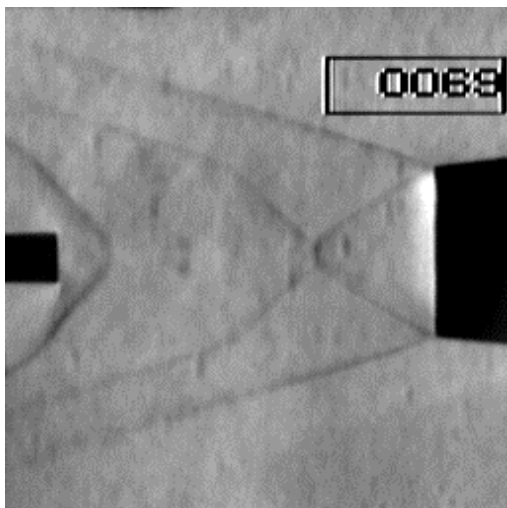
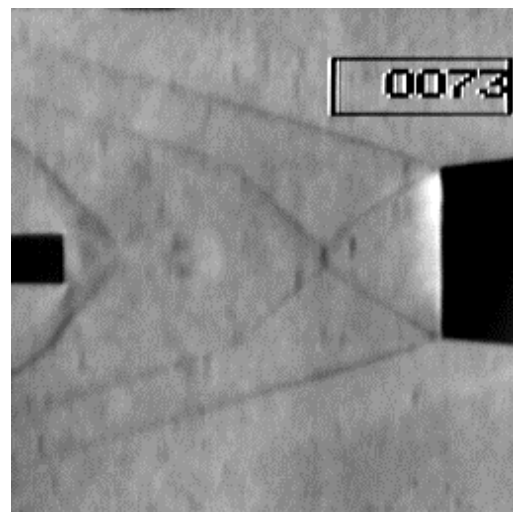
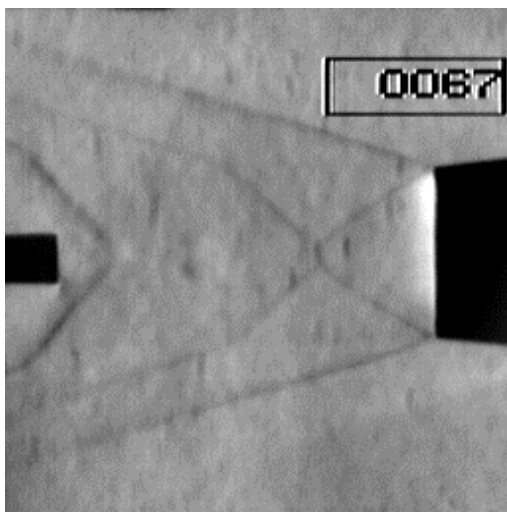
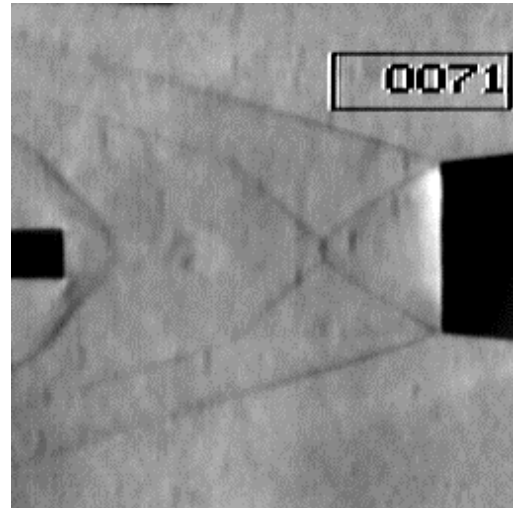
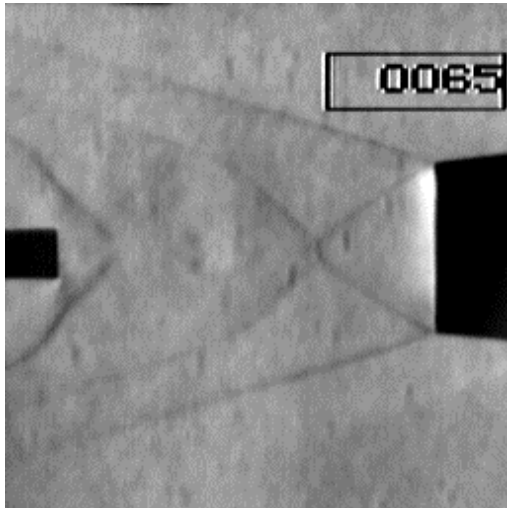
**Electric field: Z – directed**

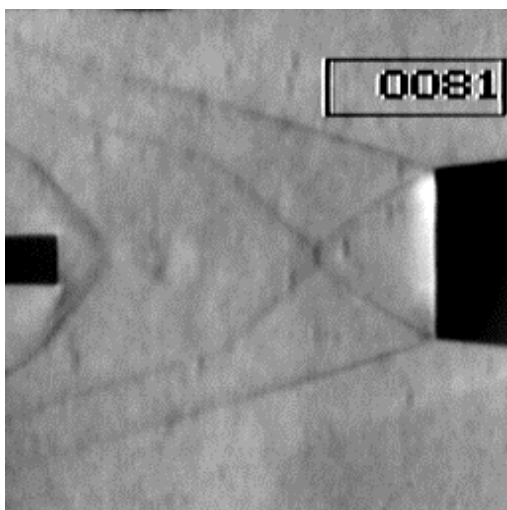
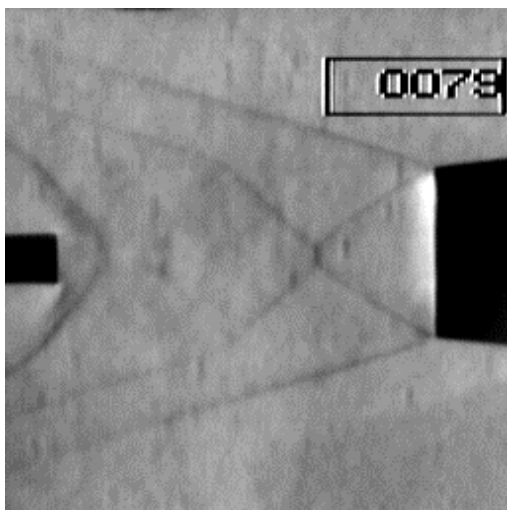
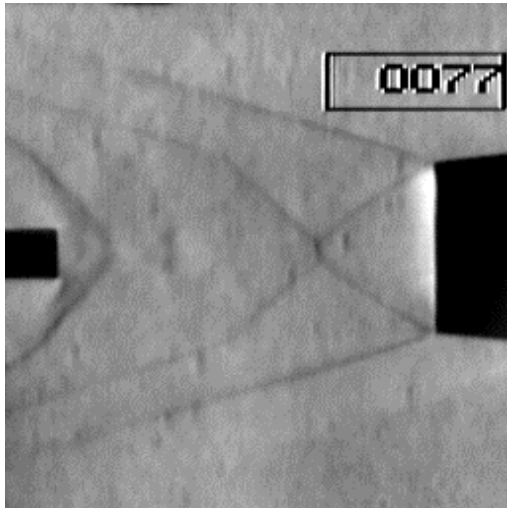
**The figure in the right upper corner of each frame is time interval  
(in microseconds) after MW pulse.**











## **S4. Schlieren images of shock wave evolution from the channel of MW discharge**

**Gas: Carbon dioxide**

**Model: 8mm diameter**

**Model position: 43mm from the central nozzle**

**Electric field: Z – directed**

**The figure in the right upper corner of each frame is time interval  
(in microseconds) after MW pulse.**

